Theoretical determination of electric field-magnetic field phase diagrams of the multiferroic bismuth ferrite

by

Marc Alexander Allen
B.Sc., University of British Columbia, 2009

A Thesis Submitted in Partial Fulfillment of the
Requirements for the Degree of

MASTER OF SCIENCE

in the Department of Physics and Astronomy

Theoretical determination of electric field-magnetic field phase diagrams of the multiferroic bismuth ferrite

by

Marc Alexander Allen
B.Sc., University of British Columbia, 2009

Supervisory Committee

Dr. Rogério de Sousa, Supervisor
(Department of Physics and Astronomy)

Dr. Byoung-Chul Choi, Departmental Member
(Department of Physics and Astronomy)

Supervisory Committee

Dr. Rogério de Sousa, Supervisor
(Department of Physics and Astronomy)

Dr. Byoung-Chul Choi, Departmental Member
(Department of Physics and Astronomy)

ABSTRACT

Bismuth ferrite (BFO) is a multiferroic material with cross-correlation between magnetic and electric orders. With no applied external fields the spin structure of BFO is anitferromagnetic and cycloidal. This ordering prevents the detection of the weak ferromagnetism known to exist in the material. The application of magnetic and electric fields of suitable strength and direction is capable of compelling the Fe^{3+} spins to align in a homogeneous, antiferromagnetic fashion. This report details how numerical methods were used to simulate the spin alignment of a BFO system under different fields. The results were compiled into electric field-magnetic field phase diagrams of BFO to show the divide between cycloidal and homogeneous systems.

Contents

Supervisory Committee ii

Abstract iii

Table of Contents iv

List of Tables vi

List of Figures vii

Acknowledgements x

1 Introduction 1

1.1 A Brief Introduction to Multiferroic Materials . . . 3

1.1.1 Ferroics . . . 3

1.1.2 More Than One at a Time . . . 5

1.2 Bismuth Ferrite . . . 6

1.2.1 Electrical Control of Magnetism . . . 7

1.2.2 Last Dance: Killing the Cycloid . . . 8

1.3 Magnetic Field . . . 8

1.4 Electric Field . . . 9

1.5 Claims . . . 10

1.6 Agenda . . . 10

2 Microscopic Model of BFO 11

2.1 Heisenberg Interaction . . . 12

2.2 Dzyaloshinskii-Moriya Interaction . . . 13

2.3 Single-Ion Anisotropy . . . 15

2.4 Analytical Energy Minimization: Cycloidal versus Homogeneous . . . 15

2.5 Zeeman Interaction . . . 18

2.6 Electric Field Coupled to Spins 18

3 Approach to Simulations **19**
3.1 Steepest Descent 19
3.1.1 Adaptive Step Size 21
3.1.2 Challenges of Steepest Descent 22
3.2 Monte Carlo Simulations 23
3.3 Algorithm for Finding Ground State of BFO 24
3.4 Analysis of Algorithm Results 27
3.4.1 Zero Padding 28
3.4.2 Windowing 28
3.4.3 Fast Fourier Transform 28

4 Results **34**
4.1 Initial Results 34
4.2 Competition Between Conical Cycloidal and Homogeneous Ordering . 39
4.3 Electric Field-Induced Anisotropy 43
4.4 Magnetic Field-Induced Homogeneity 48
4.5 Electric Field-Magnetic Field Phase Diagrams 51

5 Analysis and Conclusions **58**

Bibliography **63**

Appendix A Energy for Polarization along [111] **67**

Appendix B Additional Results **73**

List of Tables

Table 2.1 Common types of antiferromagnetism 13

List of Figures

Figure 1.1 Antiferromagnetic cycloid. The blue-green arrows represent the Néel vector **L** and the red arrows represent the local weak ferromagnetism. 2
Figure 1.2 Homogeneous, antiferromagnetic case. The blue-green arrows represent the Néel vector **L** and the red arrows represent the local weak ferromagnetism. 2
Figure 1.3 The order parameter is non-zero below its critical temperature. 4
Figure 1.4 Two unit cells of bismuth ferrite. The purple atoms are Bi^{3+}, red O^{2-} and gold Fe^{3+}. The left cell displays the cubic axes for BFO and the right cell shows the rhombohedral axes that it is convenient to use in describing BFO (see Chapter 2). Adapted from Reference [9]. 6

Figure 2.1 Spin ordering in the different types of antiferromagnetism. . . . 14

Figure 3.1 Diagram detailing steepest descent. All points on a line are of equal value for the function F. Steepest descent makes successive estimates of the value of $\mathbf{x}$ which minimizes F. 20
Figure 3.2 Coordinate system for spin used in simulations. The spin has unit length and is described solely by its azimuthal, ϕ, and polar, α, angles. 21
Figure 3.3 Energy per spin versus number of iterations. $\frac{D}{J} = 1.1$, $D' = A = 0$ and no applied fields. Comparison of speed of Monte Carlo methods versus steepest descent. Starting from a random spin configuration and the same Hamiltonian, a $20 \times 20 \times 20$ spin structure was minimized. It took over eight hours to produce the data from the Monte Carlo methods. The data from the steepest descent method were produced in four minutes. 24
Figure 3.4 FFT along $[01\bar{1}]$ direction. $\langle \|\mathbf{Q}\| \rangle$ is 1.35. 31

Figure 3.5 FFT along $[01\bar{1}]$ direction. $\langle\|\mathbf{Q}\|\rangle$ is 0.33. 32

Figure 4.1 Energy per spin versus $\frac{D}{J}$ with no applied fields or anisotropy. . 38

Figure 4.2 Simulation results of energy per spin versus magnetic field ($\mathbf{B} \parallel \hat{\mathbf{X}}$ and $\mathbf{B} \parallel \hat{\mathbf{Y}}$) compared with analytical conical cycloid and homogeneous cases for $\mathbf{P} \parallel [001]$. $\frac{D}{J} = \frac{2\pi}{5}$, $\frac{D'}{J} = 0.60$, $\frac{g\mu_B}{JS} = 0.317\ \mathrm{T}^{-1}$ and $A = E = 0$. 41

Figure 4.3 Simulation results of energy per spin versus magnetic field ($\mathbf{B} \parallel \hat{\mathbf{X}}$ and $\mathbf{B} \parallel \hat{\mathbf{Y}}$) compared with analytical conical cycloid and homogeneous cases for $\mathbf{P} \parallel [111]$. $\frac{D}{J} = \frac{2\pi}{5}$, $\frac{D'}{J} = 0.60$, $\frac{g\mu_B}{JS} = 0.317\ \mathrm{T}^{-1}$ and $A = E = 0$. 42

Figure 4.4 Electric field phase diagram. From Reference [9]. 45

Figure 4.5 $\langle\|\mathbf{Q}\|\rangle$ versus $\mathbf{E} \parallel -\hat{\mathbf{X}}$. $A = 0$, $\frac{D}{J} = \frac{2\pi}{5}$, $\frac{D'}{J} = 0.60$, $\frac{\xi}{J} = 5.77 \times 10^{-5}\ \mathrm{V\ cm}^{-1}$ and no magnetic field with $\mathbf{P} \parallel [001]$. . . . 48

Figure 4.6 $\langle\|\mathbf{Q}\|\rangle$ versus $\mathbf{E} \parallel -\hat{\mathbf{X}}$. $A = 0$, $\frac{D}{J} = \frac{2\pi}{5}$, $\frac{D'}{J} = 0.60$, $\frac{\xi}{J} = 5.77 \times 10^{-5}\ \mathrm{V\ cm}^{-1}$ and no magnetic field with $\mathbf{P} \parallel [111]$. . . . 49

Figure 4.7 $\langle\|\mathbf{Q}\|\rangle$ and magnetization modulus versus B^X. $A = 0$, $\frac{D}{J} = \frac{2\pi}{5}$, $\frac{D'}{J} = 0.60$, $\frac{g\mu_B}{JS} = 0.318\ \mathrm{T}^{-1}$ and no electric field ($\mathbf{P} \parallel [001]$). . 50

Figure 4.8 $\langle\|\mathbf{Q}\|\rangle$ and magnetization modulus versus B^X. $A = 0$, $\frac{D}{J} = \frac{2\pi}{5}$, $\frac{D'}{J} = 0.60$, $\frac{g\mu_B}{JS} = 0.318\ \mathrm{T}^{-1}$ and no electric field ($\mathbf{P} \parallel [111]$). . 51

Figure 4.9 $\langle\|\mathbf{Q}\|\rangle$ and magnetization modulus versus B^Y. $A = 0$, $\frac{D}{J} = \frac{2\pi}{5}$, $\frac{D'}{J} = 0.60$, $\frac{g\mu_B}{JS} = 0.318\ \mathrm{T}^{-1}$ and no electric field ($\mathbf{P} \parallel [001]$). . 52

Figure 4.10 $\langle\|\mathbf{Q}\|\rangle$ and magnetization modulus versus B^Y. $A = 0$, $\frac{D}{J} = \frac{2\pi}{5}$, $\frac{D'}{J} = 0.60$, $\frac{g\mu_B}{JS} = 0.318\ \mathrm{T}^{-1}$ and no electric field ($\mathbf{P} \parallel [111]$). . 53

Figure 4.11 $\langle\|\mathbf{Q}\|\rangle$ and magnetization modulus versus B^Z. $A = 0$, $\frac{D}{J} = \frac{2\pi}{5}$, $\frac{D'}{J} = 0.60$, $\frac{g\mu_B}{JS} = 0.318\ \mathrm{T}^{-1}$ and no electric field ($\mathbf{P} \parallel [001]$). . 54

Figure 4.12 $\langle\|\mathbf{Q}\|\rangle$ and magnetization modulus versus B^Z. $A = 0$, $\frac{D}{J} = \frac{2\pi}{5}$, $\frac{D'}{J} = 0.60$, $\frac{g\mu_B}{JS} = 0.318\ \mathrm{T}^{-1}$ and no electric field ($\mathbf{P} \parallel [111]$). . 54

Figure 4.13 $E^X - B^X$ phase diagram. $\mathbf{E} \parallel -\hat{\mathbf{X}}$ and $\mathbf{B} \parallel \hat{\mathbf{X}}$. ($\mathbf{P} \parallel [001]$). . . . 55

Figure 4.14 $E^X - B^X$ phase diagram. $\mathbf{E} \parallel -\hat{\mathbf{X}}$ and $\mathbf{B} \parallel \hat{\mathbf{X}}$ ($\mathbf{P} \parallel [111]$). . . . 55
Figure 4.15 $E^X - B^Y$ phase diagram. $\mathbf{E} \parallel -\hat{\mathbf{X}}$ and $\mathbf{B} \parallel \hat{\mathbf{Y}}$ ($\mathbf{P} \parallel [001]$). . . . 56
Figure 4.16 $E^X - B^Y$ phase diagram. $\mathbf{E} \parallel -\hat{\mathbf{X}}$ and $\mathbf{B} \parallel \hat{\mathbf{Y}}$ ($\mathbf{P} \parallel [111]$). . . . 56
Figure 4.17 $E^X - B^Z$ phase diagram. $\mathbf{E} \parallel -\hat{\mathbf{X}}$ and $\mathbf{B} \parallel \hat{\mathbf{Z}}$ ($\mathbf{P} \parallel [001]$). . . . 57
Figure 4.18 $E^X - B^Z$ phase diagram. $\mathbf{E} \parallel -\hat{\mathbf{X}}$ and $\mathbf{B} \parallel \hat{\mathbf{Z}}$ ($\mathbf{P} \parallel [111]$). . . . 57

Figure B.1 A comparison of spin projections with $B^Z = 10$ T and $B^Z = 20$ T. Projections are in the XY-, XZ- and YZ-planes. $A = B^X = B^Y = E = 0; \frac{D}{J} = \frac{2\pi}{5}; \frac{D'}{J} = 0.60$. 75
Figure B.2 FFT, $\left\|\tilde{\mathbf{M}}_{\mathbf{k}}\right\|$ and $\left\|\tilde{\mathbf{L}}_{\mathbf{k}}\right\|$ versus k^Y for $B^Z = 10$ T and $B^Z = 20$ T. $A = B^X = B^Y = E = 0; \frac{D}{J} = \frac{2\pi}{5}; \frac{D'}{J} = 0.60$. 76
Figure B.3 Spin projections with no applied fields. Projections are in the XY-, XZ- and YZ-planes. $A = 0; \frac{D}{J} = \frac{2\pi}{5}; \frac{D'}{J} = 0.60$. 77

ACKNOWLEDGEMENTS

I would like to thank my supervisor, Rogério de Sousa, for his assistance, energy and knowledge that greatly helped to form this project. I would also like to acknowledge all of the people with whom I have shared Elliott 112 over the years including Noah Stemeroff, Haitian Xu, Stphanie LaForest and Lei Zhang. The Condensed Matter group here at UVic is small in number, but not in impact.

Chapter 1

Introduction

As magnetic memory elements become increasingly small, there is the desire to limit the energy and increase the speed needed to switch them. The states of magnetic memory elements are conventionally switched via the local application of a magnetic field. If instead an electric field could be applied to switch the element, this would lower the energy required to write to the element. The memory itself should remain magnetic, to take advantage of the persistent nature of magnetic memory elements [1]. For a magnetic memory to be able to be controlled electrically, there needs to be interplay between magnetic and electric orders. The material bismuth ferrite ($BiFeO_3$ or BFO) displays such interplay at room temperature. As such, it is a material of great interest in the pursuit of creating an electrically-controlled magnetic memory device. This kind of capability could also be useful in the development of MRAM (magnetic random access memory), a technology that promises to integrate the computer hard drive into its processor [2].

While having many of the characteristics desirable for this new type of memory device, BFO has drawbacks that challenge the realization of a lower power magnetic memory. Firstly, it is antiferromagnetic, the spins in the material are antiparallel to each other. In a ferromagnetic system, the magnetization can be detected and states can be defined depending on which direction the magnetization is pointing. Whereas in an antiferromagnetic system, there is zero net magnetization and thus, nothing to read out. There are schemes where BFO is coupled to a ferromagnet and through exchange bias [3], the magnetization of the ferromagnet can be controlled [4, 5], but none where BFO can be used alone as a memory element. The second issue with BFO is the nature of the antiferromagentism.

Bulk BFO has its antiferromagnetism wrapped in a spiral shape known as a cycloid

(see Figure 1.1). Canted antiferromagnetic spin pairs produce local weak ferromagnetism. However, the cycloid structure means that the local weak ferromagnetism sinusoidally changes direction throughout the period of the cycloid and the weak ferromagnetism sums to zero over the crystal, meaning that it is macroscopically undetectable. If the cycloid could be unwound and the antiferromagnetism in BFO was merely of the homogeneous G-type kind, with canting still present, then the weak ferromagnetism would not sum to zero and could be detected. Figure 1.2 shows an illustration of the unwound cycloid with uniform weak ferromagnetism. From that, there is the potential to have a controllable, measurable property of BFO—a necessary component for memory read out. Several methods to unwind the cycloid were discovered in the past; these include the use of strain [6], chemical substitution [7], and the application of magnetic [8] or electric fields [9].

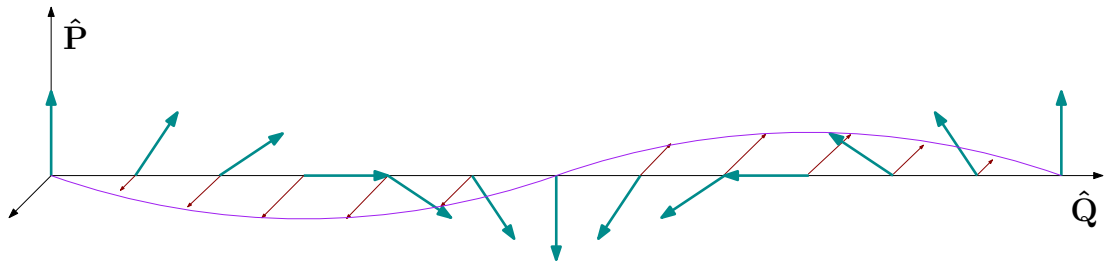

Figure 1.1: Antiferromagnetic cycloid. The blue-green arrows represent the Néel vector **L** and the red arrows represent the local weak ferromagnetism.

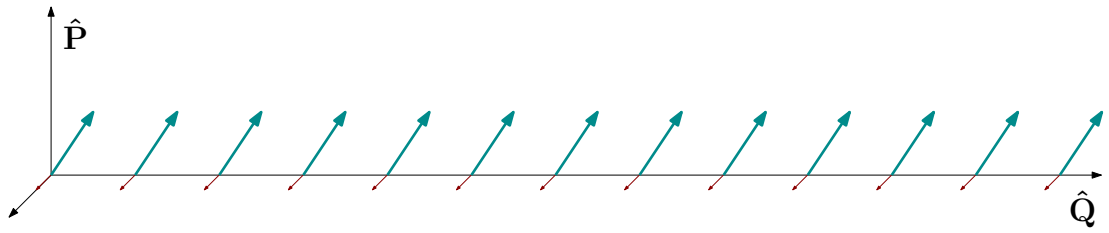

Figure 1.2: Homogeneous, antiferromagnetic case. The blue-green arrows represent the Néel vector **L** and the red arrows represent the local weak ferromagnetism.

While it is known that these methods will compel the system into homogeneous ordering, the threshold magnitudes for certain field directions are not well known. Nor has it been investigated, how combining multiple cycloid destroying effects at the same time affects the cycloid. This thesis details a theory of simultaneously applying magnetic and electric fields to a bulk BFO sample. The importance of understanding the electric field-magnetic field phase diagram of BFO has both practical

and fundamental aspects. The practical worth is in knowing the optimal way to remove the cycloid, returning to BFO's potential utility as a memory element. If a certain combination of field directions or strengths is favourable above others, that is, less energy expensive, then, if it is reasonable to apply fields in those directions to destroy the cycloid, that should be how the cycloid is destroyed. This thesis is of fundamental importance due to its investigation into an aspect of BFO that has not been probed. Are there new effects that happen when more than one field is applied at once? Is there a field combination where the effects oppose each other?

1.1 A Brief Introduction to Multiferroic Materials

1.1.1 Ferroics

A ferroic material has some inherent, reversible ordering of one of its properties, given certain environmental conditions are met, such as the material being at the proper temperature [10]. Types of ferroic orders include ferroelectricity, ferromagnetism and ferroelasticity. All ferroic materials are characterized by an order paramater. An order parameter is some property of the material which is non-zero when the material is in its ordered state and is zero when the material is not in its ordered state (see Figure 1.3).

Ferroelectricity

Ferroelectric materials have an electric polarization without the application of an electric field. The polarization vector **P** is the order parameter of ferroelectrics. BFO is a ferroelectric and has a very large polarization ($P \sim 100\ \mu C/cm^2$) that points along one of the cube diagonals of its perovskite unit cell [11]. The Curie temperature (T_c) is the temperature below which the material is ferroelectric. BFO has a Curie temperature of approximately 1140 K.

Ferromagnetism

In ferromagnetic materials, the spins of atoms parallel one another in the ordered phase. Materials have a non-zero magnetic moment under no applied magnetic field. Magnetization **M** is the order parameter here. Conventional magnetic memories are

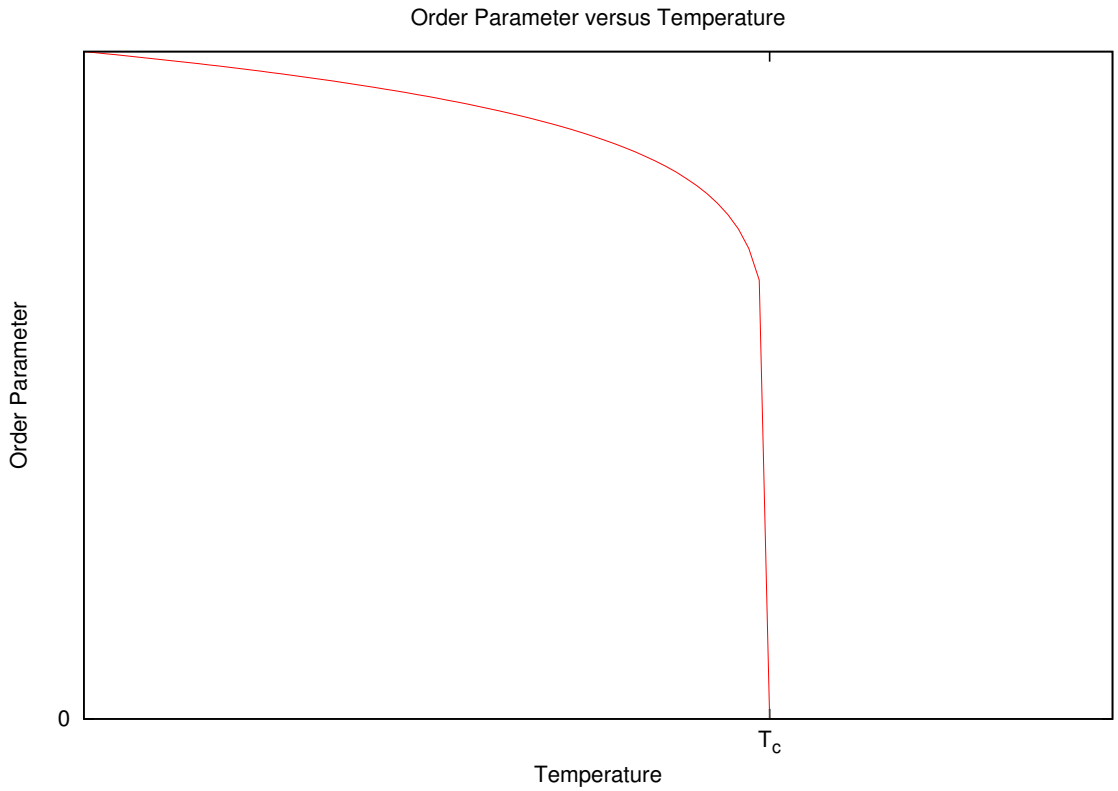

Figure 1.3: The order parameter is non-zero below its critical temperature.

made of ferromagnets. Were BFO ferromagnetic it would be almost the ideal material for use in electrically-written memories.

Antiferromagnetism

Unlike in ferromagnets, the spins of antiferromagnets are antiparallel: neighbouring spins point in opposite directions. The total magnetization for antiferromagnets is zero. This is why they cannot be used by themselves as memory elements. There is no detectable parameter to distinguish between states. The two sublattices of an antiferromagnet do have net magnetizations. The difference of the sublattice magnetizations is used to determine the order parameter, $\mathbf{L} = \mathbf{M_1} - \mathbf{M_2}$, which is known as the Néel vector. While $\mathbf{M}$ is easy to measure using inductance, the detection of $\mathbf{L}$ is much harder, usually requiring neutron or X-ray scattering experiments. Below the Néel temperature (T_N) a material is antiferromagnetic. The T_N of BFO is approximately 640 K.

Ferrimagnetism

Ferrimagnetism is a magnetic ordering intermediate between ferromagnetism and antiferromagnetism. Like in antiferromagets, neighbouring spins are antiparallel. However, the spins are of unequal magnitude, with the spins of one sublattice of greater magnitude than the other. This gives rise to net magnetization. Since $M_1 \neq M_2$, both $M = M_1 + M_2$ and $L = M_1 - M_2$ are non-zero.

Ferroelasticity

In ferroelastic materials, strain and symmetry reduction take place below a certain critical temperature which can be switched by applied stress.

1.1.2 More Than One at a Time

When multiple ferroic orders are present in the same phase in a material, the material is said to be multiferroic. Below 640 K, BFO is both ferroelectric and antiferromagnetic and thus multiferroic. BFO is one of the only room temperature multiferroics and, as a result, it has been the focus of much research over the past decade [12].

How to search for materials that are multiferroic is an issue of much discussion. If we leave other ferroic orders and just focus on ferroelectricity and (anti)ferromagnetism, the conventional pathway for one would seem to prevent the other from arising. This is due to ferroelectricity generally requiring an empty d-shell to allow for cations to be off-centre, which when replicated throughout the material leads to a net electric polarization. Magnetism generally requires partially filled d-shells [13, 14, 15].

BFO circumvents the issue by using its Fe^{3+} ion to give rise to its antiferromagnetism and its Bi^{3+} ion to give rise to its ferroelectricity (the mechanism of ferroelectricity in BFO is quite different from the usual d^0 mechanism: it involves instead the lowering of the energy of the $6s^2$ lone pair in Bi^{3+} when the ions goes off-centre [16]). Because the two ferroic orders are associated with different cations, it was assumed that the coupling between the two orders was relatively weak. However, recent research has challenged this notion. A recent experiment showed a magnon frequency shift that was linear with respect to an external applied electric field and 10^5 times larger than any other known electric field-induced magnon shift [17]. Further research into the theory behind this experimental result has shown how electric fields can be used to eliminate cycloidal ordering in BFO [9].

1.2 Bismuth Ferrite

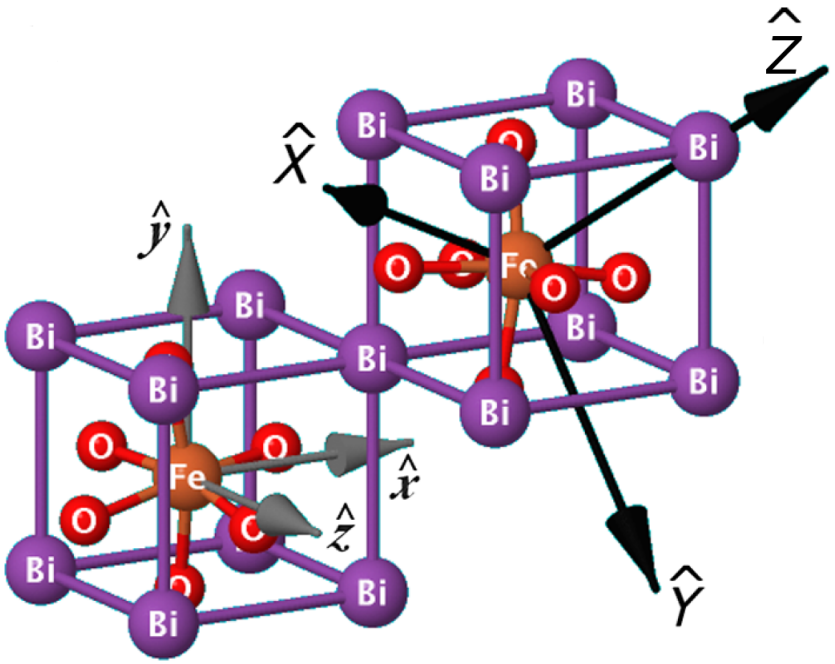

Figure 1.4: Two unit cells of bismuth ferrite. The purple atoms are Bi^{3+}, red O^{2-} and gold Fe^{3+}. The left cell displays the cubic axes for BFO and the right cell shows the rhombohedral axes that it is convenient to use in describing BFO (see Chapter 2). Adapted from Reference [9].

BFO (see Figure 1.4) has a distorted rhombohedral perovskite structure. It belongs to the R3c space group. A space group is the collection of operations (eg. rotations and translations) which when performed on a crystal leave it unaltered [18]. Its electric polarization is along one of its eight pseudocubic diagonal; [111] for example. The magnetic ground state of BFO is a spiral of the cycloid type, with period of 620 Å. The spins lie in the plane formed by the polarization **P** and the cycloid propagation vector **Q**, which points along one of three directions perpendicular to **P** (for instance, when **P** ∥ [111], **Q** can point along $[1\bar{1}0]$ and cyclic permutations). See Figure 1.1 for an example of this.

The cycloid in BFO is due to a spin-orbit effect [19]. The electric polarization in BFO compels the spins to arrange in a cycloid in order to interact with the polarization [20]. This is referred to as a spin-current effect.

Spin-orbit coupling also gives rise to the weak ferromagnetism due to spin canting in BFO [21, 22, 23]. It has been found that the average strength of the ferromag-

netism is 0.06 μ_B/Fe and is sinusoidal along the direction perpendicular to the cycloid plane [24]. This result gives hope of BFO having applications in magnetic memory technology. There is a detectable ferromagnetic moment. Of course, before BFO can be used in industry, its inherent cycloid must be destroyed so that the order parameter **M** becomes homogeneous.

1.2.1 Electrical Control of Magnetism

It was mentioned above that the cycloid plane is tied to the direction of the polarization. This fact has been the primary avenue through which researchers have attempted to gain electrical control of the magnetic ordering of BFO. The electric polarization of BFO can be switched to any of the eight body diagonals of the distorted rhombohedron with the application of an electric field, and this can force the spins into a different plane. Because the cycloid propagation direction is coupled to the polarization, switching the polarization can also change the propagation direction of the cycloid.

In 2008 Lebeugle *et al.* [25] were able to switch the polarization of bulk BFO and neutron diffraction determine that the spins indeed changed planes. Chu *et al.* [4] placed ferromagnetic CoFe on top of BFO and through poling BFO and the exchange bias between CoFe and BFO were able to switch the magnetization of CoFe domains. Lebeugle *et al.* were able to show that CoFeB deposited onto BFO gained a uniaxial magnetic anisotropy that could be matched with the cycloid of BFO. Electrical poling could switch the direction of the anisotropy [5].

All of these experiments relied upon the coupling of the cycloid propagation direction and the electric polarization. Rovillian *et al.* performed an experiment which demonstrated that poling the electric polarization was not the only way to get a substantial magnetoelectric response from BFO [17]. In the experiment, an electric field was applied to a sample of BFO. The field was varied and the frequencies of magnon modes was recorded. There was a significant shift in the frequencies of magnon modes with respect to applied electric field. To explain the shift, two electric field-dependent effects permitted by the R3c symmetry of BFO were added to the free energy theory of BFO. The theory also showed that an electric field beyond some threshold value would unwind the cycloid, forcing BFO into a homogeneous magnetic ground state.

1.2.2 Last Dance: Killing the Cycloid

If the weak ferromagnetism of BFO is to be utilised then destroying the cycloid is essential. There are many known methods to unwind the cycloid, e.g. strain [6], application of an external magnetic field [26, 8, 27], and chemical substitution [28]. Magnetic fields with a strength of $\sim$ 18 T are known to destroy the cycloid in BFO [26, 8, 27]. Recent theory work by Fishman [29] attempted to map the critical magnetic field for all orientations. Chemical substitution can also be used to destroy the cycloid. Yuan *et al.* found that substituting Nd^{3+} in place of Bi^{3+} in BFO reduced the electric polarization and changed the crystal structure [28]. With enough substitution, somewhere between x = 0.15 and x = 0.20 for $Bi_{1-x}Nd_xFeO_3$, the cycloid went away.

However, none of these methods is tunable. As well, the methods cannot be used for fast switching in a device. The goals of this thesis are to study the electric field method to unwind the cycloid and how the electric field competes with an applied magnetic field.

1.3 Magnetic Field

Strong magnetic fields, in the range of 18 T [26, 8, 27], are required to destroy the cycloid in bulk BFO.

Popov *et al.* showed that the application of a magnetic field elicited a change in the longitudinal electric polarization at a magnetic field strength of 20 T [8]. The change depended on the direction of the applied field. For a field in the [001] orthorhombic direction, below the critical field the longitudinal polarization increased with increasing field. Shortly before reaching the critical value, the polarization ceased increasing and very near the critical value began decreasing before having a substantial drop at the critical value. Fields were also applied along the hexagonal crystal structure directions of BFO and, in these instances, below the critical field the polarization increased quadratically with increasing applied field. The range of the critical field produced by the field theory model was B_c^z = (20–30) T.

Tokunaga *et al.* placed BFO crystals in magnetic fields of strengths up to and including 55 T [27]. At temperatures ranging from 4.2 K to 300 K, they saw a change in magnetization-magnetic field curves in the vicinity of 18 T. This led them to claim that this corresponded to a transition to a homogeneous, canted antiferromagnet

above 18 T. The group did not see any additional transitions as magnetic field strength was increased. Park *et al.* also saw a change in the magnetization-magnetic field curve. The transition at this work occured near 20 T [26]. The work was performed at 4.2 K.

There is substantial proof of the transition from cycloidal to homogeneous ordering in bulk BFO in the range of 18–20 T. Recently, Fishman computed the orientation dependence of the critical B field [29]. Fishman's theory was based on a particular family of variational magnetic states. In this thesis, we developed an unconstrained numerical method and we will question some of Fishman's results. A better model of the system would allow for more insight into when the transition is taking place.

1.4 Electric Field

Magnetoelectric coupling present in BFO allows for the interplay of electric and magnetic orders. A magnetic field can affect the polarization, as seen in Section 1.3. Conversely, an electric field can affect the spin ordering. This coupling occurs through spin-orbit interactions. Traditionally, the leading magnetoelectric effect in BFO has been expressed via the Dzyaloshinskii-Moriya interaction, where the large electric polarization of BFO induces the cycloidal ordering in absence of any applied fields. The Dzyaloshinskii-Moriya interaction is also responsible for the canting in BFO.

Recently, we discovered that there was another linear magnetoelectric effect in BFO which arises from the dependence of its single-ion anisotropy on the external electric field. Here we will show that this effect can compete with the Dzyaloshinskii-Moriya interaction and unwind the cycloid [9].

Since the conditions under which BFO becomes homogeneous under electric field only have been discovered recently, there has been no study of the corresponding electric field-magnetic field phase diagram detailing the applied fields where BFO is cycloidal and where it is homogeneous. Understanding the precise conditions under which BFO transforms from cycloidal ordering to homogeneous would allow the determination of the optimal way for transforming between the two phases. As we shall show, the interactions that arise from E and B lead to an interesting competition that sheds light on the physics of spiral magnetism. Our study will also provide insight as to how the spin structure would change under other conditions.

1.5 Claims

In this thesis parts of the electric field-magnetic field phase diagram of bulk BFO have been mapped via numerical minimization of the Hamiltonian for BFO. We will show that depending on the relative orientation of E and B fields, the cycloid phase may or may not persist at lower fields than anticipated. This occurs because the E and B interactions may either compete or cooperate with each other.

This work will allow for a better understanding of the requirements for destroying the cycloid of BFO and will help in the decision as to the best approach to take in switching the cycloid in devices.

1.6 Agenda

Below is a description of the layout of the thesis.

Chapter 1 provides an introduction to the work, its import, what has been achieved and details on how BFO is transformed. It also describes what will proceed in the following chapters.

Chapter 2 describes the microscopic model used to model BFO.

Chapter 3 details the computational methods used in our numerical energy minimization.

Chapter 4 examines our numerical results and compares them with our developed analytical theory.

Chapter 5 provides a discussion of our results and outlines our conclusions.

Chapter 2

Microscopic Model of BFO

The Hamiltonian used in the model is comprised of a standard Heisenberg Hamiltonian interaction with a positive exchange integral, which accounts for the G-type antiferromagnetism of BFO; two Dzyaloshinskii-Moriya interactions, one which is the basis for the formation of the cycloid in BFO and the other is responsible for the weak ferromagnetism; a single-ion anisotropy interaction, which arises from spin-orbit coupling; a Zeeman interaction; and interactions based on the response of BFO to an electric field.

$$\begin{aligned} H =& \sum_i \sum_{\boldsymbol{\delta}} \left(J \mathbf{S}_{1,i} \cdot \mathbf{S}_{2,i+\boldsymbol{\delta}} + \left[D \left\{ \hat{\mathbf{Z}} \times \frac{(\boldsymbol{\tau} + \boldsymbol{\delta})}{a_{Rh}} \right\} + D' \, \hat{\mathbf{Z}} \right] \cdot \left[\mathbf{S}_{1,i} \times \mathbf{S}_{2,i+\boldsymbol{\delta}} \right] \right) \\ & - \frac{A}{2} \sum_i \sum_{\eta=1,2} \left(\mathbf{S}_{\eta,i} \cdot \hat{\mathbf{Z}} \right)^2 - g\mu_B \sum_i \sum_{\eta=1,2} \left(\mathbf{S}_{\eta,i} \cdot \mathbf{B} \right) \\ & - \frac{\xi}{4} \sum_i \sum_{\eta=1,2} \left(\mathbf{E}_\perp \cdot \left[\left\{ \left(S^Y_{\eta,i} \right)^2 - \left(S^X_{\eta,i} \right)^2 \right\} \hat{\mathbf{X}} + 2 S^X_{\eta,i} S^Y_{\eta,i} \hat{\mathbf{Y}} \right] \right. \\ & \left. + 2\sqrt{2} \mathbf{E}_\perp \cdot \left[S^X_{\eta,i} \hat{\mathbf{X}} + S^Y_{\eta,i} \hat{\mathbf{Y}} \right] S^Z_{\eta,i} \right). \end{aligned} \tag{2.1}$$

Here, i represents the $N/2$ (where N is the total number of spins) sites of the first sublattice, $\boldsymbol{\tau}$ is the vector $a_{Rh}\,(1,1,1)$ which connects a Fe^{3+} ion from the first sublattice to its antiferromagnetic pair in the second, a_{Rh} is the rhombohedral lattice constant of BFO, $\boldsymbol{\delta}$ is the collection of vectors which when added with $\boldsymbol{\tau}$ link a first sublattice spin with its six nearest neighbours ($\boldsymbol{\delta} \in [a_{Rh}\,(0,-1,-1)$, $a_{Rh}\,(-2,-1,-1)$, $a_{Rh}\,(-1,0,-1)$, $a_{Rh}\,(-1,-2,-1)$, $a_{Rh}\,(-1,-1,0)$, $a_{Rh}\,(-1,-1,-2)]$). $\boldsymbol{\tau} + \boldsymbol{\delta} = \pm a_{Rh}\,(1,0,0)$ and cyclic permutations.

$\mathbf{S}_{\eta,i}$ represents the (classical) spin vector, with $|\mathbf{S}_{\eta,i}| = S = \frac{5}{2}$ for BFO. The

first index, η, designates to which sublattice the spin belongs and the second, i, describes its position in the material. D and D' are Dzyaloshinskii-Moriya interaction coefficients. A is the single-ion anisotropy coefficient. g is the Landé g-factor and μ_B is the Bohr magneton. ξ is the coefficient for the coupling of an external electric field to the spins. $\mathbf{B}$ and $\mathbf{E}_\perp$ are the applied magnetic and electric fields respectively. The perpendicular notation of the electric field is indicative that only components of the applied electric field which are perpendicular to the electric polarization are taken under consideration in the model. A rhombohedral coordinate system that differs from the cubic one was used: $\hat{\mathbf{X}} = \frac{(-2,1,1)}{\sqrt{6}}$, $\hat{\mathbf{Y}} = \frac{(0,-1,1)}{\sqrt{2}}$, $\hat{\mathbf{Z}} = \frac{(1,1,1)}{\sqrt{3}}$ (see Figure 1.4).

2.1 Heisenberg Interaction

The Heisenberg interaction, represented by the first term in Equation (2.1), is responsible for the fundamental magnetic nature of the material,

$$H_{Ex} = J \sum_i \sum_{\boldsymbol{\delta}} \mathbf{S}_{1,i} \cdot \mathbf{S}_{2,i+\boldsymbol{\delta}}. \tag{2.2}$$

The sign of J, the exchange integral, determines whether the material is ferromagnetic or antiferromagnetic. If $J < 0$, then it is advantageous for spins to be parallel and the material is ferromagnetic. If $J > 0$, then the system has its lowest energy configuration if spins are antiparallel and the material is antiferromagnetic.

In some systems J takes on different values depending on the direction of coupling of the spins. For instance there are situations where if $\mathbf{S}_{1,i}$ and $\mathbf{S}_{2,i+\boldsymbol{\delta}}$ are in the same xy-plane then J is negative, resulting in ferromagnetism in the plane. But if the spins are not of the same xy-plane then J is positive. The resulting spin structure is still antiferromagnetic like BFO, but it is of a different type. Wollan and Koehler classified these different types of antiferromagnetism [30]. A material exhibiting the type of arrangement described above is classified as an A-type antiferromagnet, whereas BFO with all nearest neighbours being antiparallel with respect to one another is a G-type antiferromagnet. See Table 2.1 and Figure 2.1 for more details on the different types of antiferromagnetism.

Superexchange is the mechanism behind the antiferromagneitc coupling of BFO. Via oxygen, it couples Fe^{3+} cations. The O^{2-} ion has a filled 3p orbital which overlaps

Type	Spin Arrangement
A	Adjacent layers are antiparallel
C	Adjacent columns are antiparallel
G	Adjacent spins are antiparallel

Table 2.1: Common types of antiferromagnetism

with 3d orbitals from neighbouring Fe^{3+} ions. The spin quantum number for Fe^{3+} is $S = \frac{5}{2}$. By Hund's rules, each of the five valence electrons of the Fe^{3+} ions occupy a different 3d orbital, with all spins parallel to each other. The overlapping filled 3p orbital of the O^{2-} ion necessarily has antiparallel spins. The bonding between the O^{2-} and Fe^{3+} ions is mainly ionic, but can be thought as having some covalent character. An electron from the 3p O^{2-} orbital can then hop to one of the 3d Fe^{3+} orbitals to form the covalent bond. Since each 3d Fe^{3+} orbital is occupied with a parallel spin, the electron donated from O^{2-} must be of opposite spin to those in the 5 3d Fe^{3+} orbitals. Spin is preserved during the hopping process. On the other side of the 3p O^{2-} orbital, the same type of covalent bond can be formed with the next Fe^{3+} ion. However, the spin that the now O^{-} ion can donate to Fe^{3+} is antiparallel to the one given to the neighbouring Fe^{3+} ion since they come from the same 3p orbital and are required to be antiparallel. This means that the five 3d orbitals of Fe^{3+} to now receive an electron must contain electron spins which are antiparallel to the neighbouring Fe^{3+} ion for covalent bonding to occur. Through this mechanism neighbouring Fe^{3+} ions lower their energy by being antiparallel [31].

2.2 Dzyaloshinskii-Moriya Interaction

Adding spin-orbit coupling to the superexchange mechanism gives rise to a term that is linear in spin-orbit coupling and linear in the superexchange interaction. This is the so called Dzyaloshinskii-Moriya coupling that favors non-collinear ordering of the spins. The Dzyaloshinskii-Moriya interaction is what leads to the cycloidal ordering in BFO, and is also behind its weak ferromagnetism.

In 1958, Dzyaloshinskii argued that the weak ferromagnetism exhibited by some antiferromagnets was due to their symmetry [32]. Two years later, Moriya extended the theory of superexchange to include spin-orbit coupling and claimed that this was the theoretical basis for the weak ferromagnetism in the antiferromagnets [33, 34].

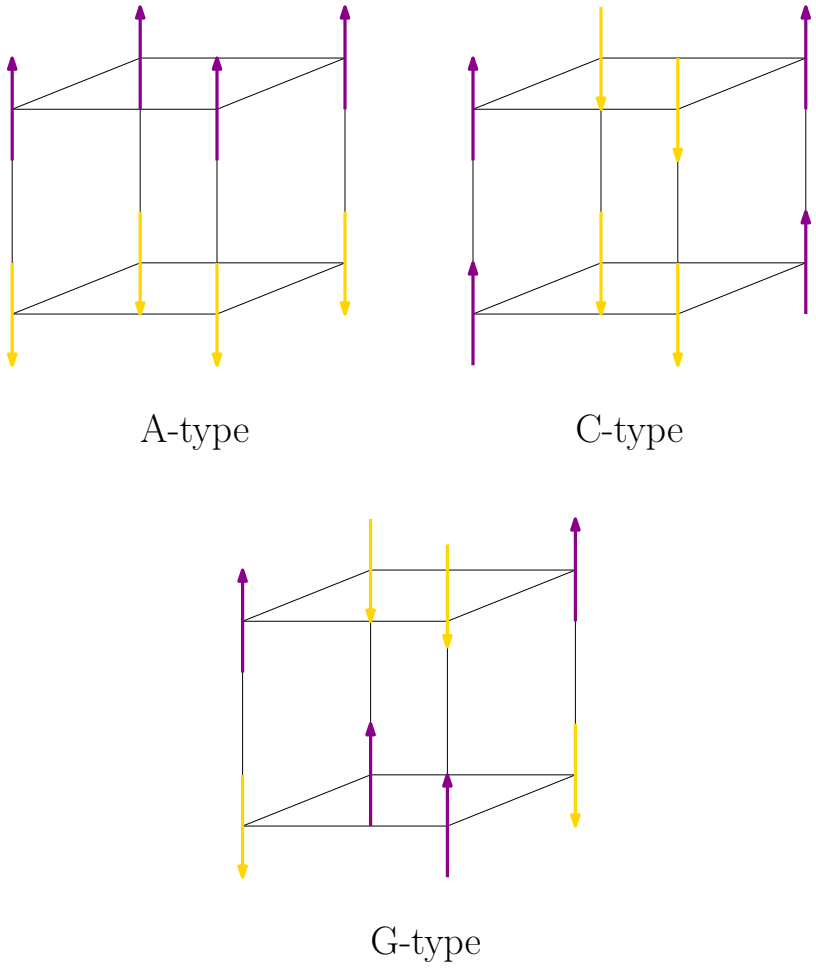

Figure 2.1: Spin ordering in the different types of antiferromagnetism.

Two different Dzyaloshinskii-Moryia interactions are shown in the first line of Equation (2.1):

$$H_{DM} = \sum_i \sum_{\boldsymbol{\delta}} \left(D \left[\hat{\mathbf{Z}} \times \frac{\{\boldsymbol{\tau} + \boldsymbol{\delta}\}}{a_{Rh}} \right] + D' \, \hat{\mathbf{Z}} \right) \cdot (\mathbf{S}_{1,i} \times \mathbf{S}_{2,i+\boldsymbol{\delta}}) \,. \tag{2.3}$$

The first, a spin-current interaction [19], leads to the generation of the cycloid in BFO. The second is responsible for the weak ferromagnetism present in BFO.

The Dzyaloshinskii-Moriya interaction may also be expressed as

$$H_{DM} = D \, (\mathbf{R}_O \times \mathbf{R}_{ij}) \cdot (\mathbf{S}_i \times \mathbf{S}_j) \,. \tag{2.4}$$

$\mathbf{R}_O$ is the vector from the iron spin i to the oxygen. $\mathbf{R}_{ij}$ is the vector connector iron

spin i to iron spin j. If the oxygen positions are substituted into Equation (2.4) then the interaction can be written as

$$H_{DM} = \sum_{\langle i,j \rangle} \left(\mathbf{P} \times \mathbf{R}_{ij} + \alpha \hat{\mathbf{Z}} \right) \cdot \left(\mathbf{S}_i \times \mathbf{S}_j \right). \tag{2.5}$$

$\langle i, j \rangle$ indicates that spins i and j are nearest neighbours. In Equation (2.5), the electric polarization in the energy indicates that the oxygen ions contribute to the ferroelectric moment and α is related to the counter rotation of oxygen tetrahedra adjacent along the polarization direction.

2.3 Single-Ion Anisotropy

Single-ion anisotropy is a correction to the spin energy that is quadratic in spin-orbit coupling [9].

$$H_{SIA} = -\frac{A}{2} \sum_i \sum_{\eta=1,2} \left(\mathbf{S}_{\eta,i} \cdot \hat{\mathbf{Z}} \right)^2. \tag{2.6}$$

2.4 Analytical Energy Minimization: Cycloidal versus Homogeneous

The anisotropy is present even without the application of an electric field and, if A is large enough, will change the spin structure of BFO from cycloidal to homogeneous. To see this consider the energy of the system for a homeogeneous antiferromagnet (with no applied fields):

$$\mathbf{S}_{1,i} = S\,\hat{\mathbf{Z}}, \tag{2.7a}$$

$$\mathbf{S}_{2,i} = -S\,\hat{\mathbf{Z}}. \tag{2.7b}$$

$$\begin{aligned} H_{homogeneous} &= \sum_i \sum_{\boldsymbol{\delta}} \left(J \mathbf{S}_{1,i} \cdot \mathbf{S}_{2,i+\boldsymbol{\delta}} + \left[D \left\{ \hat{\mathbf{Z}} \times \frac{(\boldsymbol{\tau} + \boldsymbol{\delta})}{a_{Rh}} \right\} + D'\,\hat{\mathbf{Z}} \right] \cdot \left[\mathbf{S}_{1,i} \times \mathbf{S}_{2,i+\boldsymbol{\delta}} \right] \right) \\ &\quad - \frac{A}{2} \sum_i \sum_{\eta=1,2} \left(\mathbf{S}_{\eta,i} \cdot \hat{\mathbf{Z}} \right)^2 \\ &= -\frac{6JNS^2}{2} - \frac{NAS^2}{2} \end{aligned}$$

$$= -NS^2\left(3J + \frac{A}{2}\right). \tag{2.8}$$

Compare the homogeneous energy to the case of a harmonic cycloid:

$$\mathbf{S}_{1,i} = S\left(\cos\left[\mathbf{Q}\cdot\mathbf{R}_{1,i}\right]\hat{\mathbf{Z}} + \sin\left[\mathbf{Q}\cdot\mathbf{R}_{1,i}\right]\hat{\mathbf{Q}}\right), \tag{2.9a}$$

$$\mathbf{S}_{2,i} = -S\left(\cos\left[\mathbf{Q}\cdot\mathbf{R}_{2,i}\right]\hat{\mathbf{Z}} + \sin\left[\mathbf{Q}\cdot\mathbf{R}_{2,i}\right]\hat{\mathbf{Q}}\right). \tag{2.9b}$$

$$\begin{aligned}
H_{cycloid} &= \sum_i\sum_{\boldsymbol{\delta}}\left(J\mathbf{S}_{1,i}\cdot\mathbf{S}_{2,i+\boldsymbol{\delta}} + \left[D\left\{\hat{\mathbf{Z}}\times\frac{(\boldsymbol{\tau}+\boldsymbol{\delta})}{a_{Rh}}\right\} + D'\,\hat{\mathbf{Z}}\right]\cdot\left[\mathbf{S}_{1,i}\times\mathbf{S}_{2,i+\boldsymbol{\delta}}\right]\right) \\
&\quad - \frac{A}{2}\sum_i\sum_{\eta=1,2}\left(\mathbf{S}_{\eta,i}\cdot\hat{\mathbf{Z}}\right)^2 \\
&= S^2\sum_i\sum_{\boldsymbol{\delta}}\left(-J\left[\cos\left\{\mathbf{Q}\cdot\mathbf{R}_{1,i}\right\}\cos\left\{\mathbf{Q}\cdot\mathbf{R}_{2,i+\boldsymbol{\delta}}\right\}\right.\right. \\
&\quad \left.\left. + \sin\left\{\mathbf{Q}\cdot\mathbf{R}_{1,i}\right\}\sin\left\{\mathbf{Q}\cdot\mathbf{R}_{2,i+\boldsymbol{\delta}}\right\}\right] \right. \\
&\quad \left. + \left[\cos\left\{\mathbf{Q}\cdot\mathbf{R}_{2,i+\boldsymbol{\delta}}\right\}\sin\left\{\mathbf{Q}\cdot\mathbf{R}_{1,i}\right\} - \cos\left\{\mathbf{Q}\cdot\mathbf{R}_{1,i}\right\}\sin\left\{\mathbf{Q}\cdot\mathbf{R}_{2,i+\boldsymbol{\delta}}\right\}\right]\right. \\
&\quad \left.\times\left[D\left\{\hat{\mathbf{Z}}\times\frac{(\boldsymbol{\tau}+\boldsymbol{\delta})}{a_{Rh}}\right\} + D'\,\hat{\mathbf{Z}}\right]\cdot\left[\hat{\mathbf{Z}}\times\hat{\mathbf{Q}}\right]\right) \\
&\quad - \frac{AS^2}{2}\sum_i\sum_{\eta=1,2}\cos^2\left(\mathbf{Q}\cdot\mathbf{R}_{\eta,i}\right) \\
&= -S^2\sum_i\sum_{\boldsymbol{\delta}}\left(J\cos\left[\mathbf{Q}\cdot\left\{\boldsymbol{\tau}+\boldsymbol{\delta}\right\}\right]\right. \\
&\quad \left. + D\sin\left[\mathbf{Q}\cdot\left\{\boldsymbol{\tau}+\boldsymbol{\delta}\right\}\right]\left[\hat{\mathbf{Z}}\times\frac{(\boldsymbol{\tau}+\boldsymbol{\delta})}{a_{Rh}}\right]\cdot\left[\hat{\mathbf{Z}}\times\hat{\mathbf{Q}}\right]\right) - \frac{NAS^2}{4} \\
&= -\frac{NS^2}{2}\sum_{\boldsymbol{\delta}}\left(J\cos\left[\mathbf{Q}\cdot\left\{\boldsymbol{\tau}+\boldsymbol{\delta}\right\}\right]\right. \\
&\quad \left. + D\sin\left[\mathbf{Q}\cdot\left\{\boldsymbol{\tau}+\boldsymbol{\delta}\right\}\right]\left[\hat{\mathbf{Z}}\times\frac{(\boldsymbol{\tau}+\boldsymbol{\delta})}{a_{Rh}}\right]\cdot\left[\hat{\mathbf{Z}}\times\hat{\mathbf{Q}}\right]\right) - \frac{NAS^2}{4} \\
&= -\frac{NS^2}{2}\left(J\sum_{\boldsymbol{\delta}}\cos\left[\mathbf{Q}\cdot\left\{\boldsymbol{\tau}+\boldsymbol{\delta}\right\}\right]\right. \\
&\quad \left. + D\left[\hat{\mathbf{Z}}\times\left\{\sum_{\boldsymbol{\delta}}\sin\left(\mathbf{Q}\cdot\left[\boldsymbol{\tau}+\boldsymbol{\delta}\right]\right)\frac{\boldsymbol{\tau}+\boldsymbol{\delta}}{a_{Rh}}\right\}\right]\cdot\left[\hat{\mathbf{Z}}\times\hat{\mathbf{Q}}\right] + \frac{A}{2}\right).
\end{aligned} \tag{2.10}$$

$\hat{\mathbf{Z}} \times \hat{\mathbf{Q}} \perp \hat{\mathbf{Z}}$, therefore the weak ferromagnetism (D') term vanishes. If $Qa_{Rh} \ll 1$ then,

$$\begin{aligned} H_{cycloid} &\approx -NS^2 \left(J \left[3 - \frac{\{Qa_{Rh}\}^2}{2} \right] \right. \\ &\quad \left. + \frac{D}{2} \left[\hat{\mathbf{Z}} \times \left\{ \sum_{\boldsymbol{\delta}} \mathbf{Q} \cdot (\boldsymbol{\tau} + \boldsymbol{\delta}) \frac{\boldsymbol{\tau} + \boldsymbol{\delta}}{a_{Rh}} \right\} \right] \cdot \left[\hat{\mathbf{Z}} \times \hat{\mathbf{Q}} \right] + \frac{A}{4} \right) \\ &= -NS^2 \left(J \left[3 - \frac{\{Qa_{Rh}\}^2}{2} \right] + DQa_{Rh} \left[\hat{\mathbf{Z}} \times \hat{\mathbf{Q}} \right] \cdot \left[\hat{\mathbf{Z}} \times \hat{\mathbf{Q}} \right] + \frac{A}{4} \right) \\ &= -NS^2 \left(J \left[3 - \frac{\{Qa_{Rh}\}^2}{2} \right] + DQa_{Rh} + \frac{A}{4} \right). \end{aligned} \tag{2.11}$$

Taking the partial derivative of the energy with respect to Q will then give the value of Q which minimizes the energy:

$$\frac{\partial H_{cycloid}}{\partial Q} = NS^2 \left(JQa_{Rh}^2 - Da_{Rh} \right) = 0 \implies Qa_{Rh} = \frac{D}{J}. \tag{2.12}$$

Taking $Qa_{Rh} = \dfrac{D}{J}$,

$$\begin{aligned} H_{cycloid} &= -NS^2 \left(3J - \frac{D^2}{2J} + \frac{D^2}{J} + \frac{A}{4} \right) \\ &= -NS^2 \left(3J + \frac{D^2}{2J} + \frac{A}{4} \right). \end{aligned} \tag{2.13}$$

If we compare the energies of the homogeneous and cycloidal arrangements then we can see under what conditions homogeneous ordering is favoured:

$$\begin{gathered} H_{homogeneous} < H_{cycloid} \\ -NS^2 \left(3J + \frac{A}{2} \right) < -NS^2 \left(3J + \frac{D^2}{2J} + \frac{A}{4} \right) \\ \frac{A}{2} > \frac{D^2}{2J} + \frac{A}{4} \\ \frac{A}{4} > \frac{D^2}{2J} \\ A > \frac{2D^2}{J}. \end{gathered}$$

When $A > \frac{2D^2}{J}$, homogeneous spin ordering is energetically preferable to cycloidal.

2.5 Zeeman Interaction

The magnetic moment of an electron will interact with an external magnetic field. The Zeeman interaction describes this. g here is the Landé g-factor. $\mu_B = \frac{e\hbar}{2m_e}$ is the Bohr magneton. e is the elementary charge, $\hbar$ is the reduced Planck constant and m_e is the electron mass. At high enough fields, the interaction will cause the destruction of the cycloid in BFO. At high enough magnetic field values, the Zeeman interaction,

$$H_Z = -g\mu_B \sum_i \sum_{\eta=1,2} \mathbf{S}_{\eta,i} \cdot \mathbf{B}, \tag{2.14}$$

will dominate and the spins will all align.

2.6 Electric Field Coupled to Spins

From the microscopic theory related to single-ion anisotropy, it was found that there was coupling between an external electric field perpendicular to the electric polarization and the spins of the system [9]. The energy,

$$\begin{aligned} H_E = -\frac{\xi}{4} \sum_i \sum_{\eta=1,2} \Big(\mathbf{E}_\perp \cdot \left[\left\{ \left(S^Y_{\eta,i}\right)^2 - \left(S^X_{\eta,i}\right)^2 \right\} \hat{\mathbf{X}} + 2S^X_{\eta,i} S^Y_{\eta,i} \hat{\mathbf{Y}} \right] \\ + 2\sqrt{2}\mathbf{E}_\perp \cdot \left[S^X_{\eta,i} \hat{\mathbf{X}} + S^Y_{\eta,i} \hat{\mathbf{Y}} \right] S^Z_{\eta,i} \Big), \end{aligned} \tag{2.15}$$

is related to spin-orbit coupling. BFO, due to the presence of bismuth, has very strong spin-orbit coupling (spin-orbit coupling strength is proportional to Z^4 and Z = 83 for bismuth [35]). This strong spin-orbit coupling was seen in the experiment where magnon modes were significantly shifted with applied electric fields [17].

H_E was originally devolped to explain the shift of magnon modes as an electric field was applied. The response was 10^5 times [9] larger than any other ever seen in magnon spectra in response to the application of an electric field. The terms in Equation (2.15) are the ones allowed by the R3c symmetry of BFO. That is, allowed R3c space group operations performed on a BFO crystal will leave Equation (2.15) unchanged.

Chapter 3

Approach to Simulations

We developed a computer algorithm that used steepest descent methods to determine the spin structure of BFO when magnetic and electric fields were applied. The results of the simulations were then used to construct electric field-magnetic field phase diagrams of BFO. The simulations used the Hamiltonian described in Chapter 2. Below is an overview of the methods used in the algorithm and in the analysis of the resultant data.

3.1 Steepest Descent

To minimize a function $F(\mathbf{x})$ with respect to $\mathbf{x}$, a fraction of ∇F, evaluated at some initial guess $\mathbf{x}_0$, should be subtracted from $\mathbf{x}_0$. This process is repeated until some threshold of accuracy is reached, such as $F(\mathbf{x}_{n+1}) - F(\mathbf{x}_n) < \epsilon$ or $\|\nabla F(\mathbf{x}_n)\| < \epsilon$, where ϵ is a small positive number (see Figure 3.1). To see that subtracting a fraction of ∇F from $\mathbf{x}_n$ will reduce the value of F consider the Taylor series approximation of $F(\mathbf{x}_{n+1})$ with $0 < \zeta < 1$:

$$\begin{aligned} F(\mathbf{x}_{n+1}) &= F(\mathbf{x}_n - \zeta \nabla F[\mathbf{x}_n]) \\ &\approx F(\mathbf{x}_n) - \zeta \nabla F(\mathbf{x}_n)^T \nabla F(\mathbf{x}_n) \\ &= F(\mathbf{x}_n) - \zeta \|\nabla F(\mathbf{x}_n)\|^2. \end{aligned} \tag{3.1}$$

As $\|\nabla F(\mathbf{x}_n)\|^2 \geq 0$, $F(\mathbf{x}_{n+1}) \leq F(\mathbf{x}_n)$ for sufficiently small ζ such that the Taylor series approximation is valid.

There are many approaches to numerical optimization. The one implemented for

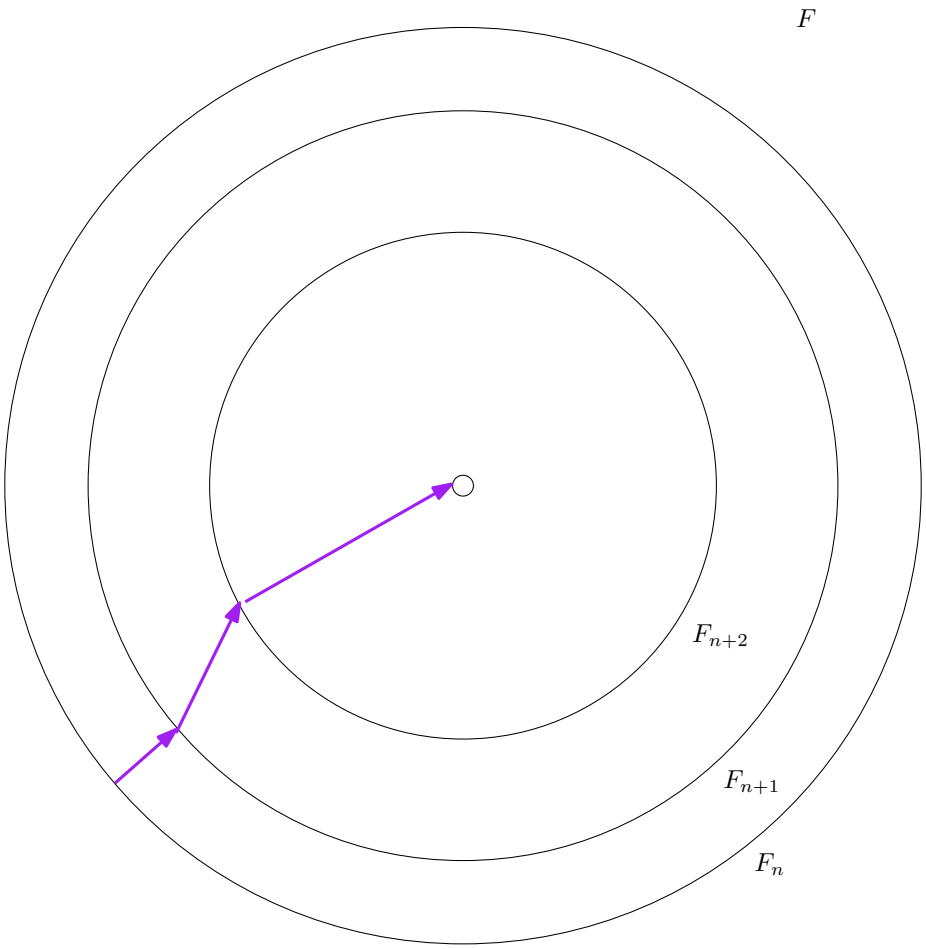

Figure 3.1: Diagram detailing steepest descent. All points on a line are of equal value for the function F. Steepest descent makes successive estimates of the value of $\mathbf{x}$ which minimizes F.

this project was the steepest descent line search method. Line search methods start from a particular point and head in a direction in search of another point which reduces or, in the case of maximization, increases the value of the target function, F.

Search direction determination distinguishes the various methods. The steepest descent method chooses the negative of the gradient of the target function, $-\nabla F(\mathbf{x}_n)$, as its search direction.

Other line search methods include Newton's method which requires the calculation of the Hessian, the matrix containing the second-order partial derivatives of the function F. Calculation of the Hessian can be time-consuming and error-ridden. In Newton's method the search direction is $-\left(\nabla^2 F\left[\mathbf{x}_n\right]\right)^{-1} \nabla F(\mathbf{x}_n)$ where $\nabla^2 F\left(\mathbf{x}_n\right)$ is the Hessian. The limited-memory Broyden–Fletcher–Goldfarb–Shanno method (L-

BFGS) is another well-regarded line search algorithm, but it uses an approximation of the Hessian and suffers from similar drawbacks as Newton's method [36].

Steepest descent is an unconstrained optimization method. As the spins are treated classically with unit length, optimizing the spin Cartesian components is not possible with this algorithm. Instead, each classical spin is described in spherical coordiates via two angles, ϕ, the azimuthal angle and α, the polar angle (see Figure 3.2). The Hamiltonian is written in terms of these angles and then minimized.

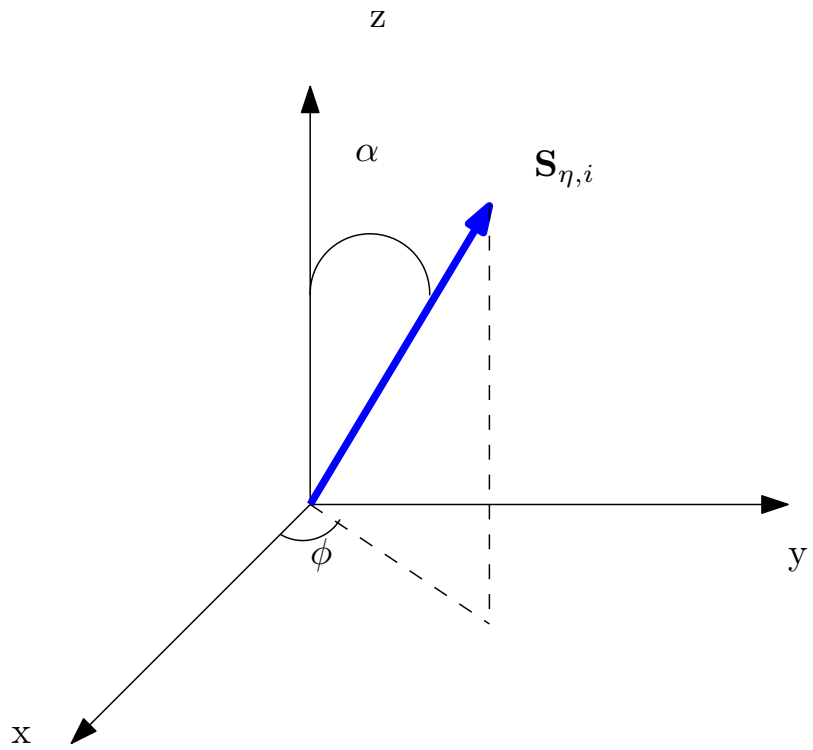

Figure 3.2: Coordinate system for spin used in simulations. The spin has unit length and is described solely by its azimuthal, ϕ, and polar, α, angles.

3.1.1 Adaptive Step Size

In an attempt to reach the energy minimum of the system as quickly as possible, the Armijo condition,

$$F\left(\mathbf{x}_n + \zeta_n \mathbf{p}_n\right) \leq F\left(\mathbf{x}_n\right) + c\zeta_n \nabla F_n^T \mathbf{p}_n, \tag{3.2}$$

was implemented. This ensured that sufficient progress was made in each minimization step.

This says that the function evaluated at the new guess for the minimum point must be less than or equal to the function at the previous guess at the estimation plus the gradient of the function evaluated at the old guess multiplied by the search direction and the step size, multiplied by some coefficient c between 0 and 1. It is used in a backtracking line search where the step size is reduced until the Armijo condition is met. ζ is reduced until the condition in Equation (3.2) is met. $\mathbf{p}_n$ is the search direction ($\mathbf{p}_n = -\nabla F[\mathbf{x}_n]$ for steepest descent). These steps are summarized in Algorithm 1.

Make initial guess for $\mathbf{x}$; select $\epsilon > 0$; select $\zeta, c, r \in (0, 1)$
while $\|\nabla F\|^2 > \epsilon$ **do**
  while $F(\mathbf{x} - \zeta \nabla F) > F(\mathbf{x}) - c\zeta \|\nabla F\|$ **do**
    $\zeta \leftarrow r\zeta$
  end while
  $\mathbf{x} \leftarrow \mathbf{x} - \zeta \nabla F$
  $F(\mathbf{x}) \leftarrow F(\mathbf{x} - \zeta \nabla F)$
end while

Algorithm 1: Steepest descent algorithm with Armijo condition

3.1.2 Challenges of Steepest Descent

The advantage steepest descent holds over many other line search methods is the lack of needing to find the second derivative of the function to be minimized. Of course, that still leaves the task of finding the first derivative of the function. For a function such as the Hamiltonian of Chapter 2, the task is not necessarily simple. There are multiple terms to evaluate and many places for errors to enter.

Additionally, the method is susceptible to becoming stuck in local minima. As the termination condition is that the gradient become smaller than some predetermined value, the first instance where this occurs during the running of the program will lead to the program exitting regardless whether this is the gloabal or a local minimum. This means that the initial guess for $\mathbf{x}_0$ is crucial. A poorly selected starting point may converge to a point well away from the actual solution.

Knowing characteristics of the final answer, in this case, reasonable and unreasonable spin arrangements, is advantageous to minimization. It would allow for a reasonable initial guess at a solution to be made. This would allow for quicker convergence. Also, knowing characteristics of the final answer would allow for an assessment to be

made of the appropriateness of any final answer.

3.2 Monte Carlo Simulations

Attempts were also made to perform Monte Carlo simulations. In the simulations, the same Hamiltonian presented in Chapter 2 was used as the energy. From an initial state, a single spin state was randomly selected and its orientation was randomly altered. If the change reduced the energy of the system, it was retained. Otherwise, the system reverted to the previous state. This continued for a determined number of iterations.

While this approach was far less challenging to implement than steepest descent, owing to the fact that no derivatives of the Hamiltonian needed to be calculated, it proved to be much slower than steepest descent in lowering the energy of the system. This was somewhat foreseeable due to the stocastic nature of Monte Carlo.

The Monte Carlo results provide means by which to compare results derived from steepest descent methods. The simplicity of executing Monte Carlo means that it should be capable of finding the ground state of any system with a known Hamiltonian, it just may take many iterations to reach the ground state.

Many additional iterations might need to be performed when nearing the ground state to have make incremental progress. Since spins are randomly selected, there is no way to ensure that all spins are visited. Even if all spins are visited, because the change in the spin is random, there is no manner by which to assure that the necessary orientation for a certain spin is attained in a suitable timeframe. That is, many visits to a spin are needed to exhaust all possible orientations.

Figure 3.3 shows the disparity in the approaches. A $20 \times 20 \times 20$ spin structure starting from a random configuration was minimized using Monte Carlo and steepest descent methods. The Monte Carlo approach needed one million spin iterations to just fall short of -3 units of energy per spin for the configuration ($D/J = 1.1$). It took less than 20 iterations (with a different randomized spin configuration) for the steepest descent apporach to better the Monte Carlo one. In all, the Monte Carlo approach took over eight hours of runtime to minimize the cube of spins inferiorly to what the steepest descent method did in four minutes.

It was evident from such case studies that Monte Carlo methods were not the best approach for the intended project. It would be more appropriate to use Monte Carlo methods if the system was thermalized or if spins were restricted to being up

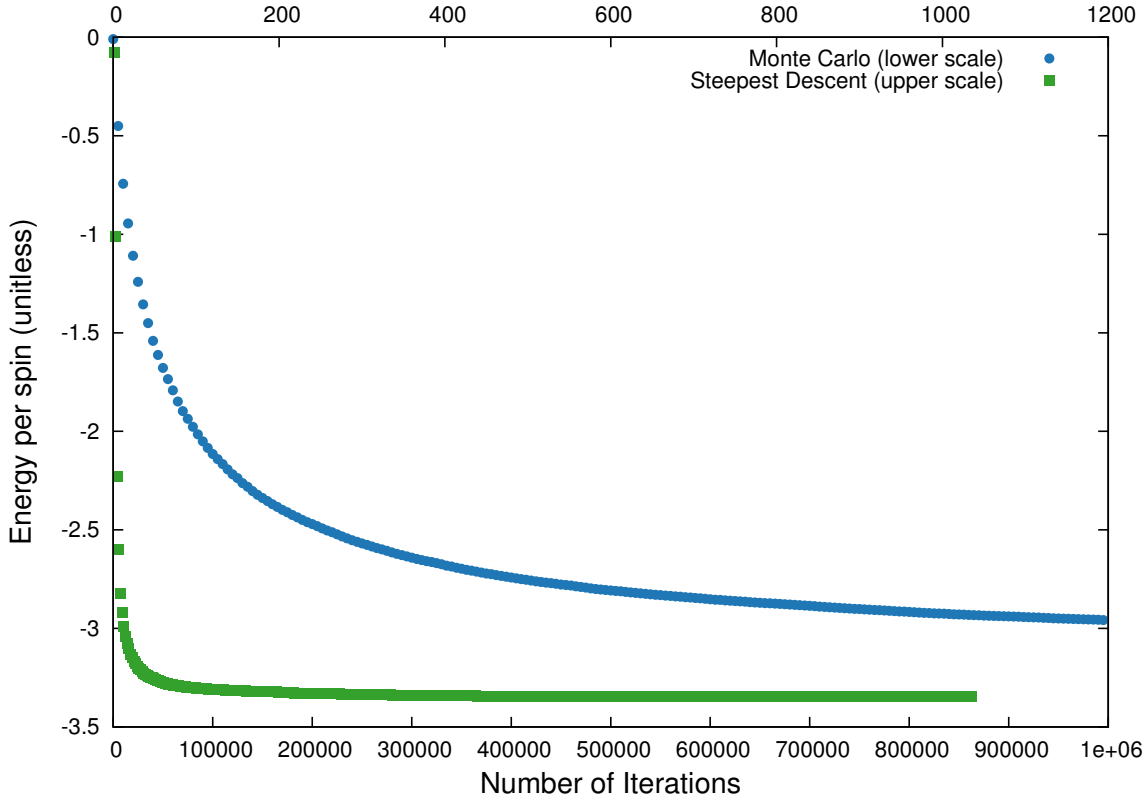

Figure 3.3: Energy per spin versus number of iterations. $\frac{D}{J} = 1.1$, $D' = A = 0$ and no applied fields. Comparison of speed of Monte Carlo methods versus steepest descent. Starting from a random spin configuration and the same Hamiltonian, a $20 \times 20 \times 20$ spin structure was minimized. It took over eight hours to produce the data from the Monte Carlo methods. The data from the steepest descent method were produced in four minutes.

or down.

3.3 Algorithm for Finding Ground State of BFO

The algorithm for finding the spin configuration of BFO with applied fields was written in Fortran. The Hamiltonian developed in Chapter 2 was used as the function to minimize via the method of steepest descent (as described in Section 3.1). Each spin was considered to have unit length and its orientation was described by two angles: ϕ, the azimuthal and α, the polar.

An initial spin configuration guess was made to initiate the steepest descent algorithm. Then the gradient of the Hamiltonian with respect to the $2N$ variables of

the system, the angles, was calculated. The square of the modulus of the gradient of the Hamiltonian was compared to a determined threshold value. If it was above the threshold, then the system would iterate with $\phi_{\eta,i}$ and $\alpha_{\eta,i}$ changed per Section 3.1 until the threshold value for gradient of the Hamiltonian was met.

When the system is described in terms of the angles of the spins in terms of the BFO rhombohedral coordinates, then the spins may be represented as

$$\mathbf{S}_{\eta,i} = \cos\phi_{\eta,i}\sin\alpha_{\eta,i}\hat{\mathbf{X}} + \sin\phi_{\eta,i}\sin\alpha_{\eta,i}\hat{\mathbf{Y}} + \cos\alpha_{\eta,i}\hat{\mathbf{Z}}. \tag{3.3}$$

Substitution into Equation (2.1) leads to

$$\begin{aligned}
H = &\sum_i\sum_{\boldsymbol{\delta}}\left(J\mathbf{S}_{1,i}\cdot\mathbf{S}_{2,i+\boldsymbol{\delta}} + \left[D\left\{\hat{\mathbf{Z}}\times\frac{(\boldsymbol{\tau}+\boldsymbol{\delta})}{a_{Rh}}\right\} + D'\,\hat{\mathbf{Z}}\right]\cdot\left[\mathbf{S}_{1,i}\times\mathbf{S}_{2,i+\boldsymbol{\delta}}\right]\right)\\
&- \frac{A}{2}\sum_i\sum_{\eta=1,2}\left(\mathbf{S}_{\eta,i}\cdot\hat{\mathbf{Z}}\right)^2 - g\mu_B\sum_i\sum_{\eta=1,2}\left(\mathbf{S}_{\eta,i}\cdot\mathbf{B}\right)\\
&- \frac{\xi}{4}\sum_i\sum_{\eta=1,2}\left(\mathbf{E}_\perp\cdot\left[\left\{\left(S^Y_{\eta,i}\right)^2 - \left(S^X_{\eta,i}\right)^2\right\}\hat{\mathbf{X}} + 2S^X_{\eta,i}S^Y_{\eta,i}\hat{\mathbf{Y}}\right]\right.\\
&\left.+\, 2\sqrt{2}\mathbf{E}_\perp\cdot\left[S^X_{\eta,i}\hat{\mathbf{X}} + S^Y_{\eta,i}\hat{\mathbf{Y}}\right]S^Z_{\eta,i}\right)\\
= &\sum_i\sum_{\boldsymbol{\delta}}\left(J\left[\left\{\cos\phi_{1,i}\cos\phi_{2,i+\boldsymbol{\delta}} + \sin\phi_{1,i}\sin\phi_{2,i+\boldsymbol{\delta}}\right\}\sin\alpha_{1,i}\sin\alpha_{2,i+\boldsymbol{\delta}}\right.\right.\\
&\left.+\,\cos\alpha_{1,i}\cos\alpha_{2,i+\boldsymbol{\delta}}\right] + \left[D\left\{\hat{\mathbf{Z}}\times\frac{(\boldsymbol{\tau}+\boldsymbol{\delta})}{a_{Rh}}\right\} + D'\,\hat{\mathbf{Z}}\right]\\
&\cdot\left[\left\{\sin\phi_{1,i}\sin\alpha_{1,i}\cos\alpha_{2,i+\boldsymbol{\delta}} - \cos\alpha_{1,i}\sin\phi_{2,i+\boldsymbol{\delta}}\sin\alpha_{2,i+\boldsymbol{\delta}}\right\}\hat{\mathbf{X}}\right.\\
&+\left\{\cos\alpha_{1,i}\cos\phi_{2,i+\boldsymbol{\delta}}\sin\alpha_{2,i+\boldsymbol{\delta}} - \cos\phi_{1,i}\sin\alpha_{1,i}\cos\alpha_{2,i+\boldsymbol{\delta}}\right\}\hat{\mathbf{Y}}\\
&\left.+\left\{\cos\phi_{1,i}\sin\phi_{2,i+\boldsymbol{\delta}} - \sin\phi_{1,i}\cos\phi_{2,i+\boldsymbol{\delta}}\right\}\sin\alpha_{1,i}\sin\alpha_{2,i+\boldsymbol{\delta}}\hat{\mathbf{Z}}\right]\\
&- \frac{A}{2}\sum_i\sum_{\eta=1,2}\cos^2\alpha_{\eta,i}\\
&- g\mu_B\sum_i\sum_{\eta=1,2}\left(\left[B^X\cos\phi_{\eta,i} + B^Y\sin\phi_{\eta,i}\right]\sin\alpha_{\eta,i} + B^Z\cos\alpha_{\eta,i}\right)\\
&- \frac{\xi}{4}\sum_i\sum_{\eta=1,2}\left(\mathbf{E}_\perp\cdot\left[\left\{\sin^2\phi_{\eta,i} - \cos^2\phi_{\eta,i}\right\}\sin^2\alpha_{\eta,i}\hat{\mathbf{X}}\right.\right.\\
&\left.+\,2\sin\phi_{\eta,i}\cos\phi_{\eta,i}\sin^2\alpha_{\eta,i}\hat{\mathbf{Y}}\right]\\
&\left.+\,2\sqrt{2}\mathbf{E}_\perp\cdot\left[\cos\phi_{\eta,i}\hat{\mathbf{X}} + \sin\phi_{\eta,i}\hat{\mathbf{Y}}\right]\sin\alpha_{\eta,i}\cos\alpha_{\eta,i}\right)
\end{aligned}$$

$$
\begin{aligned}
&= \sum_i \sum_{\boldsymbol{\delta}} \big(J \left[\cos\left\{ \phi_{1,i} - \phi_{2,i+\boldsymbol{\delta}} \right\} \sin\alpha_{1,i} \sin\alpha_{2,i+\boldsymbol{\delta}} + \cos\alpha_{1,i} \cos\alpha_{2,i+\boldsymbol{\delta}} \right] \\
&\quad + D \left[\hat{\mathbf{Z}} \times \frac{\{\boldsymbol{\tau} + \boldsymbol{\delta}\}}{a_{Rh}} \right] \\
&\quad \cdot \Big[\left\{ \sin\phi_{1,i} \sin\alpha_{1,i} \cos\alpha_{2,i+\boldsymbol{\delta}} - \cos\alpha_{1,i} \sin\phi_{2,i+\boldsymbol{\delta}} \sin\alpha_{2,i+\boldsymbol{\delta}} \right\} \hat{\mathbf{X}} \\
&\quad + \left\{ \cos\alpha_{1,i} \cos\phi_{2,i+\boldsymbol{\delta}} \sin\alpha_{2,i+\boldsymbol{\delta}} - \cos\phi_{1,i} \sin\alpha_{1,i} \cos\alpha_{2,i+\boldsymbol{\delta}} \right\} \hat{\mathbf{Y}} \Big] \\
&\quad + D' \sin\left[\phi_{2,i+\boldsymbol{\delta}} - \phi_{1,i} \right] \sin\alpha_{1,i} \sin\alpha_{2,i+\boldsymbol{\delta}} \big) \\
&\quad - \frac{A}{2} \sum_i \sum_{\eta=1,2} \cos^2\alpha_{\eta,i} \\
&\quad - g\mu_B \sum_i \sum_{\eta=1,2} \left(\left[B^X \cos\phi_{\eta,i} + B^Y \sin\phi_{\eta,i} \right] \sin\alpha_{\eta,i} + B^Z \cos\alpha_{\eta,i} \right) \\
&\quad - \frac{\xi}{4} \sum_i \sum_{\eta=1,2} \Big(\mathbf{E}_\perp \cdot \left[\sin 2\phi_{\eta,i} \hat{\mathbf{Y}} - \cos 2\phi_{\eta,i} \hat{\mathbf{X}} \right] \sin^2\alpha_{\eta,i} \\
&\quad + \sqrt{2} \mathbf{E}_\perp \cdot \left[\cos\phi_{\eta,i} \hat{\mathbf{X}} + \sin\phi_{\eta,i} \hat{\mathbf{Y}} \right] \sin 2\alpha_{\eta,i} \Big) .
\end{aligned} \tag{3.4}
$$

The derivatives with respect to the angles are

$$
\begin{aligned}
\frac{\partial H}{\partial \phi_{\eta,i}} &= \sum_{\boldsymbol{\delta}} \big(-J \sin\left[\phi_{\eta,i} - \phi_{\rho,i+\boldsymbol{\delta}} \right] \sin\alpha_{\eta,i} \sin\alpha_{\rho,i+\boldsymbol{\delta}} \\
&\quad + D \left[\hat{\mathbf{Z}} \times \frac{\{\boldsymbol{\tau} + \boldsymbol{\delta}\}}{a_{Rh}} \right] \cdot \Big[\cos\phi_{\eta,i} \sin\alpha_{\eta,i} \cos\alpha_{\rho,i+\boldsymbol{\delta}} \hat{\mathbf{X}} \\
&\quad + \sin\phi_{\eta,i} \sin\alpha_{\eta,i} \cos\alpha_{\rho,i+\boldsymbol{\delta}} \hat{\mathbf{Y}} \Big] - D' \cos\left[\phi_{\rho,i+\boldsymbol{\delta}} - \phi_{\eta,i} \right] \sin\alpha_{\eta,i} \sin\alpha_{\rho,i+\boldsymbol{\delta}} \Big) \\
&\quad + g\mu_B \left(B^X \sin\phi_{\eta,i} - B^Y \cos\phi_{\eta,i} \right) \sin\alpha_{\eta,i} \\
&\quad - \frac{\xi}{4} \Big(2\, \mathbf{E}_\perp \cdot \left[\sin 2\phi_{\eta,i} \hat{\mathbf{X}} + \cos 2\phi_{\eta,i} \hat{\mathbf{Y}} \right] \sin^2\alpha_{\eta,i} \\
&\quad + \sqrt{2} \mathbf{E}_\perp \cdot \left[\cos\phi_{\eta,i} \hat{\mathbf{Y}} - \sin\phi_{\eta,i} \hat{\mathbf{X}} \right] \sin 2\alpha_{\eta,i} \Big)
\end{aligned} \tag{3.5}
$$

and

$$
\begin{aligned}
\frac{\partial H}{\partial \alpha_{\eta,i}} &= \sum_{\boldsymbol{\delta}} \big(J \left[\cos\left\{ \phi_{\eta,i} - \phi_{\rho,i+\boldsymbol{\delta}} \right\} \cos\alpha_{\eta,i} \sin\alpha_{\rho,i+\boldsymbol{\delta}} - \sin\alpha_{\eta,i} \cos\alpha_{\rho,i+\boldsymbol{\delta}} \right] \\
&\quad + D \left[\hat{\mathbf{Z}} \times \frac{\{\boldsymbol{\tau} + \boldsymbol{\delta}\}}{a_{Rh}} \right] \\
&\quad \cdot \Big[\left\{ \sin\phi_{\eta,i} \cos\alpha_{\eta,i} \cos\alpha_{\rho,i+\boldsymbol{\delta}} + \sin\alpha_{\eta,i} \sin\phi_{\rho,i+\boldsymbol{\delta}} \sin\alpha_{\rho,i+\boldsymbol{\delta}} \right\} \hat{\mathbf{X}} \\
&\quad - \left\{ \sin\alpha_{\eta,i} \cos\phi_{\rho,i+\boldsymbol{\delta}} \sin\alpha_{\rho,i+\boldsymbol{\delta}} + \cos\phi_{\eta,i} \cos\alpha_{\eta,i} \cos\alpha_{\rho,i+\boldsymbol{\delta}} \right\} \hat{\mathbf{Y}} \Big]
\end{aligned}
$$

$$
\begin{aligned}
&+ D' \sin\left[\phi_{\rho,i+\boldsymbol{\delta}} - \phi_{\eta,i}\right] \cos\alpha_{\eta,i} \sin\alpha_{\rho,i+\boldsymbol{\delta}}) \\
&+ \frac{A}{2} \sin 2\alpha_{\eta,i} - g\mu_B \left(\left[B^X \cos\phi_{\eta,i} + B^Y \sin\phi_{\eta,i}\right] \cos\alpha_{\eta,i} - B^Z \sin\alpha_{\eta,i}\right) \\
&- \frac{\xi}{4} \Big(\mathbf{E}_\perp \cdot \left[\sin 2\phi_{\eta,i}\hat{\mathbf{Y}} - \cos 2\phi_{\eta,i}\hat{\mathbf{X}}\right] \\
&+ 2\sqrt{2}\mathbf{E}_\perp \cdot \left[\cos\phi_{\eta,i}\hat{\mathbf{X}} + \sin\phi_{\eta,i}\hat{\mathbf{Y}}\right]\Big) \sin 2\alpha_{\eta,i}. \qquad (3.6)
\end{aligned}
$$

ρ represents the other sublattice: if $\eta = 1$ then $\rho = 2$ and vice versa. For each spin site, the iterative value of the two angles was updated using the derivatives of the Hamiltonian:

$$\phi_{\eta,i;n+1} = \phi_{\eta,i;n} - \zeta_n \frac{\partial H}{\partial \phi_{\eta,i;n}} \qquad (3.7)$$

and

$$\alpha_{\eta,i;n+1} = \alpha_{\eta,i;n} - \zeta_n \frac{\partial H}{\partial \alpha_{\eta,i;n}}. \qquad (3.8)$$

The iterative process continued until the threshold value of $\|H\|^2$ was obtained. At that point the state was analyzed to determine whether it was cycloidal or homogeneous.

Due to the potential for steepest descent to be trapped in local minima, the programs used multiple initial configurations and simultaneous runs to try to attain the global minimum for the system for the inputted parameters. Initial starting points generally included the planar-harmonic cycloids with propagation vectors along the three conventional directions $\left[1\bar{1}0\right]$, $\left[10\bar{1}\right]$ and $\left[01\bar{1}\right]$ and homogeneous ordering.

Once all of the the minimizations (starting from different initial conditions) were performed, a program was executed to determine which set of results produced the lowest energy. This configuration was taken to be the ground state spin arrangement for the given parameters. Fourier analysis was then performed on the results.

3.4 Analysis of Algorithm Results

Fourier analysis was employed to make distinctions between the two states, cycloidal and homogeneous. Fast Fourier transforms (FFTs) were performed on the data produced from the simulations. A harmonic cycloid would have two peaks equidistant from the origin in its Fourier profile. A homogeneous cycloid would have a single peak at the origin. Due to the discrete nature of the data, there will be broadening of peaks. Windowing and zero padding were introduced in an attempt to reduce this.

3.4.1 Zero Padding

Zero padding is the addition of null results to data before performing a Fourier transform. The intent is to refine the resulting transform so as to get more accurate results. Spins with values of zero were added to the cube of non-zero simulated spins.

3.4.2 Windowing

Windowing is used to counteract the effects of a periodic signal which abruptly ceases. This is the case with the simulated cube of spins. There is a periodic nature to the spin arrangement and then it stops. Left untreated, the FFTs would have peaks in unanticipated places due to the abrupt cessation of the pattern. These artifacts are undesirable and, as such, a window function was applied to the data. Specifically, the Hann window was used. Effectively, the window weighted spins in the centre of the cube where there is a periodic patterns surrounding them more heavily than spins near the edges of the cube which does not have as many spins maintaining the pattern surrounding them. The one-dimensional Hann function is

$$w\left(n_i\right) = \frac{1}{2}\left(1 - \cos\left[\frac{2\pi n_i}{N_i - 1}\right]\right). \tag{3.9}$$

The three-dimensional function has the form

$$\begin{aligned} w\left(n_x, n_y, n_z\right) = \frac{1}{8}&\left(1 - \cos\left[\frac{2\pi n_x}{N_x - 1}\right]\right)\left(1 - \cos\left[\frac{2\pi n_y}{N_y - 1}\right]\right) \\ &\times \left(1 - \cos\left[\frac{2\pi n_z}{N_z - 1}\right]\right). \end{aligned} \tag{3.10}$$

Equation (3.10) displays the weighting for the spins. In this notation, $n_i \in [0, N_i - 1]$. The values of the spins were multiplied by Equation (3.10) before the FFT was performed.

3.4.3 Fast Fourier Transform

The software FFTW (Fastest Fourier Transform in the West) was used to produce the FFTs. Analysis of the resultant FFTs allowed for value of the average value of the modulus of $\mathbf{Q}$, $\langle \|\mathbf{Q}\| \rangle$, which should be non-zero for a cycloid and zero for homogeneous ordering.

The Fourier transform of the spin takes the following form:

$$\tilde{\mathbf{S}}_{\eta,\mathbf{k}} = \frac{1}{\sqrt{M}} \sum_{\mathbf{R}} e^{\imath \mathbf{k}\cdot\mathbf{R}} \mathbf{S}_{\eta,\mathbf{R}}. \tag{3.11}$$

Its inverse has the form

$$\mathbf{S}_{\eta,\mathbf{R}} = \frac{1}{\sqrt{M}} \sum_{\mathbf{k}} e^{-\imath \mathbf{k}\cdot\mathbf{R}} \tilde{\mathbf{S}}_{\eta,\mathbf{k}}, \tag{3.12}$$

where M is the number of spin sites in the Fourier transform. This number is different than the number of spins in the simulation due to the zero padding. $\mathbf{k}$ is the wave vector and $\mathbf{R}$ is the position of the spin:

$$\begin{aligned} \mathbf{R} &= a_{Rh} \left(n_x \hat{\mathbf{x}} + n_y \hat{\mathbf{y}} + n_z \hat{\mathbf{z}} \right) \\ &= a_{Rh} \left(n_1 \left[\hat{\mathbf{y}} + \hat{\mathbf{z}} \right] + n_2 \left[\hat{\mathbf{x}} + \hat{\mathbf{z}} \right] + n_3 \left[\hat{\mathbf{x}} + \hat{\mathbf{y}} \right] \right). \end{aligned} \tag{3.13}$$

$\mathbf{R} = \mathbf{R}_{1,i}$ was used for both sublattices so that an accurate comparison could be made between transforms of different sublattices. $n_m \in \left[-\frac{N_m}{2} + 1, \frac{N_m}{2} \right]$ where N_m is the number of spins along the coordinate m. Due to how spins are assigned values in the program, it is necessary to take the FFT of the spin configuration in terms of n_1, n_2 and n_3 and then convert to n_x, n_y and n_z. From Equation (3.13),

$$n_x = n_2 + n_3, \tag{3.14a}$$

$$n_y = n_1 + n_3, \tag{3.14b}$$

$$n_z = n_1 + n_2. \tag{3.14c}$$

And written in terms of n_x, n_y and n_z,

$$n_1 = \frac{n_y + n_z - n_x}{2}, \tag{3.15a}$$

$$n_2 = \frac{n_x + n_z - n_y}{2}, \tag{3.15b}$$

$$n_3 = \frac{n_x + n_y - n_z}{2}. \tag{3.15c}$$

The Fourier transform can then be re-written in terms of n_1, n_2 and n_3:

$$\tilde{\mathbf{S}}_{\eta,\mathbf{k}} = \frac{1}{\sqrt{M}} \sum_{\mathbf{R}} e^{\imath \mathbf{k}\cdot\mathbf{R}} \mathbf{S}_{\eta,\mathbf{R}}$$

$$= \frac{1}{\sqrt{M}} \sum_{n_x,n_y,n_z} e^{\imath a_{Rh}(k_x n_x + k_y n_y + k_z n_z)} \mathbf{S}_{\eta;n_x,n_y,n_z}$$
$$= \frac{1}{\sqrt{M}} \sum_{n_1,n_2,n_3} e^{\imath a_{Rh}(k_x[n_2+n_3] + k_y[n_1+n_3] + k_z[n_1+n_2])} \mathbf{S}_{\eta;n_1,n_2,n_3}$$
$$= \frac{1}{\sqrt{M}} \sum_{n_1,n_2,n_3} e^{\imath a_{Rh}(k_1 n_1 + k_2 n_2 + k_3 n_3)} \mathbf{S}_{\eta;n_1,n_2,n_3}. \tag{3.16}$$

From Equation (3.16), k_1, k_2 and k_3 can be defined:

$$k_1 = k_y + k_z, \tag{3.17a}$$
$$k_2 = k_x + k_z, \tag{3.17b}$$
$$k_3 = k_x + k_y. \tag{3.17c}$$

In terms of k_1, k_2 and k_3,

$$k_x = \frac{k_2 + k_3 - k_1}{2}, \tag{3.18a}$$
$$k_y = \frac{k_1 + k_3 - k_2}{2}, \tag{3.18b}$$
$$k_z = \frac{k_1 + k_2 - k_3}{2}. \tag{3.18c}$$

The FFT output of the program is of k_1, k_2 and k_3 and from Equation (3.18), this can be used to find k_x, k_y and k_z.

To find the average of the modulus of $\mathbf{Q}$, the Fourier components at all k-points are evaluated along with the value of $\mathbf{k}$:

$$\langle \|\mathbf{Q}_\eta\| \rangle = \sqrt{\sum_{\mathbf{k}} \tilde{\mathbf{S}}^2_{\eta,\mathbf{k}} \mathbf{k}^2}. \tag{3.19}$$

$\tilde{\mathbf{L}}_\mathbf{k}$ and $\tilde{\mathbf{M}}_\mathbf{k}$ can also be defined:

$$\tilde{\mathbf{L}}_\mathbf{k} = \tilde{\mathbf{S}}_{1,\mathbf{k}} - \tilde{\mathbf{S}}_{2,\mathbf{k}} \tag{3.20}$$

and

$$\tilde{\mathbf{M}}_\mathbf{k} = \tilde{\mathbf{S}}_{1,\mathbf{k}} + \tilde{\mathbf{S}}_{2,\mathbf{k}}. \tag{3.21}$$

These functions indicate at which points in reciprocal space there is antiferromagnetic

$\left(\tilde{\mathbf{L}}_{\mathbf{k}}\right)$ or ferromagnetic $\left(\tilde{\mathbf{M}}_{\mathbf{k}}\right)$ character. For a harmonic cycloid, peaks would be expected at $\mathbf{k} = \pm\mathbf{Q}$ for $\tilde{\mathbf{L}}_{\mathbf{k}}$ and $\tilde{\mathbf{M}}_{\mathbf{k}} = \mathbf{0}$ for all $\mathbf{k}$. For a homogeneous antiferromagnet, there should be a peak at $\mathbf{k} = \mathbf{0}$ for $\tilde{\mathbf{L}}_{\mathbf{k}}$ and $\tilde{\mathbf{M}}_{\mathbf{k}} = \mathbf{0}$ for all $\mathbf{k}$. Figures 3.4 and 3.5 depict the results of FFTs of the ground states for $\frac{D}{J} = \frac{2\pi}{5}$, $\frac{D'}{J} = 0.60$, $\frac{A}{J} = 0$, $\frac{\xi}{J} = 5.77 \times 10^{-5}$ cm V^{-1} with an applied electric field $\left(\mathbf{E}_{\perp} = -4.0 \times 10^{4}\ \text{V cm}^{-1}\hat{\mathbf{X}}\right)$ and without. In Figure 3.4, there are no applied fields, and the ground state appears to be a planar cycloid with $\langle\|\mathbf{Q}\|\rangle = 1.35$ and two distinct off-centre peaks are visible. The FFT is symmetric about $\mathbf{k} = \mathbf{0}$ with two peaks as required by the condition that the spin state is a real vector. In Figure 3.5, there is a central peak and $\langle\|\mathbf{Q}\|\rangle = 0.33$. It would be expected that in a homogeneous system, there would be a central peak as, ideally, $\langle\|\mathbf{Q}\|\rangle$ would be equal to zero.

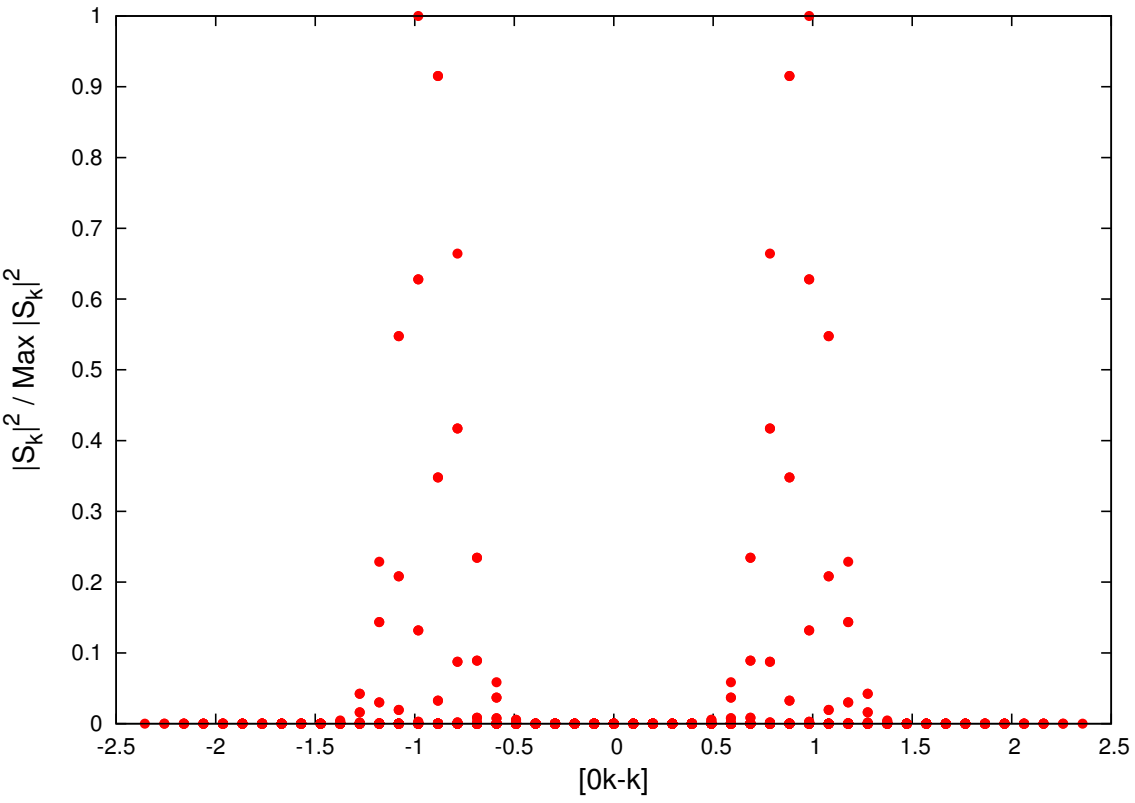

Figure 3.4: FFT along $\left[01\bar{1}\right]$ direction. $\langle\|\mathbf{Q}\|\rangle$ is 1.35.

In order to interpret this result, consider the harmonic and planar cycloid:

$$\mathbf{S}_{\eta,\mathbf{R}} = (-1)^{\eta+1}\left(\cos\left[\mathbf{Q}\cdot\mathbf{R}\right]\hat{\mathbf{Z}} + \sin\left[\mathbf{Q}\cdot\mathbf{R}\right]\hat{\mathbf{Q}}\right). \tag{3.22}$$

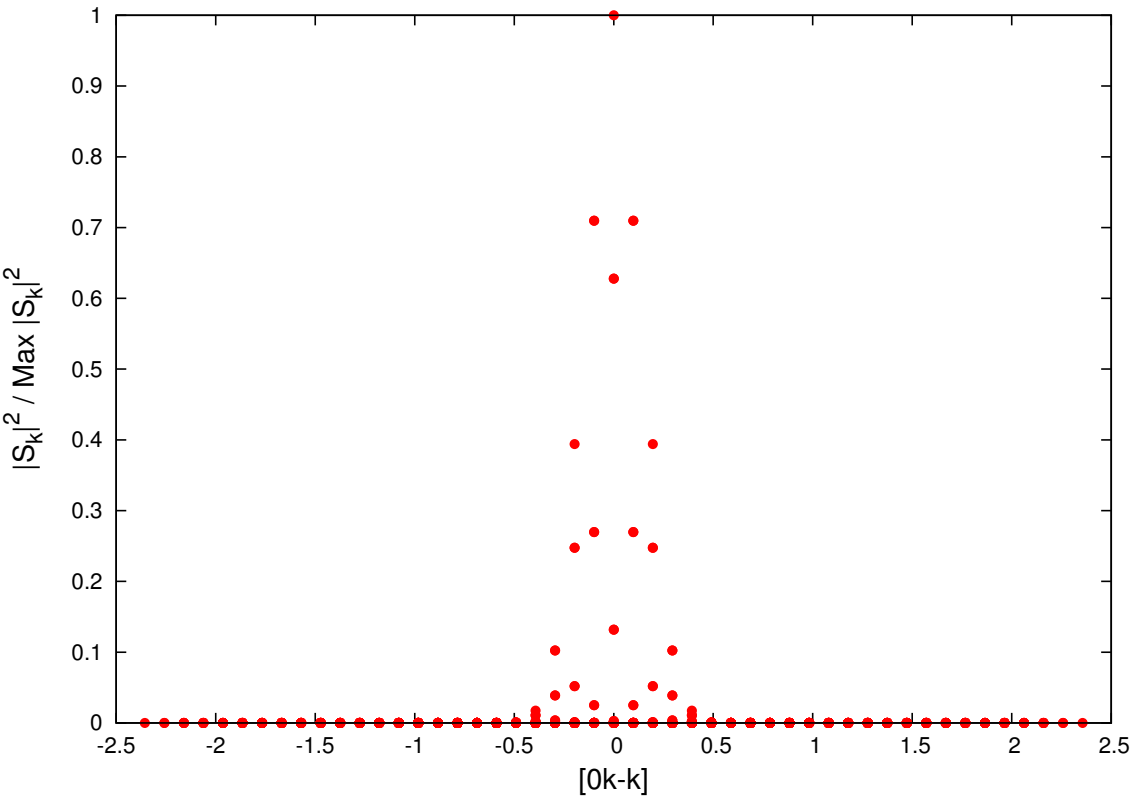

Figure 3.5: FFT along $[01\bar{1}]$ direction. $\langle\|\mathbf{Q}\|\rangle$ is 0.33.

This can be placed into Equation (3.11) to find the dependence of $\mathbf{Q}$ on the FFT:

$$\begin{aligned}\tilde{\mathbf{S}}_{\eta,\mathbf{k}} &= \frac{1}{\sqrt{M}}\sum_{\mathbf{R}} e^{\imath\mathbf{k}\cdot\mathbf{R}}\mathbf{S}_{\eta,\mathbf{R}} \\ &= \frac{(-1)^{\eta+1}\sqrt{M}}{2}\left(\delta_{\mathbf{k},-\mathbf{Q}}\left[\hat{\mathbf{Z}}-\imath\hat{\mathbf{Q}}\right]+\delta_{\mathbf{k},\mathbf{Q}}\left[\hat{\mathbf{Z}}+\imath\hat{\mathbf{Q}}\right]\right) \qquad (3.23)\end{aligned}$$

For a cycloid with propagation vector $\mathbf{Q}$, the Fourier transform is a pair of delta functions at $\mathbf{k}=\pm\mathbf{Q}$ with a real component in the $\hat{\mathbf{Z}}$ direction and an imaginary one in the $\hat{\mathbf{Q}}$. From here, the modulus squared can be found:

$$\begin{aligned}\|\tilde{\mathbf{S}}_{\eta,\mathbf{k}}\|^2 &= \tilde{\mathbf{S}}_{\eta,\mathbf{k}}\tilde{\mathbf{S}}^*_{\eta,\mathbf{k}} \\ &= \frac{M}{4}\left(\delta_{\mathbf{k},-\mathbf{Q}}\left[\hat{\mathbf{Z}}-\imath\hat{\mathbf{Q}}\right]+\delta_{\mathbf{k},\mathbf{Q}}\left[\hat{\mathbf{Z}}+\imath\hat{\mathbf{Q}}\right]\right)\left(\delta_{\mathbf{k},-\mathbf{Q}}\left[\hat{\mathbf{Z}}+\imath\hat{\mathbf{Q}}\right]+\delta_{\mathbf{k},\mathbf{Q}}\left[\hat{\mathbf{Z}}-\imath\hat{\mathbf{Q}}\right]\right) \\ &= \frac{M}{4}\left(\delta_{\mathbf{k},-\mathbf{Q}}\delta_{\mathbf{k},-\mathbf{Q}}\left[\hat{\mathbf{Z}}-\imath\hat{\mathbf{Q}}\right]\left[\hat{\mathbf{Z}}+\imath\hat{\mathbf{Q}}\right]+\delta_{\mathbf{k},-\mathbf{Q}}\delta_{\mathbf{k},\mathbf{Q}}\left[\hat{\mathbf{Z}}-\imath\hat{\mathbf{Q}}\right]\left[\hat{\mathbf{Z}}-\imath\hat{\mathbf{Q}}\right]\right. \\ &\quad\left.+\,\delta_{\mathbf{k},\mathbf{Q}}\delta_{\mathbf{k},-\mathbf{Q}}\left[\hat{\mathbf{Z}}+\imath\hat{\mathbf{Q}}\right]\left[\hat{\mathbf{Z}}+\imath\hat{\mathbf{Q}}\right]+\delta_{\mathbf{k},\mathbf{Q}}\delta_{\mathbf{k},\mathbf{Q}}\left[\hat{\mathbf{Z}}+\imath\hat{\mathbf{Q}}\right]\left[\hat{\mathbf{Z}}-\imath\hat{\mathbf{Q}}\right]\right)\end{aligned}$$

$$= \frac{M}{2} \left(\delta_{\mathbf{k},-\mathbf{Q}} + \delta_{\mathbf{k},\mathbf{Q}} \right) \tag{3.24}$$

Thus, a plot of the modulus of the Fourier transform should have peaks at $\mathbf{k} = \pm\mathbf{Q}$. When the cycloidal order transitions to homogeneous, there should be a single peak at $\mathbf{k} = \pm\mathbf{Q} = \mathbf{0}$. This is what is seen in Figures 3.4 and 3.5 which leads to the characterization of the system in Figure 3.4 as cycloidal and the system of Figure 3.5 as homogeneous.

As described above, two distinct symmetric, off-centre peaks qualitatively indicate cycloidal ordering and a lone central peak is qualitatively indicative of homogeneous ordering. There is the general issue of how to quanitatively distinguish between cycloidal and homogeneous ordering. Ideally, a transition to homogeneous ordering should be signified by $\langle \|\mathbf{Q}\| \rangle \to 0$. As can be seen in Figure 3.5, $\langle \|\mathbf{Q}\| \rangle \neq 0$, yet its peak is centred at zero. The disparity comes from the fact that the numerical simulations and their FFTs were performed on systems of finite size. The simulations were performed with $20 \times 20 \times 20$ systems. The reciprocal space values were separated by $\frac{2\pi}{20} = 0.31$.

The value of 0.31 would appear be a reasonable estimate for the threshold value since it would mean that the majority of the transform was within the smallest division away from zero. However in simulations, the value of $\langle \|\mathbf{Q}\| \rangle$ settled at 0.33 when fields were applied. Directly examining the lattice of spins, it was evident that a transition to homogeneous ordering had taken place. The choice was made to use $\langle \|\mathbf{Q}\| \rangle = 0.40$, somewhat above the 0.33, as the threshold value. Anything at or above this value was deemed to be cycloidal and anything below homogeneous.

Chapter 4

Results

Below are the results of the computer simulations using the algorithm described in Chapter 3 using the Hamiltonian from Chapter 2. They are compared with analytical results derived from the same Hamiltonian.

Simulations were run using two different configurations. One was with the polarization parallel the [001] direction. This is not a direction along which the polarization can point in BFO, but it was done to have the numerous cycloids in the $20 \times 20 \times 20$ cell all of the same length: $\hat{\mathbf{Q}} \perp \hat{\mathbf{Z}}$. Thus, the cycloid propagates along either $\hat{\mathbf{X}}$ or $\hat{\mathbf{Y}}$, which are now the major axes and are 20 spins long. In this configuration, $\frac{\boldsymbol{\delta}+\boldsymbol{\tau}}{a_{Rh}} = \pm\hat{\mathbf{X}};\ \pm\hat{\mathbf{Y}}; \text{or} \pm\hat{\mathbf{Z}}$.

The other configuration had the polarization along the conventional [111] direction. Here, $\frac{\boldsymbol{\delta}+\boldsymbol{\tau}}{a_{Rh}} = \pm\hat{\mathbf{x}};\ \pm\hat{\mathbf{y}}; \text{or} \pm\hat{\mathbf{z}}$. With the polarization along [111], the cycloid is along $\left[1\bar{1}0\right]$, $\left[10\bar{1}\right]$, or $\left[01\bar{1}\right]$. Throughout different parts of the supercell, there are different numbers of spins along these directions. The number of spins in the cycloids of the simulated supercell varies throughout the supercell.

The calculations presented in this chapter assume the polarization is along the [001] direction. Appendix A works out the calculations for $\mathbf{P} \parallel [111]$. Additional results that did not find room in this chapter are presented in Appendix B.

4.1 Initial Results

All of the simulations presented in this work were performed on a $20 \times 20 \times 20$ cube of spins. It is quite reasonable to wonder if the results are dependent of the size of the system. One approach would be to run simulations on arrays of varying sizes.

However, this would be quite time-consuming. Another approach, and what was done in this project, is to compare the energy per spin for the simulations to that of exact analytical results. If the $20 \times 20 \times 20$ system can approximate the same energy per spin as that of the analytical system, then there would be a basis to claim that the results have little dependence on system size.

Also, these initial tests help to show that the simulations were, in fact, approximating analytical solutions. Using simple systems with just the exchange and spin-current interactions present, the simulations were able to approximate the analytical solutions for both polarization orientations. This helps to prove the validity of the approach.

Consider the case where there is an applied magnetic field in the $\hat{\mathbf{X}}$ direction, but no applied electric field, with single-ion anisotropy set to zero:

$$\mathbf{B} = B\ \hat{\mathbf{X}}, A = E = 0.$$

The spins of the two sublattices are expected to have minimum energy for a conical cycloid as the spins form a cycloid, but are also all canted with a component aligned with the magnetic field:

$$\mathbf{S}_{1,i} = S\left(\sin\theta\,\hat{\mathbf{X}} + \cos\theta\left[\sin\left\{\mathbf{Q}\cdot\mathbf{R}_{1,i}\right\}\hat{\mathbf{Y}} + \cos\left\{\mathbf{Q}\cdot\mathbf{R}_{1,i}\right\}\hat{\mathbf{Z}}\right]\right), \tag{4.1}$$

$$\mathbf{S}_{2,i} = S\left(\sin\theta\,\hat{\mathbf{X}} - \cos\theta\left[\sin\left\{\mathbf{Q}\cdot\mathbf{R}_{2,i}\right\}\hat{\mathbf{Y}} + \cos\left\{\mathbf{Q}\cdot\mathbf{R}_{2,i}\right\}\hat{\mathbf{Z}}\right]\right). \tag{4.2}$$

The angle θ represents the angle between the spin vectors and the YZ-plane. If there is no magnetic field then $\theta = 0$ and the spins are entirely confined within the YZ-plane. Beyond some threshold magnetic field value to be determined, all spins point along the $\hat{\mathbf{X}}$ axis and thus $\theta = \dfrac{\pi}{2}$. This solution can be placed into the Hamiltonian and simplified:

$$\begin{aligned} H_{cc} &= \sum_i \sum_{\boldsymbol{\delta}} \left(J\mathbf{S}_{1,i}\cdot\mathbf{S}_{2,i+\boldsymbol{\delta}} + \left[D\left\{\hat{\mathbf{Z}}\times\frac{(\boldsymbol{\tau}+\boldsymbol{\delta})}{a_{Rh}}\right\} + D'\ \hat{\mathbf{Z}}\right]\cdot\left[\mathbf{S}_{1,i}\times\mathbf{S}_{2,i+\boldsymbol{\delta}}\right]\right) \\ &\quad - Sg\mu_B \sum_i \sum_{\eta=1,2} \left(\mathbf{S}_{\eta,i}\cdot\mathbf{B}\right) \\ &= \frac{NS^2}{2}\left(J\left[6\sin^2\theta - \cos^2\theta \sum_{\boldsymbol{\delta}} \cos\left\{\mathbf{Q}\cdot(\boldsymbol{\tau}+\boldsymbol{\delta})\right\}\right]\right. \end{aligned}$$

$$- \frac{D\cos^2\theta}{a_{Rh}}\hat{\mathbf{Y}}\cdot\sum_{\boldsymbol{\delta}}\left[\boldsymbol{\tau}+\boldsymbol{\delta}\right]\sin\left[\mathbf{Q}\cdot\left\{\boldsymbol{\tau}+\boldsymbol{\delta}\right\}\right]\Bigg) - NSg\mu_B B\sin\theta. \tag{4.3}$$

$\mathbf{Q} = Q\,\hat{\mathbf{Y}}$ minimizes the energy as it allows the Dzyaloshinksii-Moriya interaction to further reduce the energy.

$$\begin{aligned} H_{cc} &= \frac{NS^2}{2}\left(J\left[6\sin^2\theta - \cos^2\theta\left\{4+2\cos\left(Qa_{Rh}\right)\right\}\right] - 2D\cos^2\theta\sin\left[Qa_{Rh}\right]\right) \\ &\quad - NSg\mu_B B\sin\theta \\ &= NS^2\left(3J\sin^2\theta - \cos^2\theta\left[2J + J\cos\left\{Qa_{Rh}\right\} + D\sin\left\{Qa_{Rh}\right\}\right] - \frac{g\mu_B B\sin\theta}{S}\right). \end{aligned} \tag{4.4}$$

From here, Q can be optimized:

$$\frac{\partial H_{cc}}{\partial Q} = -NS^2\cos^2\theta a_{Rh}\left(D\cos\left[Qa_{Rh}\right] - J\sin\left[Qa_{Rh}\right]\right) = 0 \implies \tan\left(Qa_{Rh}\right) = \frac{D}{J}. \tag{4.5}$$

Equation (4.5) can be used to define $\sin\left(Qa_{Rh}\right)$ and $\cos\left(Qa_{Rh}\right)$:

$$\sin\left(Qa_{Rh}\right) = \frac{D}{\sqrt{D^2+J^2}}, \tag{4.6}$$

$$\cos\left(Qa_{Rh}\right) = \frac{J}{\sqrt{D^2+J^2}}. \tag{4.7}$$

These can then be replaced in the Hamiltonian,

$$\begin{aligned} H_{cc} &= NS^2\left(3J\sin^2\theta - \cos^2\theta\left[2J + \frac{J^2}{\sqrt{D^2+J^2}} + \frac{D^2}{\sqrt{D^2+J^2}}\right] - \frac{g\mu_B B\sin\theta}{S}\right) \\ &= NS^2\left(3J\sin^2\theta - \cos^2\theta\left[2J + \sqrt{D^2+J^2}\right] - \frac{g\mu_B B\sin\theta}{S}\right). \end{aligned} \tag{4.8}$$

The derivative of H_{cc} with respect to θ can then be taken to minimize the energy:

$$\begin{aligned} \frac{\partial H_{cc}}{\partial\theta} &= NS^2\cos\theta\left(\sin\theta\left[6J+4J+2\sqrt{D^2+J^2}\right] - \frac{g\mu_B B}{S}\right) = 0 \\ &\implies \sin\theta = \frac{g\mu_B B}{2S\left(5J+\sqrt{D^2+J^2}\right)}. \end{aligned} \tag{4.9}$$

This is then substituted into the energy term:

$$\begin{aligned} H_{cc} = NS^2 \Bigg(& 3J \left[\frac{g\mu_B B}{2S\left\{5J + \sqrt{D^2+J^2}\right\}} \right]^2 \\ & - \left[1 - \left\{ \frac{g\mu_B B}{2S\left(5J + \sqrt{D^2+J^2}\right)} \right\}^2 \right] \left[2J + \sqrt{D^2+J^2} \right] \\ & - \frac{\left[g\mu_B B\right]^2}{2S^2\left[5J + \sqrt{D^2+J^2}\right]} \Bigg) \end{aligned} \tag{4.10}$$

$$\begin{aligned} = NS^2 \Bigg(& - \left[2J + \sqrt{D^2+J^2} \right] \\ & + \left[5J + \sqrt{D^2+J^2} \right] \left[\frac{g\mu_B B}{2S\left\{5J + \sqrt{D^2+J^2}\right\}} \right]^2 - \frac{\left[g\mu_B B\right]^2}{2S^2\left[5J + \sqrt{D^2+J^2}\right]} \Bigg) \end{aligned}$$

$$= -NS^2 \left(2J + \sqrt{D^2+J^2} + \frac{\left[g\mu_B B\right]^2}{4S^2\left[5J + \sqrt{D^2+J^2}\right]} \right). \tag{4.11}$$

The energy per spin is

$$\frac{H_{cc}}{JNS^2} = -\left(2 + \sqrt{\left[\frac{D}{J}\right]^2 + 1} + \left[\frac{g\mu_B B}{2JS}\right]^2 \frac{1}{5 + \sqrt{\left[\frac{D}{J}\right]^2 + 1}} \right). \tag{4.12}$$

If there is no magnetic field then the energy per spin is

$$\frac{H_{cc}}{JNS^2} = -\left(2 + \sqrt{\left[\frac{D}{J}\right]^2 + 1} \right). \tag{4.13}$$

This is the energy that was compared with the numerical results for $\mathbf{P} \parallel [001]$. Two different approaches were taken with the simulations. In one the system had open boundary conditions: spins at the end of the cube only had local nearest neighbours. Spins on the other side of the cube were not considered to be neighbours. That is $\mathbf{S}_{\frac{N}{2}+1} \neq \mathbf{S}_{-\frac{N}{2}}$. There was concern that have periodic boundary conditions would affect the value of Q.

The second approach was with periodic boundary conditions where $\mathbf{S}_{\frac{N}{2}+1} = \mathbf{S}_{-\frac{N}{2}}$. As seen in Figure 4.1, this resulted in lower energies than the open boundary conditions. For special values of D where $\frac{D}{J} = \frac{2n\pi}{20}$, where $n \in \mathbb{N}$, the simulated

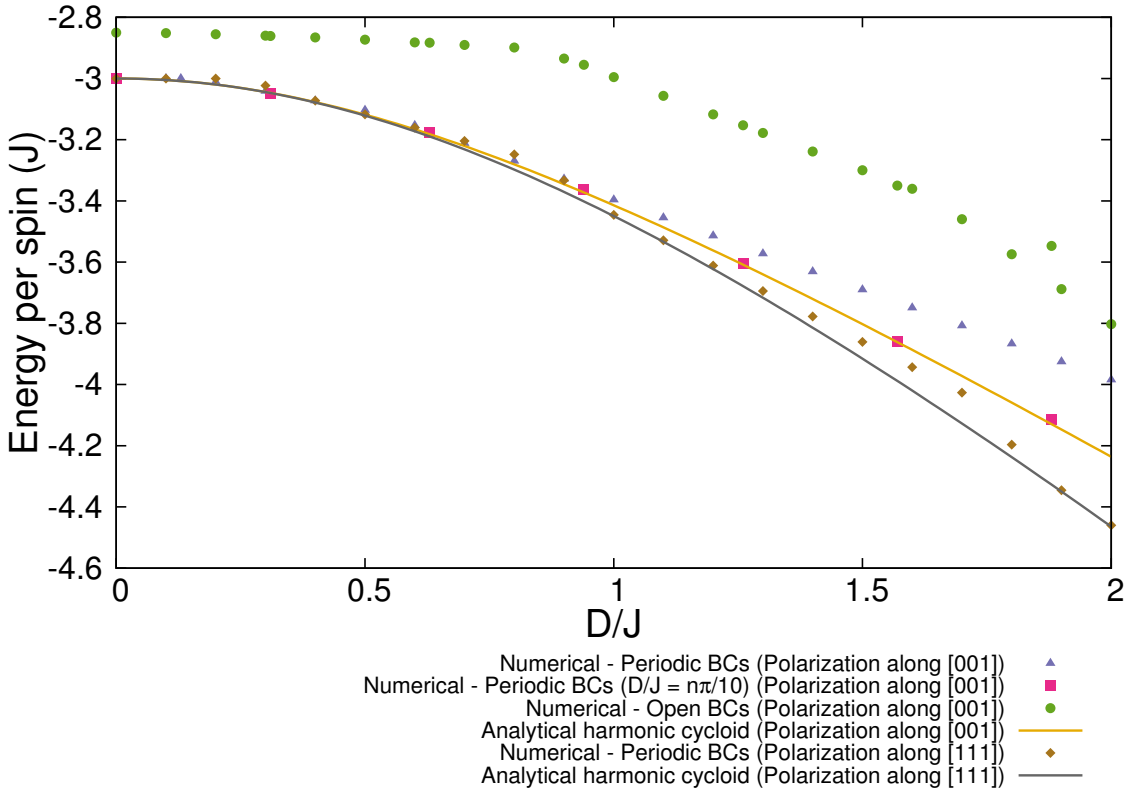

Figure 4.1: Energy per spin versus $\frac{D}{J}$ with no applied fields or anisotropy.

results agreed with the analytical ones which have periodic boundary conditions. For $Qa_{Rh} \ll 1$, $Qa_{Rh} = \frac{D}{J}$. The simulation takes $a_{Rh} = 1$. Therefore,

$$Q = \frac{D}{J} = \frac{2n\pi}{20} = \frac{2\pi}{\lambda} \implies \lambda = \frac{20}{n}. \tag{4.14}$$

Our numerical calculation agreed with the analytical solution (for the infinite system) only when the cycloid fits exactly inside our finite system. When the cycloid Q was not one of these special values, the simulations were of markedly higher energy than the analytical results, giving a measure of finite size effects. The disagreement between analytical and numerical results increased as $\frac{D}{J}$ increased. This could possibly be due to the increased size of the cycloid which, with the periodic boundary conditions, meant that the program had increasing difficulty in resolving the necessity of satisfying the boundary conditions while honouring the requirement of the size of the cycloid.

Using one of the special values of $\frac{D}{J}$ appeared to allow for the dismissal of concerns about the dependence of simulated results on system size. The results, using periodic boundary conditions, agreed with analytical ones for the polarization along [001]. As long as an integer number of periods of the cycloid (with no fields) were completed in the supercell, the numerical method was reliable in finding the ground state.

In regards to the polarization along [111], the simulated results appear to have some oscillatory nature not found when the polarization is along [001]. Because the length of the cycloids in the [111] configuration is not uniform, there are no special values of $\frac{D}{J}$ where there are an integer number of periods of the cycloid completed within the supercell. Thus, there are no values which reliably agree with the analytical results (see Equation (A.11)).

4.2 Competition Between Conical Cycloidal and Homogeneous Ordering

The goal of the project was to understand under which conditions, the spin state transitioned from cycloidal to homogeneous. When only a magnetic field is applied, if the state is cycloidal, then the conical cycloid can represent the solution as it has a component canted along the direction of the magnetic field whilst also having a cycloid. The energy from this state was evaluated in Section 4.1. Below, the homogeneous case is considered and then the two states are compared.

Consider the situation of $B = B\,\hat{\mathbf{X}}$ with no applied electric field or anisotropy:

$$\mathbf{B} = B\ \hat{\mathbf{X}}, A = E = 0.$$

For homogeneous ordering, there is the antiferromagnetic component and a component which point along the magnetic field direction:

$$\mathbf{S}_{1,i} = S\left(\sin\theta\,\hat{\mathbf{X}} + \cos\theta\hat{\mathbf{Z}}\right), \tag{4.15}$$

$$\mathbf{S}_{2,i} = S\left(\sin\theta\,\hat{\mathbf{X}} - \cos\theta\hat{\mathbf{Z}}\right). \tag{4.16}$$

These spins are then evaluated in the standard Hamiltonian of Chapter 2.

$$H_{homogeneous} = \sum_i \sum_{\boldsymbol{\delta}} \left(J\mathbf{S}_{1,i}\cdot\mathbf{S}_{2,i+\boldsymbol{\delta}} + \left[D\left\{\hat{\mathbf{Z}}\times\frac{(\boldsymbol{\tau}+\boldsymbol{\delta})}{a_{Rh}}\right\} + D'\ \hat{\mathbf{Z}}\right]\cdot\left[\mathbf{S}_{1,i}\times\mathbf{S}_{2,i+\boldsymbol{\delta}}\right]\right)$$

$$
\begin{aligned}
&- g\mu_B \sum_i \sum_{\eta=1,2} (\mathbf{S}_{\eta,i} \cdot \mathbf{B}) \\
&= \frac{NS^2}{2} \left(-6J \cos 2\theta + D \sin 2\theta \left[\hat{\mathbf{Y}} \times \hat{\mathbf{Z}} \right] \cdot \sum_{\boldsymbol{\delta}} [\boldsymbol{\tau} + \boldsymbol{\delta}] \right) - NSg\mu_B B \sin\theta \\
&= -NS \left(3JS \cos 2\theta + g\mu_B B \sin\theta \right). \qquad (4.17)
\end{aligned}
$$

The derivative of the energy with respect to θ is then taken to find the value of θ which minimizes the energy.

$$
\begin{aligned}
\frac{\partial H_{homogeneous}}{\partial \theta} &= -NS \left(-6JS \sin 2\theta + g\mu_B B \cos\theta \right) \\
&= -NS \cos\theta \left(-12JS \sin\theta + g\mu_B B \right) = 0 \implies \sin\theta = \frac{g\mu_B B}{12JS}. \qquad (4.18)
\end{aligned}
$$

Equation (4.18) is then substituted into Equation (4.17):

$$
\begin{aligned}
E_{homogeneous} &= -NS \left(3JS \left[1 - 2 \left\{ \frac{g\mu_B B}{12JS} \right\}^2 \right] + \frac{[g\mu_B B]^2}{12JS} \right) \\
&= -NJS^2 \left(3 + \frac{1}{24} \left[\frac{g\mu_B B}{JS} \right]^2 \right). \qquad (4.19)
\end{aligned}
$$

In Equation (4.12) the energy of a conical cycloid ground state was evaluated. Setting $D = 0$ in this expression produces the same result as Equation (4.19). Hence, with no Dzyaloshinskii-Moriya interaction, the cycloidal and the homogeneous cases produce the same energy as one would expect.

Evaluating the conical cycloid case with non-zero D, a comparison of the energy between the two states can be made to ascertain at what magnetic field value the homogeneous energy is lower than that of the conical cycloid:

$$
\begin{aligned}
&E_{cc} > E_{homogeneous} \\
-NS^2 \left(2J + \sqrt{D^2 + J^2} + \frac{[g\mu_B B]^2}{4S^2 \left[5J + \sqrt{D^2 + J^2} \right]} \right) &> -NJS^2 \left(3 + \frac{1}{24} \left[\frac{g\mu_B B}{JS} \right]^2 \right) \\
\left(\frac{g\mu_B B}{2S} \right)^2 \left(\frac{1}{5J + \sqrt{D^2 + J^2}} - \frac{1}{6J} \right) &< J - \sqrt{D^2 + J^2} \\
\left(\frac{g\mu_B B}{2S} \right)^2 \frac{6J - 5J - \sqrt{D^2 + J^2}}{6J \left(5J + \sqrt{D^2 + J^2} \right)} &< J - \sqrt{D^2 + J^2}
\end{aligned}
$$

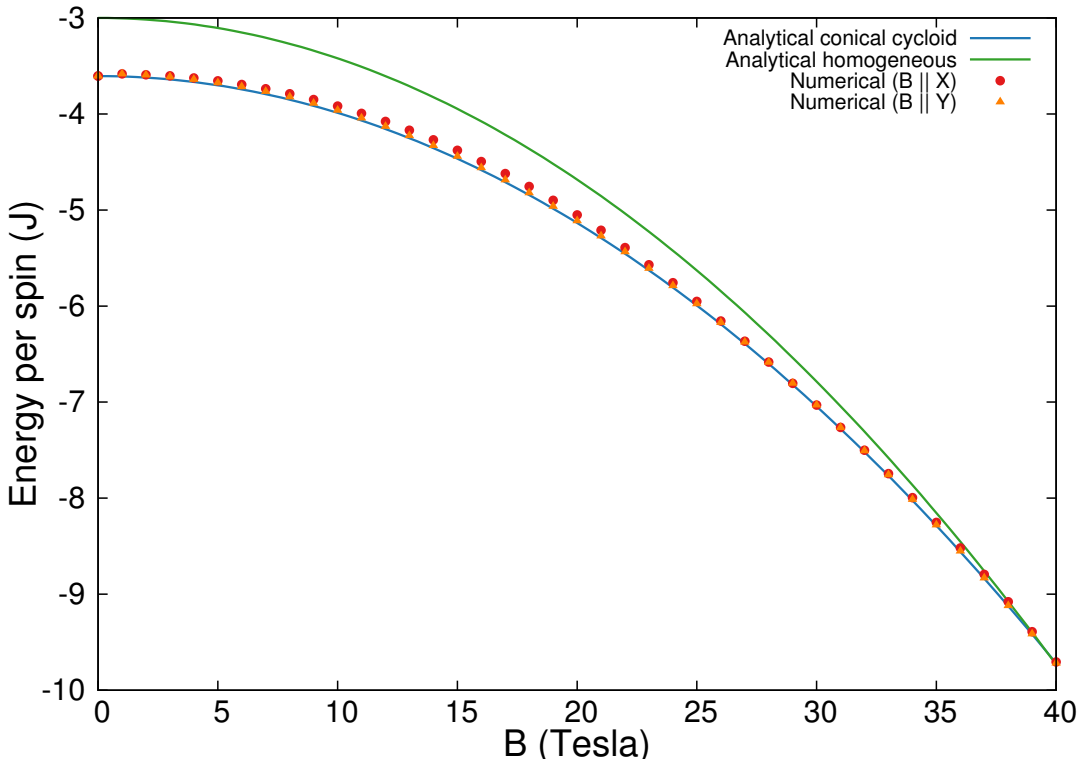

Figure 4.2: Simulation results of energy per spin versus magnetic field ($\mathbf{B} \parallel \hat{\mathbf{X}}$ and $\mathbf{B} \parallel \hat{\mathbf{Y}}$) compared with analytical conical cycloid and homogeneous cases for $\mathbf{P} \parallel [001]$. $\frac{D}{J} = \frac{2\pi}{5}$, $\frac{D'}{J} = 0.60$, $\frac{g\mu_B}{JS} = 0.317\ \mathrm{T}^{-1}$ and $A = E = 0$.

$$B^2 > 6J\left(5J + \sqrt{D^2 + J^2}\right)\left(\frac{2S}{g\mu_B}\right)^2$$

$$B^2 > 24\left(5 + \sqrt{\left[\frac{D}{J}\right]^2 + 1}\right)\left(\frac{JS}{g\mu_B}\right)^2$$

$$\left(B^2\right)_c = 24\left(5 + \sqrt{\left[\frac{D}{J}\right]^2 + 1}\right)\left(\frac{JS}{g\mu_B}\right)^2. \tag{4.20}$$

With $\frac{D}{J} = \frac{2\pi}{5}$ and $\frac{g\mu_B}{JS} = 0.318\,\mathrm{T}^{-1}$, as used in the simulations, the critical magnetic field is

$$\left(B^2\right)_c = 24\left(5 + \sqrt{\left[\frac{D}{J}\right]^2 + 1}\right)\left(\frac{JS}{g\mu_B}\right)^2$$

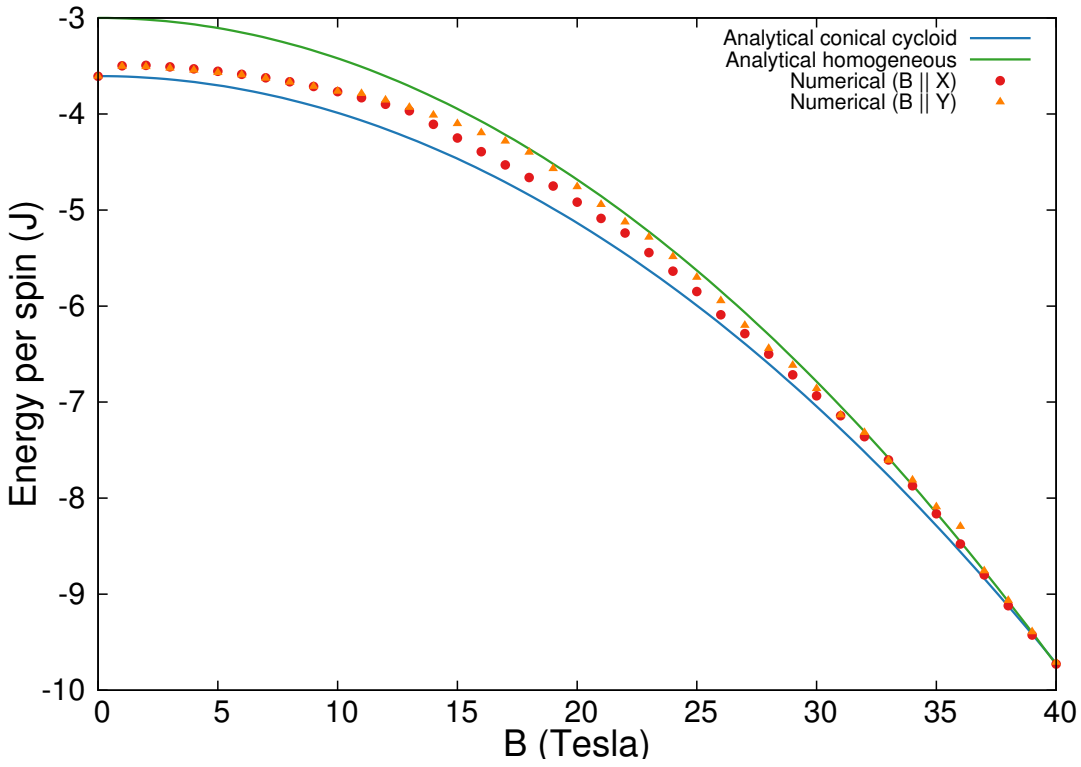

Figure 4.3: Simulation results of energy per spin versus magnetic field ($\mathbf{B} \parallel \hat{\mathbf{X}}$ and $\mathbf{B} \parallel \hat{\mathbf{Y}}$) compared with analytical conical cycloid and homogeneous cases for $\mathbf{P} \parallel [111]$. $\frac{D}{J} = \frac{2\pi}{5}$, $\frac{D'}{J} = 0.60$, $\frac{g\mu_B}{JS} = 0.317\ \mathrm{T}^{-1}$ and $A = E = 0$.

$$
\begin{aligned}
&= \frac{24\left(5 + \sqrt{\left[\frac{2\pi}{5}\right]^2 + 1}\right)}{\left(0.318\,\mathrm{T}^{-1}\right)^2} \\
&= 1.57 \times 10^3\,\mathrm{T}^2. \\
B_c &= 39.6\,\mathrm{T}.
\end{aligned}
$$

Up until approximately 40 T, the conical cycloid is the lower energy state compared to the homogeneous state with these values. Figure 4.2 shows the results of the simulations for $\mathbf{P} \parallel [001]$. The simulation results agreed with the analytical results. Through 38 T, the conical cycloidal state was of lower energy for $\mathbf{B} \parallel \hat{\mathbf{X}}$. For $\mathbf{B} \parallel \hat{\mathbf{Y}}$, which should have the same magnetic response as $\mathbf{B} \parallel \hat{\mathbf{X}}$, the conical cycloid was favoured through 40 T. It should also be noted that at such high field values, the homogeneous state is actually ferromagnetic, not antiferromagnetic. As to why there was a descrepancy between $\mathbf{B} \parallel \hat{\mathbf{X}}$ and $\mathbf{B} \parallel \hat{\mathbf{Y}}$, it may be a case that the energies of

the states were quite close and the program in one instance was able to distinguish the correct ground state and could not in the other.

In Figure 4.3 the simulated results for $\mathbf{P} \parallel [111]$ do not match the analytical one (Equation (A.10)) as well as the ones for $\mathbf{P} \parallel [001]$ in Figure 4.2. They are still mostly below the analytical energy for homogeneous ordering, suggesting that the state is some type of modified conical cycloid.

4.3 Electric Field-Induced Anisotropy

As noted in Section 2.6, an applied electric field in an appropriate direction and of sufficient strength will transform a cycloidal state into a homogeneous one. To see how this works, several examples have been worked out below. From Reference [9], for $E = E_\perp \left(\cos\psi\,\hat{\mathbf{X}} + \sin\psi\,\hat{\mathbf{Y}}\right)$,

$$H_E = \frac{\xi E_\perp}{2} \sum_i \sum_{\eta=1,2} \left(\cos\psi\, S^2_{x;\eta,i} + \cos\left[\psi - \frac{2\pi}{3}\right] S^2_{y;\eta,i} + \cos\left[\psi - \frac{4\pi}{3}\right] S^2_{z;\eta,i} \right). \tag{4.21}$$

In $\mathbf{S}_{m;\eta,i}$ the index $m = x, y, z$ refers to the Cartesian coordinates, not the rhombohedral. From here, examples can be evaluated for electric fields in certain directions. For $E = E_\perp \hat{\mathbf{X}}$, $\psi = 0$:

$$\begin{aligned} H_E &= \frac{\xi E_\perp}{2} \sum_i \sum_{\eta=1,2} \left(\cos[0]\, S^2_{x;\eta,i} + \cos\left[-\frac{2\pi}{3}\right] S^2_{y;\eta,i} + \cos\left[-\frac{4\pi}{3}\right] S^2_{z;\eta,i} \right) \\ &= \frac{\xi E_\perp}{2} \sum_i \sum_{\eta=1,2} \left(S^2_{x;\eta,i} - \frac{S^2_{y;\eta,i} + S^2_{z;\eta,i}}{2} \right). \end{aligned} \tag{4.22}$$

It is energetically unfavourable to have spins having an x-component when the electric field is applied in the $\hat{\mathbf{X}}$ direction. It is favourable to have spins having y- and z-components, but as illustrated in Reference [9], a cycloid in the y-z plane can both reduce the electric field anisotropy and the Dzyaloshinskii-Moriya interaction, so no transition to homogeneous ordering occurs.

For $E = -E_\perp \hat{\mathbf{X}}$, $\psi = \pi$:

$$H_E = \frac{\xi E_\perp}{2} \sum_i \sum_{\eta=1,2} \left(\cos[\pi]\, S^2_{x;\eta,i} + \cos\left[\frac{\pi}{3}\right] S^2_{y;\eta,i} + \cos\left[-\frac{\pi}{3}\right] S^2_{z;\eta,i} \right)$$

$$= \frac{\xi E_\perp}{2} \sum_i \sum_{\eta=1,2} \left(-S^2_{x;\eta,i} + \frac{S^2_{y;\eta,i} + S^2_{z;\eta,i}}{2} \right). \tag{4.23}$$

Spins will form in a homogeneous antiferromagnetic configuration with spins parallel to $\hat{\mathbf{x}}$ when $\mathbf{E}_\perp = -E_\perp \hat{\mathbf{X}}$. This is the electric field direction that all simulations used.

For $E = E_\perp \hat{\mathbf{Y}}$, $\psi = \frac{\pi}{2}$:

$$\begin{aligned} H_E &= \frac{\xi E_\perp}{2} \sum_i \sum_{\eta=1,2} \left(\cos\left[\frac{\pi}{2}\right] S^2_{x;\eta,i} + \cos\left[-\frac{\pi}{6}\right] S^2_{y;\eta,i} + \cos\left[-\frac{5\pi}{6}\right] S^2_{z;\eta,i} \right) \\ &= \frac{\sqrt{3}\xi E_\perp}{4} \sum_i \sum_{\eta=1,2} \left(S^2_{y;\eta,i} - S^2_{z;\eta,i} \right). \end{aligned} \tag{4.24}$$

The anisotropy here, compels the system into a homogeneous antiferromagnet with spins pointing along the $\hat{\mathbf{z}}$ direction for a sufficient field strength.

For $E = -E_\perp \hat{\mathbf{Y}}$, $\psi = \frac{3\pi}{2}$:

$$\begin{aligned} H_E &= \frac{\xi E_\perp}{2} \sum_i \sum_{\eta=1,2} \left(\cos\left[\frac{3\pi}{2}\right] S^2_{x;\eta,i} + \cos\left[\frac{7\pi}{6}\right] S^2_{y;\eta,i} + \cos\left[\frac{5\pi}{6}\right] S^2_{z;\eta,i} \right) \\ &= \frac{\sqrt{3}\xi E_\perp}{4} \sum_i \sum_{\eta=1,2} \left(S^2_{z;\eta,i} - S^2_{y;\eta,i} \right). \end{aligned} \tag{4.25}$$

The spins want to align along the $\hat{\mathbf{y}}$ direction to form a homogeneous antiferromagnet for adequate electric field strength. Figure 4.4 displays the entire electric field phase diagram calculated using continuum field theory [9].

As with the magnetic field, the cycloidal and homogeneous cases can be analyzed and the critical electric field can be determined. Consider the case with no magnetic field and no single-ion anisotropy. The homogeneous state will be assessed first:

$$A = B = 0, \mathbf{E}_\perp = -E_\perp \hat{\mathbf{X}}$$

$$\mathbf{S}_{1,i} = S \left(-\frac{2}{\sqrt{6}} \hat{\mathbf{X}} + \frac{1}{\sqrt{3}} \hat{\mathbf{Z}} \right) \tag{4.26}$$

$$\mathbf{S}_{2,i} = S \left(\frac{2}{\sqrt{6}} \hat{\mathbf{X}} - \frac{1}{\sqrt{3}} \hat{\mathbf{Z}} \right). \tag{4.27}$$

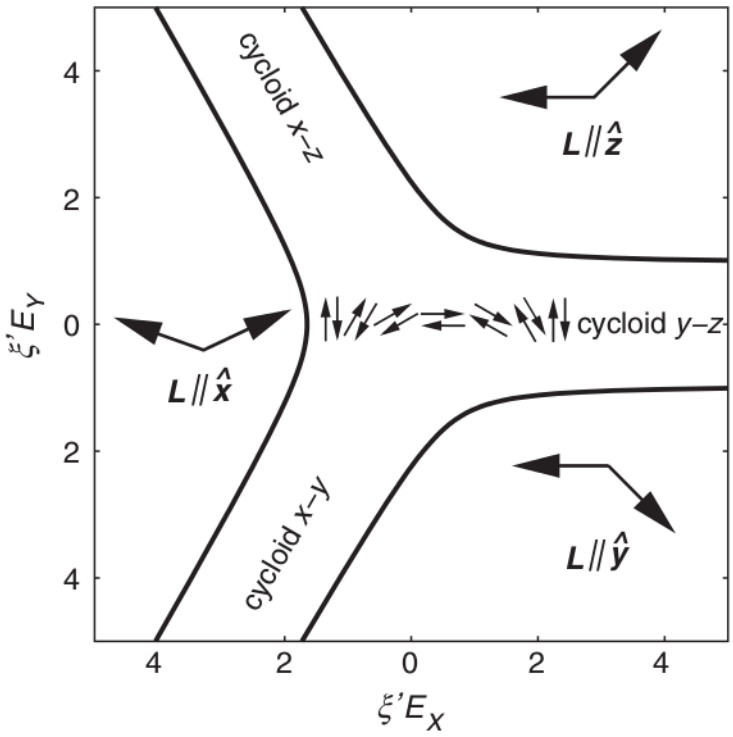

Figure 4.4: Electric field phase diagram. From Reference [9].

The spins can then be placed into the Hamiltonian:

$$\begin{aligned} H_{homogeneous} =& \sum_i \sum_{\boldsymbol{\delta}} \left(J\mathbf{S}_{1,i} \cdot \mathbf{S}_{2,i+\boldsymbol{\delta}} + \left[D \left\{ \hat{\mathbf{Z}} \times \frac{(\boldsymbol{\tau} + \boldsymbol{\delta})}{a_{Rh}} \right\} + D' \, \hat{\mathbf{Z}} \right] \cdot \left[\mathbf{S}_{1,i} \times \mathbf{S}_{2,i+\boldsymbol{\delta}} \right] \right) \\ & - \frac{\xi}{4} \sum_i \sum_{\eta=1,2} \left(\mathbf{E}_\perp \cdot \left[\left\{ \left(S^Y_{\eta,i} \right)^2 - \left(S^X_{\eta,i} \right)^2 \right\} \hat{\mathbf{X}} + 2 S^X_{\eta,i} S^Y_{\eta,i} \hat{\mathbf{Y}} \right] \right. \\ & \left. + 2\sqrt{2} \mathbf{E}_\perp \cdot \left[S^X_{\eta,i} \hat{\mathbf{X}} + S^Y_{\eta,i} \hat{\mathbf{Y}} \right] S^Z_{\eta,i} \right) \\ =& -3JNS^2 - \frac{\xi E_\perp S^2}{4} \sum_i \sum_{\eta=1,2} \frac{2+4}{3} \\ =& -NS^2 \left(3J + \frac{\xi E_\perp}{2} \right). \end{aligned} \tag{4.28}$$

Moving on to the cycloidal case, the spin states are

$$\mathbf{S}_{1,i} = S \left(\sin \left[\mathbf{Q} \cdot \mathbf{R}_{1,i} \right] \hat{\mathbf{X}} + \cos \left[\mathbf{Q} \cdot \mathbf{R}_{1,i} \right] \hat{\mathbf{Z}} \right), \tag{4.29}$$

$$\mathbf{S}_{2,i} = -S \left(\sin \left[\mathbf{Q} \cdot \mathbf{R}_{2,i} \right] \hat{\mathbf{X}} + \cos \left[\mathbf{Q} \cdot \mathbf{R}_{2,i} \right] \hat{\mathbf{Z}} \right). \tag{4.30}$$

This can then be once again placed into the Hamiltonian,

$$\begin{aligned}
H_{cycloid} =& \sum_i \sum_{\boldsymbol{\delta}} \left(J\mathbf{S}_{1,i} \cdot \mathbf{S}_{2,i+\boldsymbol{\delta}} + \left[D \left\{ \hat{\mathbf{Z}} \times \frac{(\boldsymbol{\tau}+\boldsymbol{\delta})}{a_{Rh}} \right\} + D' \, \hat{\mathbf{Z}} \right] \cdot [\mathbf{S}_{1,i} \times \mathbf{S}_{2,i+\boldsymbol{\delta}}] \right) \\
& - \frac{\xi}{4} \sum_i \sum_{\eta=1,2} \left(\mathbf{E}_\perp \cdot \left[\left\{ \left(S^Y_{\eta,i}\right)^2 - \left(S^X_{\eta,i}\right)^2 \right\} \hat{\mathbf{X}} + 2 S^X_{\eta,i} S^Y_{\eta,i} \hat{\mathbf{Y}} \right] \right. \\
& \left. + 2\sqrt{2} \mathbf{E}_\perp \cdot \left[S^X_{\eta,i} \hat{\mathbf{X}} + S^Y_{\eta,i} \hat{\mathbf{Y}} \right] S^Z_{\eta,i} \right) \\
=& \frac{NS^2}{2} \left(-J \sum_{\boldsymbol{\delta}} \cos\left[\mathbf{Q} \cdot \{\boldsymbol{\tau}+\boldsymbol{\delta}\}\right] \right. \\
& \left. + \frac{D}{a_{Rh}} \left[\hat{\mathbf{Y}} \times \hat{\mathbf{Z}} \right] \cdot \sum_{\boldsymbol{\delta}} [\boldsymbol{\tau}+\boldsymbol{\delta}] \sin\left[\mathbf{Q} \cdot \{\boldsymbol{\tau}+\boldsymbol{\delta}\}\right] - \frac{\xi E_\perp}{4} \right) \\
=& \frac{NS^2}{2} \left(-J \sum_{\boldsymbol{\delta}} \cos\left[\mathbf{Q} \cdot \{\boldsymbol{\tau}+\boldsymbol{\delta}\}\right] + \frac{D}{a_{Rh}} \hat{\mathbf{X}} \cdot \sum_{\boldsymbol{\delta}} [\boldsymbol{\tau}+\boldsymbol{\delta}] \sin\left[\mathbf{Q} \cdot \{\boldsymbol{\tau}+\boldsymbol{\delta}\}\right] \right. \\
& \left. - \frac{\xi E_\perp}{4} \right) \\
=& -NS^2 \left(J \left[2 + \cos\left\{ Q a_{Rh} \right\} \right] + D \sin\left[Q a_{Rh} \right] + \frac{\xi E_\perp}{8} \right). \qquad (4.31)
\end{aligned}$$

$\mathbf{Q} = -Q\,\hat{\mathbf{X}}$ gives the lowest energy. The derivative with respect to Q can be taken of the Hamiltonian to find the value of Q which minimizes the energy.

$$\frac{\partial H_{cycloid}}{\partial Q} = -NS^2 a_{Rh} \left(-J \sin\left[Q a_{Rh} \right] + D \cos\left[Q a_{Rh} \right] \right) = 0 \implies \tan\left(Q a_{Rh} \right) = \frac{D}{J}. \qquad (4.32)$$

This leads to

$$\sin\left(Q a_{Rh} \right) = \frac{D}{\sqrt{D^2 + J^2}}, \qquad (4.33)$$

$$\cos\left(Q a_{Rh} \right) = \frac{J}{\sqrt{D^2 + J^2}}. \qquad (4.34)$$

These expressions can be inserted into the Hamiltonian:

$$\begin{aligned}
E_{cycloid} =& -NS^2 \left(J \left[2 + \frac{J}{\sqrt{D^2+J^2}} \right] + \frac{D^2}{\sqrt{D^2+J^2}} + \frac{\xi E_\perp}{8} \right) \\
=& -NS^2 \left(2J + \sqrt{D^2+J^2} + \frac{\xi E_\perp}{8} \right). \qquad (4.35)
\end{aligned}$$

Now, the energies of the cycloidal and homogeneous states can be analyzed to see at what value of electric field it is preferable for the spins to align homogeneously:

$$
\begin{aligned}
E_{cycloid} &> E_{homogeneous} \\
-NS^2\left(2J+\sqrt{D^2+J^2}+\frac{\xi E_\perp}{8}\right) &> -NS^2\left(3J+\frac{\xi E_\perp}{2}\right) \\
\frac{3\xi E_\perp}{8} &> \sqrt{D^2+J^2}-J \\
E_\perp &> \frac{8\left(\sqrt{D^2+J^2}-J\right)}{3\xi} \\
E_\perp &> \frac{8\left(\sqrt{\left[\frac{D}{J}\right]^2+1}-1\right)}{\frac{3\xi}{J}} \\
(E_\perp)_c &= \frac{8\left(\sqrt{\left[\frac{D}{J}\right]^2+1}-1\right)}{\frac{3\xi}{J}}.
\end{aligned}
\tag{4.36}
$$

With $\frac{D}{J}=\frac{2\pi}{5}$ and $\frac{\xi}{J}=5.77\times10^{-5}\,\mathrm{cm\,V^{-1}}$,

$$
\begin{aligned}
(E_\perp)_c =& \frac{8\left(\sqrt{\left[\frac{2\pi}{5}\right]^2+1}-1\right)}{3\left(5.77\times10^{-5}\,\mathrm{cm\,V^{-1}}\right)} \\
=& 2.78\times10^4\,\mathrm{V\,cm^{-1}}.
\end{aligned}
$$

This value for the critical field is consistent with what was found during simulations as can be seen in Figure 4.5. The transition occurs between 2.5 and $3.0\times10^4\,\mathrm{V\,cm^{-1}}$ when $\langle\|\mathbf{Q}\|\rangle$ falls below 0.4. Figure 4.6 shows the transition for the polarization along [111]. Here, the transition occurs between 3.5 and $4.0\times10^4\,\mathrm{V\,cm^{-1}}$, although the calculations carried out in Appendix A suggest that the transition should happen at lower fields. Part of the discrepancy may be due to the varying cycloid length throughout the supercell.

It should be noted that the analytical calculation of $E_{cycloid}$ presented here is the simplest possibe approximation. In reality, the cycloid ground state will become anharmonic as a function of the electric field and the Q of the cycloid will depend on the electric field. This effect gives a higher critical field, as shown in the numerical

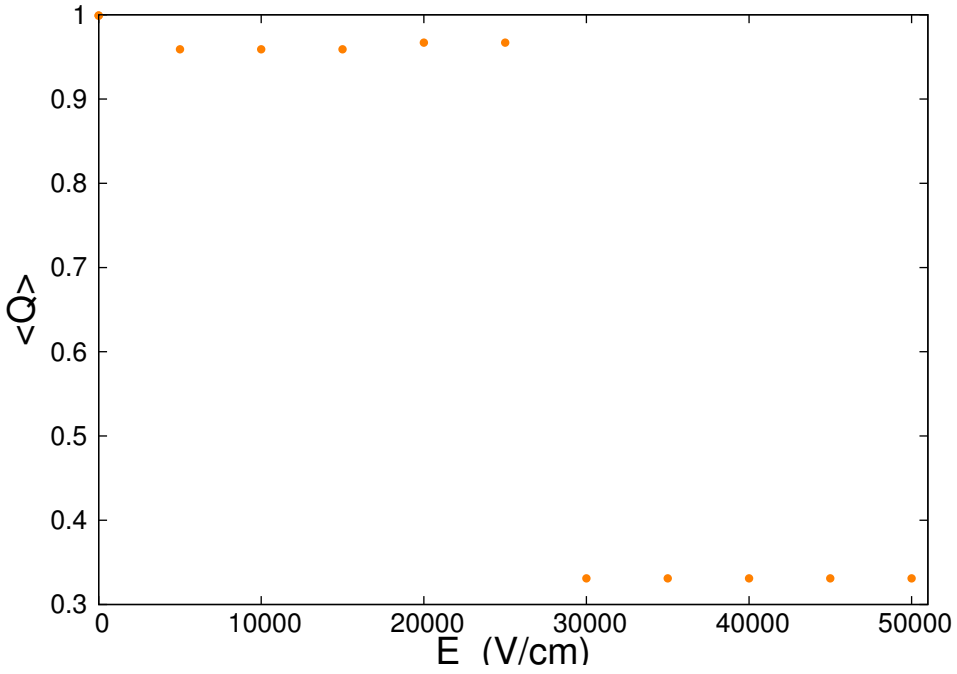

Figure 4.5: $\langle \|\mathbf{Q}\| \rangle$ versus $\mathbf{E} \parallel -\hat{\mathbf{X}}$. $A = 0$, $\frac{D}{J} = \frac{2\pi}{5}$, $\frac{D'}{J} = 0.60$, $\frac{\xi}{J} = 5.77 \times 10^{-5}$ V cm^{-1} and no magnetic field with $\mathbf{P} \parallel [001]$.

simulations.

4.4 Magnetic Field-Induced Homogeneity

It was seen in Section 4.2 that the application of a magnetic field along $\mathbf{B} \parallel \hat{\mathbf{X}}$ or $\mathbf{B} \parallel \hat{\mathbf{Y}}$ in the absence of an electric field did not force the system into a homogeneous configuration until the magnetic field strength was near 40 T.

The magnetization per spin and its modulus were measured in the simulations. They were defined as,

$$\langle \mathbf{M} \rangle = \frac{1}{N} \sum_{i} \sum_{\eta=1,2} \mathbf{S}_{\eta,i}, \tag{4.37}$$

$$\| \langle \mathbf{M} \rangle \| = \sqrt{\mathbf{M}^2}. \tag{4.38}$$

The magnetization was evaluated with spins of unit value ($S = 1$). The modulus, thus had a range of zero to one. As the magnetic field increased, the magnetization increased, as expected. The progress of the magnetization as the field strength in-

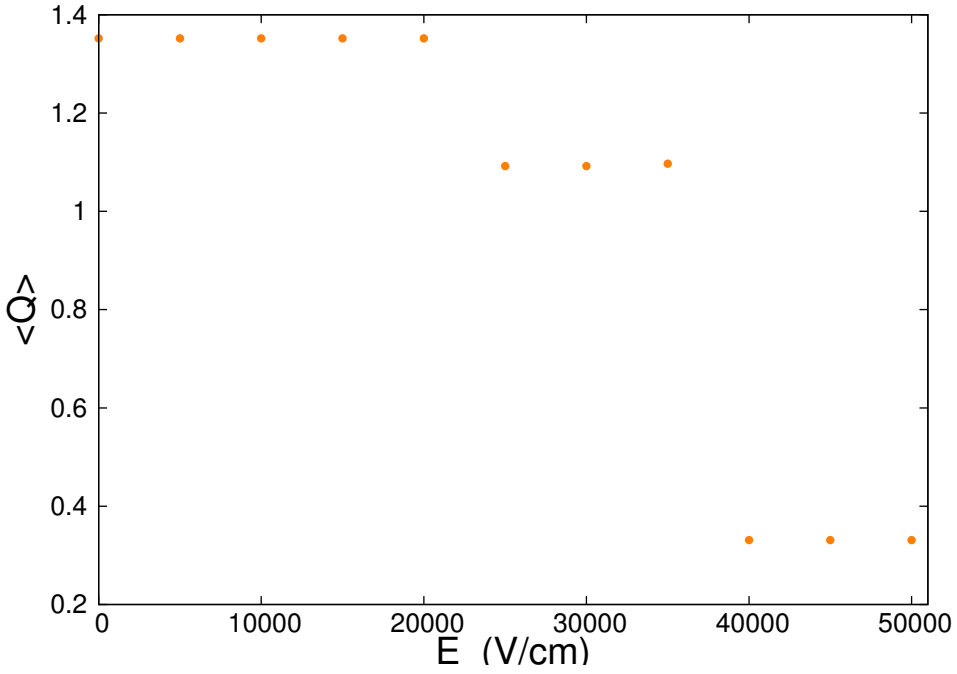

Figure 4.6: $\langle \|\mathbf{Q}\| \rangle$ versus $\mathbf{E} \parallel -\hat{\mathbf{X}}$. $A = 0$, $\frac{D}{J} = \frac{2\pi}{5}$, $\frac{D'}{J} = 0.60$, $\frac{\xi}{J} = 5.77 \times 10^{-5}$ V cm^{-1} and no magnetic field with $\mathbf{P} \parallel [111]$.

creased also served, along with $\langle \|\mathbf{Q}\| \rangle$, as a proxy to determine the transition from cycloidal to homogeneous ordering. At the transition the magnetization (and $\langle \|\mathbf{Q}\| \rangle$) had a sudden increase (decrease) in value. This is seen in Figures 4.11 where as B^Z is increased the magnetization has a linear-like increase and $\langle \|\mathbf{Q}\| \rangle$ for most points is constant. However, at $B^Z = 15$ T there is a jump in the magnetization and $\langle \|\mathbf{Q}\| \rangle$ falls below 0.4, the threshold value for transitions from cycloidal to homogeneous ordering. This is with the polarization along [001]. With the polarization along [111], Figure 4.12, a similar picture emerges, although the transition occurs at $B^Z = 12$ T.

The phase transition from cycloidal to homogeneous ordering appears here to be discontinuous and thus, first order. However, the finite system size and the gap between data makes it difficult to say for certain. Perhaps $\langle \|\mathbf{Q}\| \rangle$ is continuous through the transition and the small system size is merely incapable of capturing that. Also, we have no theory for how the cycloid is arranged when the magnetic field is parallel to the polarization and thus cannot say whether the cycloid form permits $\langle \|\mathbf{Q}\| \rangle$ to take continuously decreasing values as $\langle \|\mathbf{Q}\| \rangle \to 0$.

The Zeeman energy details how the application of a magnetic field affects the spin configuration. It allows one to see what the favoured direction of alignment for the

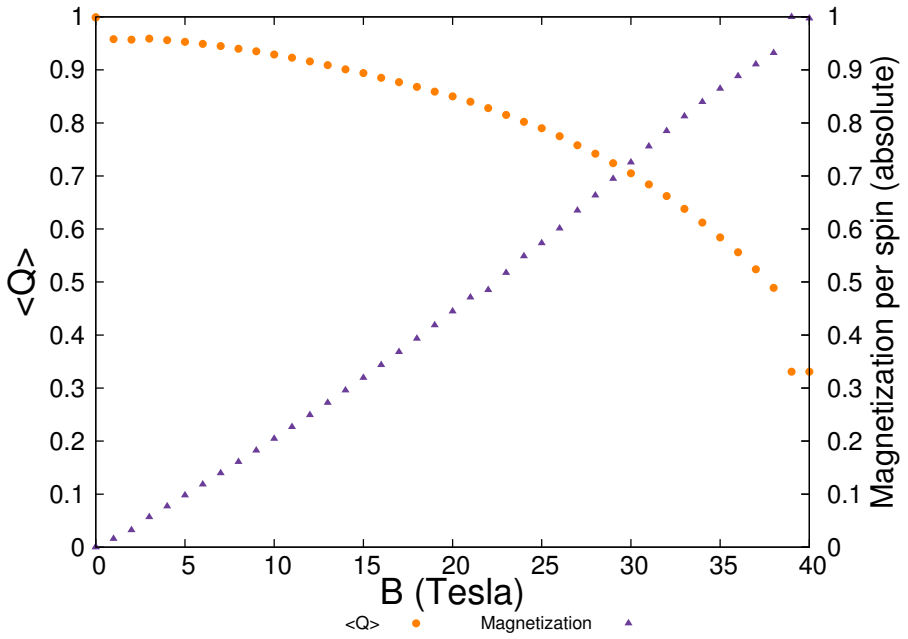

Figure 4.7: $\langle \|\mathbf{Q}\| \rangle$ and magnetization modulus versus B^X. $A = 0$, $\frac{D}{J} = \frac{2\pi}{5}$, $\frac{D'}{J} = 0.60$, $\frac{g\mu_B}{JS} = 0.318$ T^{-1} and no electric field ($\mathbf{P} \parallel [001]$).

spins is. For $\mathbf{B} \parallel \hat{\mathbf{X}}$,

$$\begin{aligned} H_Z &= -\, g\mu_B \sum_i \sum_{\eta=1,2} \mathbf{S}_{\eta,i} \cdot \mathbf{B} \\ &= -\, g\mu_B B \sum_i \sum_{\eta=1,2} S^X_{\eta,i}. \end{aligned} \tag{4.39}$$

Obviously, $\mathbf{B} \parallel \hat{\mathbf{X}}$, favors the canting of $\mathbf{S} \parallel \hat{\mathbf{X}}$, so that the S^Y and S^Z components can form a cycloid. Such a canted cycloid state is quite stable up to $B \approx 40$ T.

Figures 4.9 and 4.10 show similar results for $\mathbf{B} \parallel \hat{\mathbf{Y}}$ as Figures 4.7 and 4.8 show for $\mathbf{B} \parallel \hat{\mathbf{X}}$. In practise, this means that such a transition would be very hard to observe in the laboratory.

With $\mathbf{B} \parallel \hat{\mathbf{Z}}$ the Zeeman interaction wants spins pointing along the positive $\hat{\mathbf{Z}}$ direction. This is incompatible with the cycloid as the cycloid must have a component along $\hat{\mathbf{Z}}$. For the simulations (Figures 4.11 and 4.12), the system was able to transition at approximately 15 T when $\mathbf{P} \parallel [001]$ and 12 T when $\mathbf{P} \parallel [111]$.

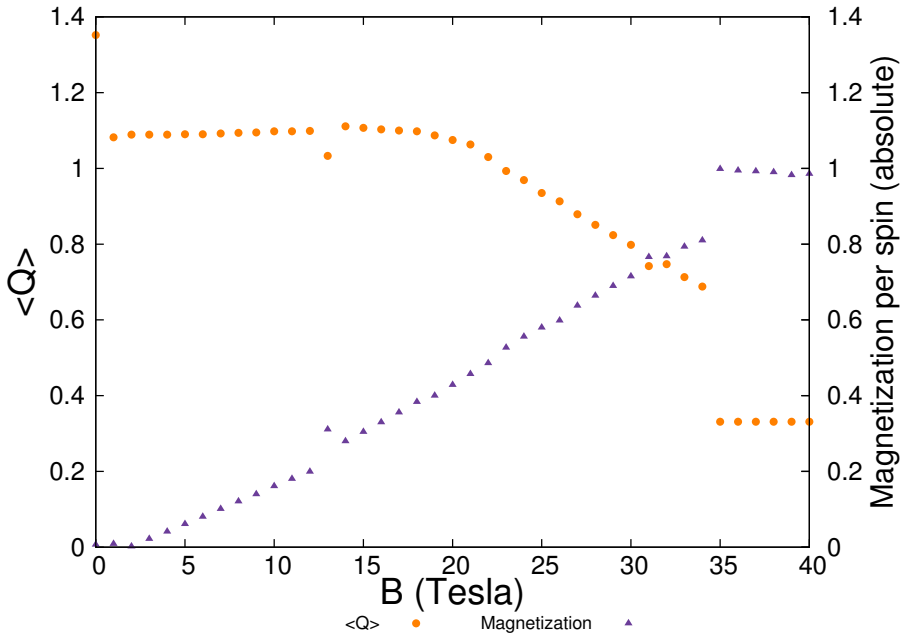

Figure 4.8: $\langle \|\mathbf{Q}\| \rangle$ and magnetization modulus versus B^X. $A = 0$, $\frac{D}{J} = \frac{2\pi}{5}$, $\frac{D'}{J} = 0.60$, $\frac{g\mu_B}{JS} = 0.318\ \mathrm{T}^{-1}$ and no electric field ($\mathbf{P} \parallel [111]$).

4.5 Electric Field-Magnetic Field Phase Diagrams

Presented here are the electric field-magnetic field phase diagrams for $\mathbf{E} \parallel -\hat{\mathbf{X}}$ and $\mathbf{B}$ along one of the rhombohedral directions which indicate whether for the given applied fields, the simulated BFO sample had cycloidal or homogeneous spin ordering. The parameters for all of the simulations were $A = 0, \frac{D}{J} = \frac{2\pi}{5}, \frac{D'}{J} = 0.60$ and $\frac{\xi}{J} = 5.77 \times 10^{-5}\,\mathrm{cm\,V^{-1}}$.

It was earlier stated that for $B = 0$, the field strength required to have the BFO sample be homogeneous for $\mathbf{E} \parallel -\hat{\mathbf{X}}$ was $E_\perp = (2.5\text{–}3.0) \times 10^4\,\mathrm{V\,cm^{-1}}$ when $\mathbf{P} \parallel [001]$. For $E_\perp = 0$, the magnetic field needed to induce homogeneous ordering for $\mathbf{B} \parallel \hat{\mathbf{X}}$ or $\mathbf{B} \parallel \hat{\mathbf{Y}}$ was $B \approx 40$ T. For $\mathbf{B} \parallel \hat{\mathbf{Z}}$, the transition was much lower in the range of 15 T.

When $\mathbf{P} \parallel [111]$, the magnetic field need to transform the supercell to homogeneous ordering, with no electric field applied, was 12 T. With no magnetic field, the electric field needed to transform the system to homogeneous ordering was $E^X = -4.0 \times 10^4\ \mathrm{V\ cm^{-1}}$.

When electric and magnetic fields were simultaneously applied to the system, there was interplay which in some instances inhibited the transition to homogeneous

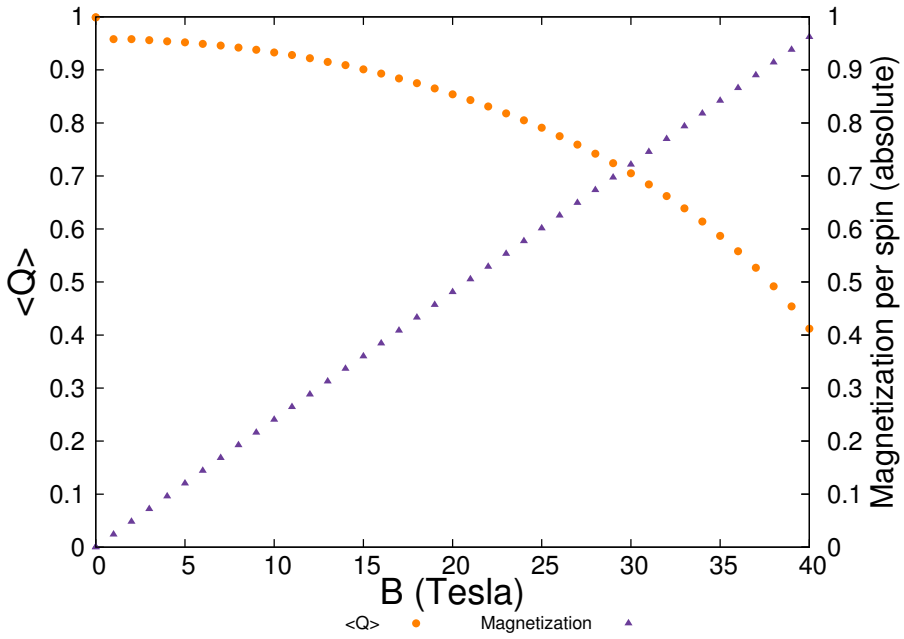

Figure 4.9: $\langle \|\mathbf{Q}\| \rangle$ and magnetization modulus versus B^Y. $A = 0$, $\frac{D}{J} = \frac{2\pi}{5}$, $\frac{D'}{J} = 0.60$, $\frac{g\mu_B}{JS} = 0.318\ \mathrm{T}^{-1}$ and no electric field ($\mathbf{P} \parallel [001]$).

ordering and in others facilitated it.

For the $E^X - B^X$ phase diagram with $\mathbf{P} \parallel [001]$, applying a magnetic field inhibited the transition to homogeneous ordering. In Figure 4.13 at strong electric and weak magnetic field (upper left of diagram) values the system is homogeneous. Along a constant electric field, as the magnetic field strength is increased the system returns to cycloidal. With increasing electric field, larger magnetic field strengths are needed to compel the system to return to cycloidal ordering, but for all field strengths explored, it did eventually return. With $\mathbf{P} \parallel [111]$, Figure 4.14, the magnetic field competes against homogeneous ordering as well.

With the $E^X - B^Y$ phase diagram with the polarization along [001], the homogeneous ordering appears to be mainly independent of the magnetic field (see Figure 4.15). At $E^X_\perp = -3.0 \times 10^4\,\mathrm{V\,cm^{-1}}$ there is altering between homogeneous and cycloidal ordering, but these may have been difficult cases for the computer programs with the homogeneous and cycloidal energies being rather close. At stronger electric fields, the system is always homogeneous. When the polarization is changed to along [111], the fields no longer seem independent of each other. The magnetic field alternates between supporting and suppressing the homogeneous ordering. For certain

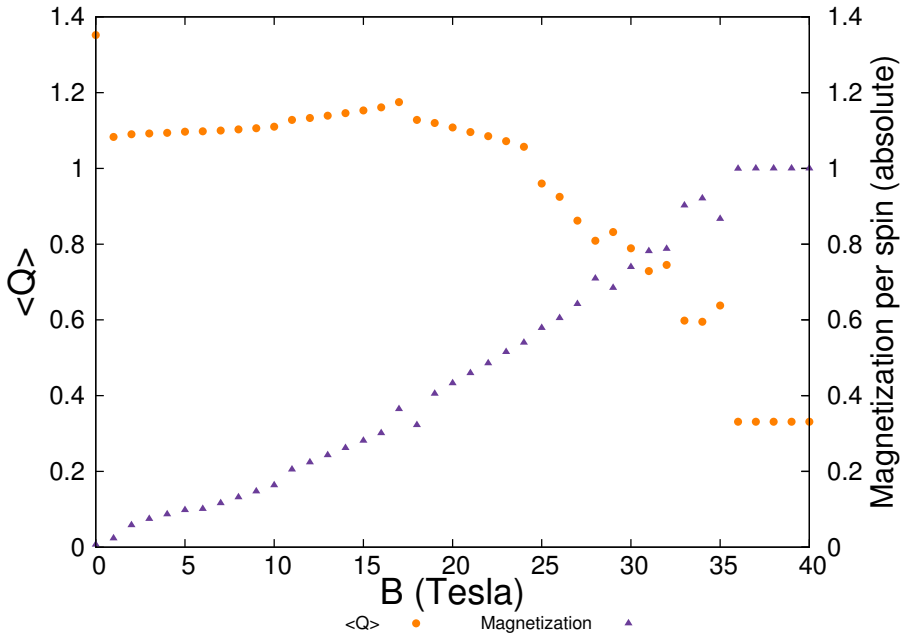

Figure 4.10: $\langle \|\mathbf{Q}\| \rangle$ and magnetization modulus versus B^Y. $A = 0$, $\frac{D}{J} = \frac{2\pi}{5}$, $\frac{D'}{J} = 0.60$, $\frac{g\mu_B}{JS} = 0.318\ \mathrm{T}^{-1}$ and no electric field ($\mathbf{P} \parallel [111]$).

field combinations, the magnetic field aids the transition to homogeneous ordering only to work against it as the strength of the field is increased.

In some regards, $E^X - B^Z$ phase diagram for $\mathbf{P} \parallel [001]$ is the opposite case to the $E^X - B^X$ phase diagram with $\mathbf{P} \parallel [001]$. Looking at Figure 4.17, the application of a magnetic field helped to facilitate the transition to homogeneous ordering. At $E^X_\perp = 0$, it required a $B^Z = 15$ T field for the system to transition from cycloidal to homogeneous. At $E^X_\perp = -1.0 \times 10^4\,\mathrm{V\,cm^{-1}}$, a 13 T field was able to perform the task. As the electric field strength increased, the magnetic field needed to induce a transition decreased. With the polarization along [111], Figure 4.18, the transition to homogeneous ordering is also aided by the combination of electric and magnetic fields. With just a magnetic field applied, the transition occurs at 12 T. Used alone, a stronger electric field is necessary for the system to be homogeneous than when $\mathbf{P} \parallel [001]$ ($E^X = -4.0 \times 10^4$ V cm^{-1}). This results in the homogeneous region of the [111] phase diagram being taller and narrower than that of the [001] diagram.

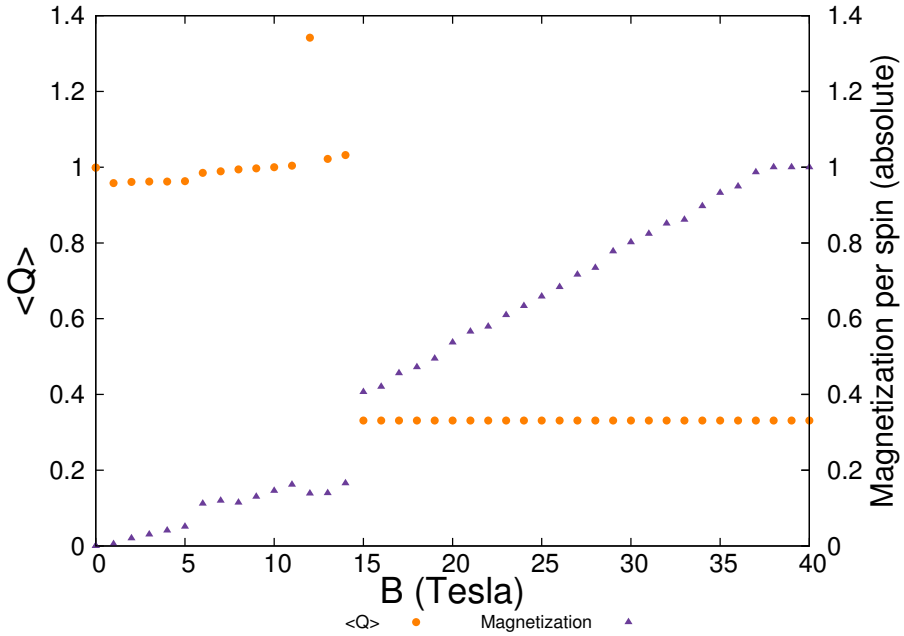

Figure 4.11: $\langle \|\mathbf{Q}\| \rangle$ and magnetization modulus versus B^Z. $A = 0$, $\frac{D}{J} = \frac{2\pi}{5}$, $\frac{D'}{J} = 0.60$, $\frac{g\mu_B}{JS} = 0.318$ T^{-1} and no electric field ($\mathbf{P} \parallel [001]$).

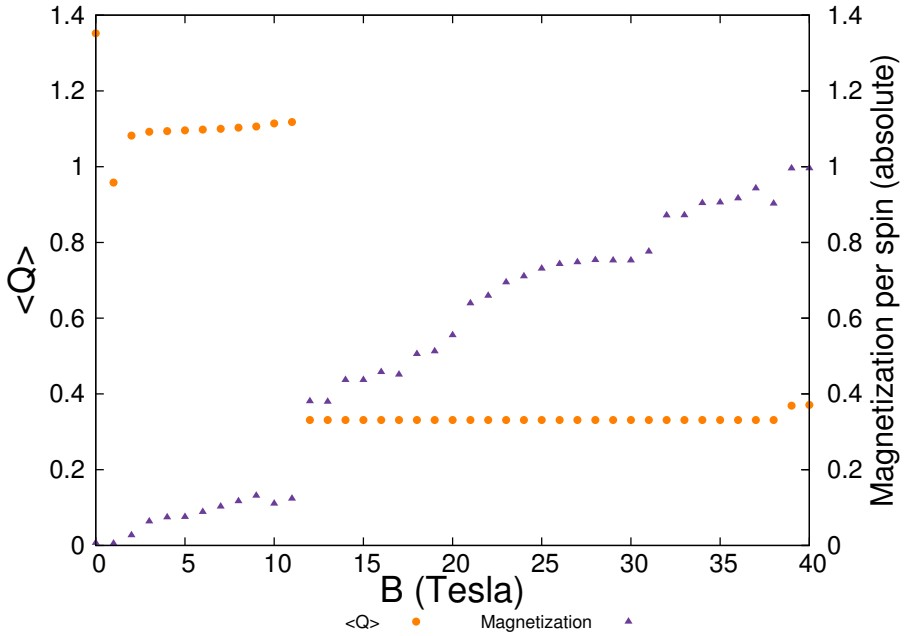

Figure 4.12: $\langle \|\mathbf{Q}\| \rangle$ and magnetization modulus versus B^Z. $A = 0$, $\frac{D}{J} = \frac{2\pi}{5}$, $\frac{D'}{J} = 0.60$, $\frac{g\mu_B}{JS} = 0.318$ T^{-1} and no electric field ($\mathbf{P} \parallel [111]$).

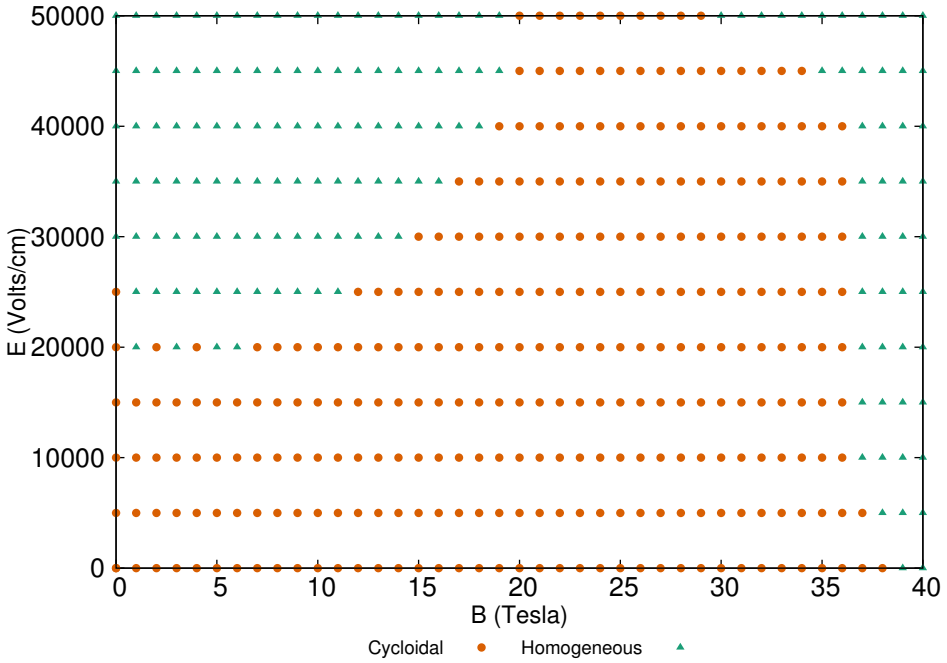

Figure 4.13: $E^X - B^X$ phase diagram. $\mathbf{E} \parallel -\hat{\mathbf{X}}$ and $\mathbf{B} \parallel \hat{\mathbf{X}}$. ($\mathbf{P} \parallel [001]$).

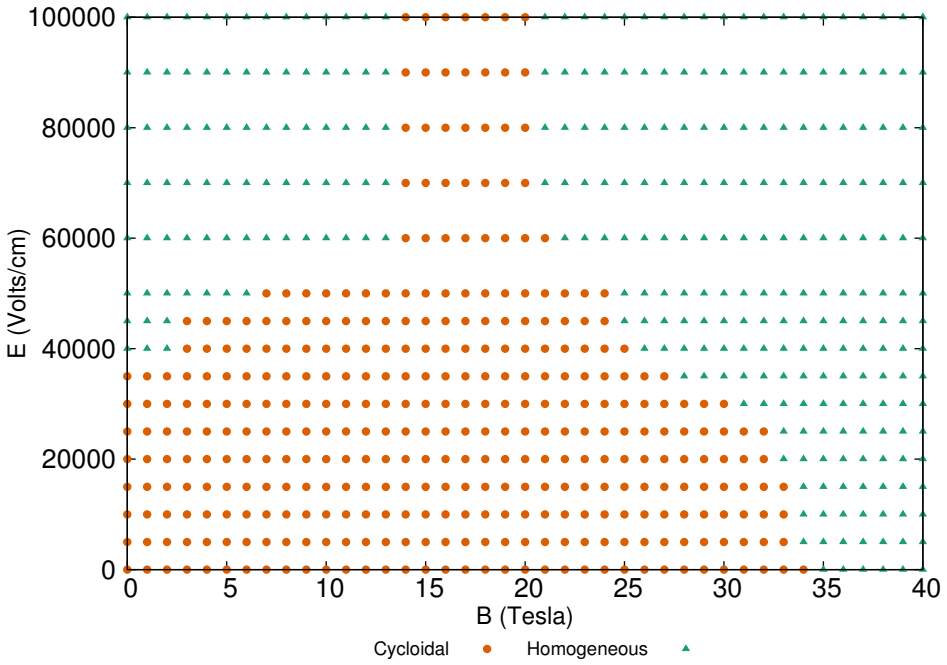

Figure 4.14: $E^X - B^X$ phase diagram. $\mathbf{E} \parallel -\hat{\mathbf{X}}$ and $\mathbf{B} \parallel \hat{\mathbf{X}}$ ($\mathbf{P} \parallel [111]$).

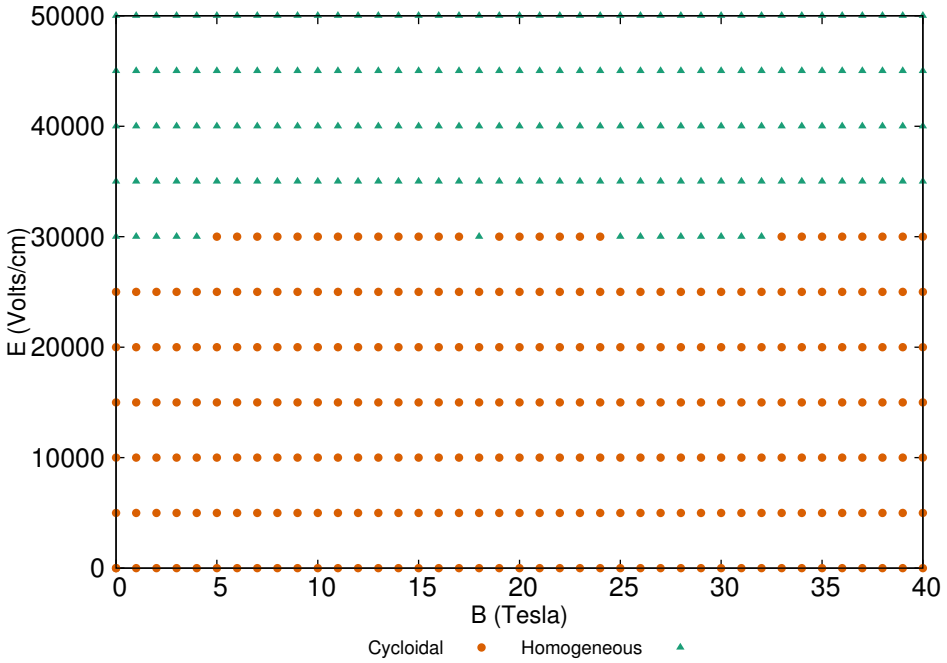

Figure 4.15: $E^X - B^Y$ phase diagram. $\mathbf{E} \parallel -\hat{\mathbf{X}}$ and $\mathbf{B} \parallel \hat{\mathbf{Y}}$ ($\mathbf{P} \parallel [001]$).

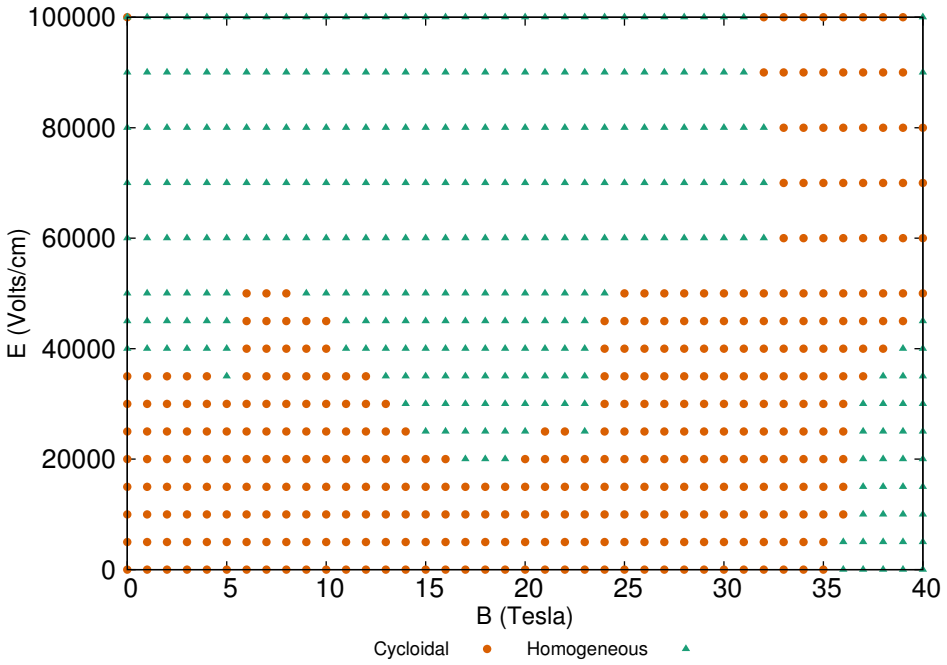

Figure 4.16: $E^X - B^Y$ phase diagram. $\mathbf{E} \parallel -\hat{\mathbf{X}}$ and $\mathbf{B} \parallel \hat{\mathbf{Y}}$ ($\mathbf{P} \parallel [111]$).

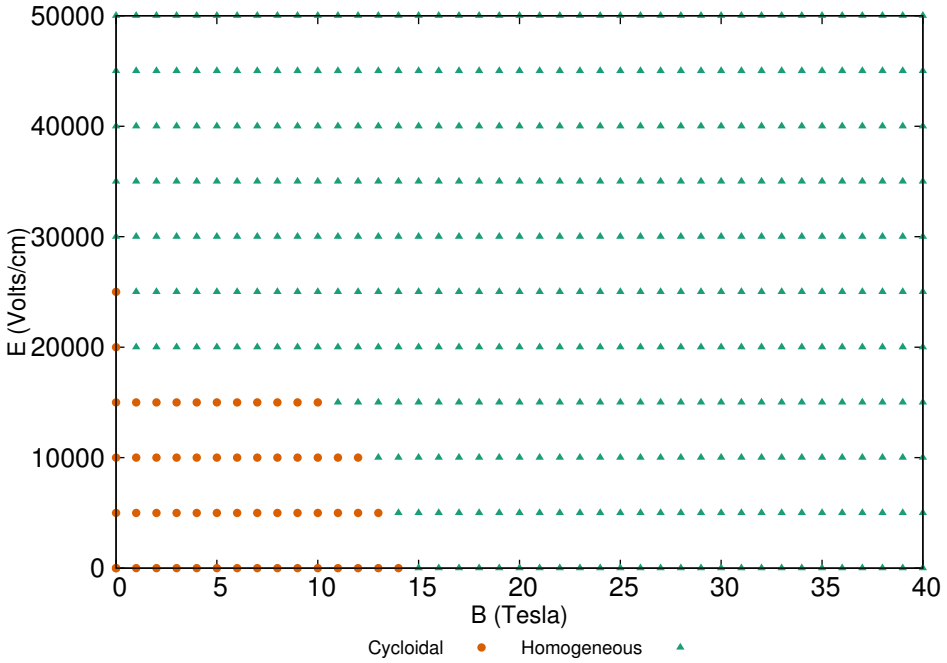

Figure 4.17: $E^X - B^Z$ phase diagram. $\mathbf{E} \parallel -\hat{\mathbf{X}}$ and $\mathbf{B} \parallel \hat{\mathbf{Z}}$ ($\mathbf{P} \parallel [001]$).

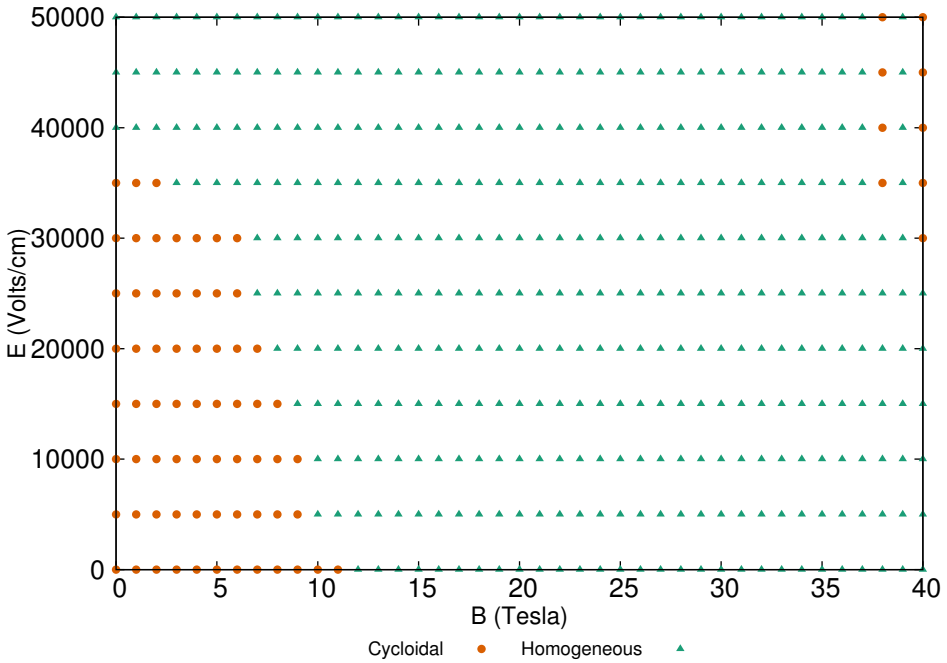

Figure 4.18: $E^X - B^Z$ phase diagram. $\mathbf{E} \parallel -\hat{\mathbf{X}}$ and $\mathbf{B} \parallel \hat{\mathbf{Z}}$ ($\mathbf{P} \parallel [111]$).

Chapter 5

Analysis and Conclusions

The work reported here details how transformations between cycloidal and homogeneous ordering in BFO occurs when electric and magnetic fields are applied. It should be emphasized that large effective magnetic fields can be achieved by growing a ferromagnet on top of BFO, as done in Reference [37]. Thus, our work provides insight in composite structures as well. It was shown that in some instances the fields work cooperatively to destroy the cycloid, such as in Figures 4.17 and 4.18, the $E^X - B^Z$ phase diagrams. In other cases, such as the $E^X - B^X$ phase diagrams (Figures 4.13 and 4.14), the fields interfere and prevent homogeneous ordering from being achieved.

A goal of this work, was to understand how to best switch the BFO spin structure from cycloidal to homogeneous. Obviously, situations where the application of fields, magnetic and electric, complement one another is the best scenario for destroying the cycloid. The $E^X - B^Z$ phase diagrams, Figures 4.17 and 4.18, show a combination of electric and magnetic field where this occurs. Equation (4.23) showed that an electric field in the -$\hat{\mathbf{X}}$ direction favours spins aligned along the $\pm\hat{\mathbf{x}}$ directions. The Zeeman energy in that case,

$$\begin{aligned} H_Z &= -\, g\mu_B \sum_i \sum_{\eta=1,2} \mathbf{S}_{\eta,i} \cdot \mathbf{B} \\ &= -\, g\mu_B B \sum_i \sum_{\eta=1,2} S^Z_{\eta,i} \\ &= -\, \frac{g\mu_B B}{\sqrt{3}} \sum_i \sum_{\eta=1,2} \left(S_{x;\eta,i} + S_{y;\eta,i} + S_{z;\eta,i}\right), \end{aligned} \tag{5.1}$$

showed that a magnetic field along the $\hat{\mathbf{Z}}$ direction favours spins along the positive $\hat{\mathbf{x}}$,

$\hat{\mathbf{y}}$ or $\hat{\mathbf{z}}$ directions. When combined, both the electric field and Zeeman interactions can be partially satisfied. Homogeneous, antiferromagnetic ordering along the $\hat{\mathbf{x}}$ direction will allow the electric field term to lower the energy of the system. Canting in the $\hat{\mathbf{y}} + \hat{\mathbf{z}}$ direction will also allow the Zeeman interaction to further reduce the system's energy.

This happy, cooperative situation does not arise when an electric field in the -$\hat{\mathbf{X}}$ direction is combined with a magnetic field in the $\hat{\mathbf{X}}$ or $\hat{\mathbf{Y}}$ direction. As seen in Equations (4.20) and (A.12), for the given parameters the magnetic field will not induce a transition to homogeneous ordering until near 40 T. For $\mathbf{B} \parallel \hat{\mathbf{X}}$, it is seen in Figures 4.13 and 4.14 that larger magnetic field values pushed the system from homogeneous ordering to cycloidal. A magnetic field in the $\hat{\mathbf{X}}$ direction favours spins aligned along the positive $\hat{\mathbf{y}}$ or $\hat{\mathbf{z}}$ or along the negative $\hat{\mathbf{x}}$ direction:

$$\begin{aligned} H_Z =& - g\mu_B \sum_i \sum_{\eta=1,2} \mathbf{S}_{\eta,i} \cdot \mathbf{B} \\ =& - g\mu_B B \sum_i \sum_{\eta=1,2} S^X_{\eta,i} \\ =& \frac{g\mu_B B}{\sqrt{6}} \sum_i \sum_{\eta=1,2} \left(2S_{x;\eta,i} - S_{y;\eta,i} - S_{z;\eta,i}\right). \end{aligned} \tag{5.2}$$

The electric field compelled spins to align along the $\hat{\mathbf{x}}$ direction in an antiparallel fashion, but $\mathbf{B} \parallel \hat{\mathbf{X}}$ wants spins aligned along the positive $\hat{\mathbf{x}}$ direction, moreso than $\mathbf{B} \parallel \hat{\mathbf{Z}}$ did. This heightened competiton between the electric and magnetic field for domain over the alignment of spins in the $\hat{\mathbf{x}}$ would appear to lead systems that at high $E_\perp$ and low B were homogeneous to become cycloidal. The magnetic field is not strong enough to induce a spin flop, but sufficient that the cycloid is energetically preferable.

With $\mathbf{B} \parallel \hat{\mathbf{Y}}$, the Zeeman energy is

$$\begin{aligned} H_Z =& - g\mu_B \sum_i \sum_{\eta=1,2} \mathbf{S}_{\eta,i} \cdot \mathbf{B} \\ =& - g\mu_B B \sum_i \sum_{\eta=1,2} S^Y_{\eta,i} \\ =& \frac{g\mu_B B}{\sqrt{2}} \sum_i \sum_{\eta=1,2} \left(S_{y;\eta,i} - S_{z;\eta,i}\right). \end{aligned} \tag{5.3}$$

The magnetic field would like the spins along the positive $\hat{\mathbf{z}}$ direction or the negative

$\hat{\mathbf{y}}$ direction. With $\mathbf{E} \parallel -\hat{\mathbf{X}}$, the electric field wants spins along the $\pm\hat{\mathbf{x}}$ directions. It also does not want spins along the positive $\hat{\mathbf{z}}$ direction or the negative $\hat{\mathbf{y}}$ direction. $\mathbf{B} \parallel \hat{\mathbf{Y}}$ does not interact with the x-component of the spins, so it does not mind spins in the $\pm\hat{\mathbf{x}}$ directions. Figure 4.15 suggests that the two fields are nearly independent when $\mathbf{P} \parallel [001]$. The magnetic field, which with no electric field, behaves like $\mathbf{B} \parallel \hat{\mathbf{X}}$, is too weak below 40 T to induce homogeneity. The electric field induces homogeneity at strength somewhat above 2.5×10^4 V cm^{-1}. The magnetic field applied above the critical field does not aid its ability to induce homogeneity, but, also, does not hinder it to a great enough extent that there is a reversion to cycloidal ordering.

It should be noted that the simulations presented here were all performed with no single-ion anisotropy. With single-ion anisotropy included, the situation is different [29]. There would be transitions to homogeneous ordering at lower levels of magnetic field as there is already an interaction working towards that goal in the energy. The choice to run simulations without the presence of anisotropy was made in an attempt to witness the outcome of the most simplistic case when magnetic and electric fields were both present.

The multiferroic nature of BFO is not dependent on the presence of the cycloid. The Fe^{3+} ion is responsible for the antiferromagnetism found in the material and the Bi^{3+} ion is primarily responsible for the ferroelectricity. The ferroelectricity and antiferromagnetism persist even when the system is in the homogeneous configuration. The spin-current interaction, responsible for the cycloid, which, with no field present, induces the cycloid, loses the competition with other interactions when the electric and magnetic fields reach critical values and the crystal undergoes a transformation to homogeneous ordering. This does not destroy the polarization responsible for the spin-current interaction. Merely, other interactions at the critical field values have a greater influence on the composition of the system.

Whilst the transformation from cycloidal to homogeneous ordering is necessary to read out the ferromagnetism found in BFO, the spin-current interaction, responsible for the ability to electrically switch the direction of the cycloid, no longer dominates. Another type of magnetoelectric coupling is found in its place. The electric field-spin coupling allows for the direction of the ferromagnetism to be switched. How the cycloid is unwound affects the crystal's spin structure. As seen in Figure 4.4, $\mathbf{E}_\perp \parallel -\hat{\mathbf{X}}$ will bring about homogeneous ordering with canted spins along $\hat{\mathbf{x}}$. $\mathbf{E}_\perp \parallel -\hat{\mathbf{Y}}$ will cause spins to align along $\hat{\mathbf{y}}$ and $\mathbf{E}_\perp \parallel \hat{\mathbf{Y}}$ will cause spins to align along $\hat{\mathbf{z}}$. The three different spin orientations will induce weak ferromagnetism in three different directions. Thus,

changing the electric field direction will change the direction of the non-zero weak ferromagnetism.

These phase diagrams and the work done to compose them provide insight into the interaction of magnetic and electric fields in terms of controlling the spin structure of BFO. While there has been work done to assess the role of the magnetic field [29, 23, 26, 8, 27] and the electric field [9] play in determining the spin structure of BFO, the two effects have not been studied together before. Analytical results were also derived from the model Hamiltonian and agreed with the numerical ones.

This work was intended to produce electric field-magnetic field phase diagrams which denoted when the spin structure of BFO was cycloidal and when it was homogeneous. These diagrams were presented in Chapter 4 in the form of Figures 4.13, 4.14, 4.15, 4.16, 4.17 and 4.18. They showed that with an electric field in the $-\hat{\mathbf{X}}$ direction and a magnetic field in the $\hat{\mathbf{X}}$ direction, the magnetic field opposed the electric field in transforming cycloidally ordered systmes into homogeneously ordered ones. With the magnetic field in the $\hat{\mathbf{Y}}$ direction, the fields were seemingly independent of each other when $\mathbf{P} \parallel [001]$ and when $\mathbf{P} \parallel [111]$, the magnetic field worked towards or against homogeneous ordering depending on the field value combinations. For a magnetic field in the $\hat{\mathbf{Z}}$ direction, the combination of fields reduced the field strength needed to transform the field from cycloidal to homogeneous.

To produce the phase diagrams, a model Hamiltonian was developed which included an interaction which coupled the spins of the system to an external magnetic field (the Zeeman interaction) and a term which coupled an external electric field to the spins due to spin-orbit coupling. A computer algorithm, based on steepest descent methods, was constructed to numerically calculate the energy of a system of size $20 \times 20 \times 20$ spins. Fast Fourier Transforms were created from the data to determine whether the system was cycloidal or homogeneous for the given applied magnetic and electric fields. These results were compared with analytical ones and general agreement was found between them.

The $20 \times 20 \times 20$ system used here is miniscule relative to that of an actual BFO crystal. The period of the cycloid in BFO is 620 Å and a lattice parameter of nearly 4 Å [12]. That means that a single period of the cycloid runs over many more cells than those of the simulations presented here. To try and replicate the physics happening in such a large system is challenging. Using systems of sizes larger than the one employed here and comparing simulated results is an approach that could be used in the future to verify that the results presented here carry forward with

increasing size.

All of the simulations presented here were done at 0 K with no consideration given to thermal fluctuations. Considering that the interest in BFO is partially driven by it been not only a multiferroic, but a room temperature multiferroic, it would be helpful to conduct simulations at finite temperatures to see how results change when under more practical conditions.

The results presented in this report provide insight into how magnetic fields and electric fields, including the ones coming from heterostructures (such as the ferromagnet CoFe grown on top of BFO [37]), interact in regards to transforming the spin ordering of a BFO system. They highlight what ways are optimal in transforming BFO into a homogeneously-ordered system with order parameter $\mathbf{M}$ that does not average out over short distances. The goal to exploit the weak ferromagnetism of room temperature multiferroic bismuth ferrite in some sort of memory element may well be alive.

Bibliography

[1] J. F. Scott. Data storage: Multiferroic memories. *Nature Materials*, 6(4):256–257, April 2007.

[2] S. Tehrani, J.M. Slaughter, E. Chen, M. Durlam, J. Shi, and M. DeHerren. Progress and outlook for MRAM technology. *IEEE Transactions on Magnetics*, 35(5):2814–2819, September 1999.

[3] W. H. Meiklejohn and C. P. Bean. New magnetic anisotropy. *Physical Review*, 102(5):1413–1414, June 1956.

[4] Ying-Hao Chu, Lane W. Martin, Mikel B. Holcomb, Martin Gajek, Shu-Jen Han, Qing He, Nina Balke, Chan-Ho Yang, Donkoun Lee, Wei Hu, Qian Zhan, Pei-Ling Yang, Arantxa Fraile-Rodriguez, Andreas Scholl, Shan X. Wang, and R. Ramesh. Electric-field control of local ferromagnetism using a magnetoelectric multiferroic. *Nature Materials*, 7(6):478–482, June 2008.

[5] D. Lebeugle, A. Mougin, M. Viret, D. Colson, and L. Ranno. Electric field switching of the magnetic anisotropy of a ferromagnetic layer exchange coupled to the multiferroic compound $BiFeO_3$. *Physical Review Letters*, 103(25):257601, December 2009.

[6] Feiming Bai, Junling Wang, M. Wuttig, JieFang Li, Naigang Wang, A. P. Pyatakov, A. K. Zvezdin, L. E. Cross, and D. Viehland. Destruction of spin cycloid in $(111)_c$-oriented $BiFeO_3$ thin films by epitiaxial constraint: Enhanced polarization and release of latent magnetization. *Applied Physics Letters*, 86:032511, 2005.

[7] P. Chen, Ö. Günaydın-Şen, W. J. Ren, Z. Qin, T. V. Brinzari, S. McGill, S.-W. Cheong, and J. L. Musfeldt. Spin cycloid quenching in Nd^{3+}-substituted $BiFeO_3$. *Physical Review B*, 86(1):014407, July 2012.

[8] Yu. F. Popov, A. K. Zvezdin, G. P. Vorob'ev, A. M. Kadomtseva, V. A. Murashev, and D. N. Rakov. Linear magnetoelectric effect and phase transitions in bismuth ferrite $BiFeO_3$. *Soviet Journal of Experimental and Theoretical Physics Letters*, 57:69, January 1993.

[9] Rogério de Sousa, Marc Allen, and Maximilien Cazayous. Theory of spin-orbit enhanced electric-field control of magnetism in multiferroic $BiFeO_3$. *Physical Review Letters*, 110(26):267202, June 2013.

[10] Nicola A. Spaldin, Sang-Wook Cheong, and Ramamoorthy Ramesh. Multiferroics: Past, present, and future. *Physics Today*, 63(10):38–43, 2010.

[11] M. Ramazanoglu, W. Ratcliff, Y. J. Choi, Seongsu Lee, S.-W. Cheong, and V. Kiryukhin. Temperature-dependent properties of the magnetic order in single-crystal $BiFeO_3$. *Physical Review B*, 83(17):174434, May 2011.

[12] Gustau Catalan and James F. Scott. Physics and applications of bismuth ferrite. *Advanced Materials*, 21(24):2463–2485, June 2009.

[13] Sang-Wook Cheong and Maxim Mostovoy. Multiferroics: a magnetic twist for ferroelectricity. *Nature Materials*, 6(1):13–20, January 2007.

[14] Nicola A. Hill. Why are there so few magnetic ferroelectrics? *J. Phys. Chem. B*, 104(29):6694–6709, 2000.

[15] R. Ramesh and Nicola A. Spaldin. Multiferroics: progress and prospects in thin films. *Nature Materials*, 6(1):21–29, January 2007.

[16] J. B. Neaton, C. Ederer, U. V. Waghmare, N. A. Spaldin, and K. M. Rabe. First-principles study of spontaneous polarization in multiferroic $BiFeO_3$. *Physical Review B*, 71(1):014113, January 2005.

[17] P. Rovillain, R. de Sousa, Y. Gallais, A. Sacuto, M. A. Méasson, D. Colson, A. Forget, M. Bibes, A. Barthélémy, and M. Cazayous. Electric-field control of spin waves at room temperature in multiferroic $BiFeO_3$. *Nature Materials*, 9(12):975–979, December 2010.

[18] Michael Tinkham. *Group theory and quantum mechanics*. International series in pure and applied physics. McGraw-Hill, New York, 1964.

[19] Hosho Katsura, Naoto Nagaosa, and Alexander V. Balatsky. Spin current and magnetoelectric effect in noncollinear magnets. *Physical Review Letters*, 95(5):057205, July 2005.

[20] D. Rahmedov, Dawei Wang, Jorge Íñiguez, and L. Bellaiche. Magnetic cycloid of $BiFeO_3$ from atomistic simulations. *Physical Review Letters*, 109(3):037207, July 2012.

[21] Rogério de Sousa and Joel E. Moore. Comment on "Ferroelectrically induced weak ferromagnetism by design". *Physical Review Letters*, 102(24):249701, June 2009.

[22] Claude Ederer and Nicola A. Spaldin. Weak ferromagnetism and magnetoelectric coupling in bismuth ferrite. *Physical Review B*, 71(6):060401, February 2005.

[23] A. M. Kadomtseva, A. K. Zvezdin, Yu. F. Popov, A. P. Pyatakov, and G. P. Vorob'ev. Space-time parity violation and magnetoelectric interactions in antiferromagnets. *Journal of Experimental and Theoretical Physics Letters*, 79:571–581, June 2004.

[24] M. Ramazanoglu, M. Laver, W. Ratcliff, S. M. Watson, W. C. Chen, A. Jackson, K. Kothapalli, Seongsu Lee, S.-W. Cheong, and V. Kiryukhin. Local weak ferromagnetism in single-crystalline ferroelectric $BiFeO_3$. *Physical Review Letters*, 107(20):207206, November 2011.

[25] D. Lebeugle, D. Colson, A. Forget, M. Viret, A. M. Bataille, and A. Gukasov. Electric-field-induced spin flop in $BiFeO_3$ single crystals at room temperature. *Physical Review Letters*, 100(22):227602, June 2008.

[26] Junghwan Park, Sang-Hyun Lee, Seongsu Lee, Fabia Gozzo, Hiroyuki Kimura, Yukio Noda, Young Jai Choi, Valery Kiryukhin, Sang-Wook Cheong, Younjung Jo, Eun Sang Choi, Luis Balicas, Gun Sang Jeon, and Je-Geun Park. Magnetoelectric feedback among magnetic order, polarization, and lattice in multiferroic $BiFeO_3$. *Journal of the Physical Society of Japan*, 80:114714, 2011.

[27] Masashi Tokunaga, Masaki Azuma, and Yuichi Shimakawa. High-field study of strong magnetoelectric coupling in single-domain crystals of $BiFeO_3$. *Journal of the Physical Society of Japan*, 79:064713, 2010.

[28] G. L. Yuan, Siu Wing Or, J. M. Liu, and Z. G. Liu. Structural transformation and ferroelectromagnetic behavior in single-phase $Bi_{1-x}Nd_xFeO_3$ multiferroic ceramics. *Applied Physics Letters*, 89(5):052905, July 2006.

[29] Randy S. Fishman. Orientation dependence of the critical magnetic field for multiferroic $BiFeO_3$. *Physical Review B*, 88(10):104419, September 2013.

[30] E. O. Wollan and W. C. Koehler. Neutron diffraction study of the magnetic properties of the series of perovskite-type compounds [(1-x)La, xCa]MnO_3. *Physical Review*, 100(2):545–563, October 1955.

[31] Nicola Spaldin. *Magnetic materials : fundamentals and applications*. Cambridge University Press, Cambridge; New York, 2nd ed. edition, 2011.

[32] I.E. Dzyaloshinskii. A thermodynamic theory of "weak" ferromagnetism of antiferromagnetics. *Journal of Physics and Chemistry of Solids*, 4(4):241–255, 1958.

[33] Tôru Moriya. New mechanism of anisotropic superexchange interaction. *Physical Review Letters*, 4(5):228–230, March 1960.

[34] Tôru Moriya. Anisotropic superexchange interaction and weak ferromagnetism. *Physical Review*, 120(1):91, October 1960.

[35] P. W. Atkins and Ronald Friedman. *Molecular quantum mechanics*. Oxford University Press, Oxford; New York, 5th edition, 2011.

[36] Jorge Nocedal and Stephen J. Wright. *Numerical optimization*. Springer Series in Operations Research and Financial Engineering. Springer New York, second edition, January 2006.

[37] J. T. Heron, M. Trassin, K. Ashraf, M. Gajek, Q. He, S. Y. Yang, D. E. Nikonov, Y-H. Chu, S. Salahuddin, and R. Ramesh. Electric-field-induced magnetization reversal in a ferromagnet-multiferroic heterostructure. *Physical Review Letters*, 107(21):217202, November 2011.

Appendix A

Energy for Polarization along [111]

Presented here are the calculations for the energy with different spin configurations when the polarization is along [111]. In some instances they differ from the energy when $\mathbf{P} \parallel [001]$ due to $\hat{\mathbf{Q}}$ and $\boldsymbol{\delta} + \boldsymbol{\tau}$ no longer being either perpendicular or parallel to each other as is the case when $\mathbf{P} \parallel [001]$.

Returning to the conical cycloid with the conditions as in Section 4.1:

$$\mathbf{B} = B\ \hat{\mathbf{X}}, A = E = 0.$$

Again, the two sublattices are:

$$\mathbf{S}_{1,i} = S\left(\sin\theta\,\hat{\mathbf{X}} + \cos\theta\left[\sin\left\{\mathbf{Q}\cdot\mathbf{R}_{1,i}\right\}\hat{\mathbf{Y}} + \cos\left\{\mathbf{Q}\cdot\mathbf{R}_{1,i}\right\}\hat{\mathbf{Z}}\right]\right), \tag{A.1}$$

$$\mathbf{S}_{2,i} = S\left(\sin\theta\,\hat{\mathbf{X}} - \cos\theta\left[\sin\left\{\mathbf{Q}\cdot\mathbf{R}_{2,i}\right\}\hat{\mathbf{Y}} + \cos\left\{\mathbf{Q}\cdot\mathbf{R}_{2,i}\right\}\hat{\mathbf{Z}}\right]\right). \tag{A.2}$$

The angle θ is the angle between the spin vectors and the YZ-plane. This solution is put into the Hamiltonian and simplified. Taking $\mathbf{Q} = Q\,\hat{\mathbf{Y}}$ to minimize the energy,

$$\begin{aligned} H_{cc} &= \frac{NS^2}{2}\left(J\left[6\sin^2\theta - \cos^2\theta\sum_{\boldsymbol{\delta}}\cos\left\{\mathbf{Q}\cdot(\boldsymbol{\tau}+\boldsymbol{\delta})\right\}\right]\right. \\ &\quad \left. - \frac{D\cos^2\theta}{a_{Rh}}\hat{\mathbf{Y}}\cdot\sum_{\boldsymbol{\delta}}\left[\boldsymbol{\tau}+\boldsymbol{\delta}\right]\sin\left[\mathbf{Q}\cdot\left\{\boldsymbol{\tau}+\boldsymbol{\delta}\right\}\right]\right) - NSg\mu_B B\sin\theta \\ &= \frac{NS^2}{2}\left(J\left[6\sin^2\theta - \cos^2\theta\left\{2 + 4\cos\left(\frac{Qa_{Rh}}{\sqrt{2}}\right)\right\}\right] - \frac{4}{\sqrt{2}}D\cos^2\theta\sin\left[\frac{Qa_{Rh}}{\sqrt{2}}\right]\right) \\ &\quad - NSg\mu_B B\sin\theta \end{aligned}$$

$$= NS^2 \left(3J \sin^2\theta - \cos^2\theta \left[J + 2J \cos\left\{ \frac{Qa_{Rh}}{\sqrt{2}} \right\} + \sqrt{2}D \sin\left\{ \frac{Qa_{Rh}}{\sqrt{2}} \right\} \right] - \frac{g\mu_B B \sin\theta}{S} \right). \tag{A.3}$$

Q can be optimized:

$$\frac{\partial H_{cc}}{\partial Q} = -\frac{NS^2 \cos^2\theta a_{Rh}}{\sqrt{2}} \left(\sqrt{2}D \cos\left[\frac{Qa_{Rh}}{\sqrt{2}} \right] - 2J \sin\left[\frac{Qa_{Rh}}{\sqrt{2}} \right] \right) = 0$$
$$\implies \tan\left(\frac{Qa_{Rh}}{\sqrt{2}} \right) = \frac{D}{\sqrt{2}J}. \tag{A.4}$$

Equation (A.4) can be used to define $\sin\left(\frac{Qa_{Rh}}{\sqrt{2}}\right)$ and $\cos\left(\frac{Qa_{Rh}}{\sqrt{2}}\right)$:

$$\sin\left(\frac{Qa_{Rh}}{\sqrt{2}} \right) = \frac{D}{\sqrt{D^2 + 2J^2}}, \tag{A.5}$$
$$\cos\left(\frac{Qa_{Rh}}{\sqrt{2}} \right) = \frac{2J}{\sqrt{2D^2 + 4J^2}}. \tag{A.6}$$

These can then be replaced in the Hamiltonian,

$$H_{cc} = NS^2 \left(3J \sin^2\theta - \cos^2\theta \left[J + \frac{4J^2}{\sqrt{2D^2 + 4J^2}} + \frac{2D^2}{\sqrt{2D^2 + 4J^2}} \right] - \frac{g\mu_B B \sin\theta}{S} \right)$$
$$= NS^2 \left(3J \sin^2\theta - \cos^2\theta \left[J + \sqrt{2D^2 + 4J^2} \right] - \frac{g\mu_B B \sin\theta}{S} \right)$$
$$= NS^2 \left(-J - \sqrt{2D^2 + 4J^2} + \sin^2\theta \left[4J + \sqrt{2D^2 + 4J^2} \right] - \frac{g\mu_B B \sin\theta}{S} \right) \tag{A.7}$$

The derivative of H_{cc} with respect to θ can then be taken to minimize the energy:

$$\frac{\partial H_{cc}}{\partial \theta} = NS^2 \cos\theta \left(2 \sin\theta \left[4J + \sqrt{D^2 + J^2} \right] - \frac{g\mu_B B}{S} \right) = 0$$
$$\implies \sin\theta = \frac{g\mu_B B}{2S\left(4J + \sqrt{2D^2 + 4J^2} \right)}. \tag{A.8}$$

This is then substituted into the energy term:

$$H_{cc} = NS^2 \left(-J - \sqrt{2D^2 + 4J^2} + \left[\frac{g\mu_B B}{2S\left\{ 4J + \sqrt{2D^2 + 4J^2} \right\}} \right]^2 \left[4J + \sqrt{2D^2 + 4J^2} \right] \right.$$

$$- \frac{[g\mu_B B]^2}{2S^2\left[4J+\sqrt{2D^2+4J^2}\right]}\Bigg)$$
$$= -NS^2\left(J+\sqrt{2D^2+4J^2}+\frac{[g\mu_B B]^2}{4S^2\left[4J+\sqrt{2D^2+4J^2}\right]}\right). \tag{A.9}$$

The energy per spin is

$$\frac{H_{cc}}{JNS^2} = -\left(1+2\sqrt{1+\frac{1}{2}\left[\frac{D}{J}\right]^2}+\left[\frac{g\mu_B B}{2JS}\right]^2\frac{1}{4+2\sqrt{1+\frac{1}{2}\left[\frac{D}{J}\right]^2}}\right). \tag{A.10}$$

If there is no magnetic field then the energy per spin is

$$\frac{H_{cc}}{JNS^2} = -\left(1+2\sqrt{1+\frac{1}{2}\left[\frac{D}{J}\right]^2}\right). \tag{A.11}$$

This is the lower line plotted in Figure 4.1. It is lower in energy than when the polarization is along [001] because four spin-current interaction terms contribute to it versus the two in the $\mathbf{P} \parallel [001]$ case.

The energy is the same irrespective of polarization direction when the spin are in a homogeneous configuration as the Dzyaloshinskii-Moriya interaction is zero when spins are antiparallel. A comparison can be made between the conical cycloid and the homogeneous energies to see when the transition to homogeneous ordering occurs.

$$E_{cc} > E_{homogeneous}$$
$$-NS^2\left(J+\sqrt{2D^2+4J^2}+\frac{[g\mu_B B]^2}{4S^2\left[4J+\sqrt{2D^2+4J^2}\right]}\right) > -NJS^2\left(3+\frac{1}{24}\left[\frac{g\mu_B B}{JS}\right]^2\right)$$
$$\left(\frac{g\mu_B B}{2S}\right)^2\left(\frac{1}{4J+\sqrt{2D^2+4J^2}}-\frac{1}{6J}\right) < 2J-\sqrt{2D^2+4J^2}$$
$$\left(\frac{g\mu_B B}{2S}\right)^2\frac{6J-4J-\sqrt{2D^2+4J^2}}{6J\left(4J+\sqrt{2D^2+4J^2}\right)} < 2J-\sqrt{2D^2+4J^2}$$
$$B^2 > 6J\left(4J+\sqrt{2D^2+4J^2}\right)\left(\frac{2S}{g\mu_B}\right)^2$$
$$B^2 > 48\left(2+\sqrt{1+\frac{1}{2}\left[\frac{D}{J}\right]^2}\right)\left(\frac{JS}{g\mu_B}\right)^2$$

$$\left(B^2\right)_c = 48\left(2+\sqrt{1+\frac{1}{2}\left[\frac{D}{J}\right]^2}\right)\left(\frac{JS}{g\mu_B}\right)^2. \tag{A.12}$$

With $\frac{D}{J}=\frac{2\pi}{5}$ and $\frac{g\mu_B}{JS}=0.318\,\mathrm{T}^{-1}$, as used in the simulations, the critical magnetic field is

$$\begin{aligned}\left(B^2\right)_c &= 48\left(2+\sqrt{1+\frac{1}{2}\left[\frac{D}{J}\right]^2}\right)\left(\frac{JS}{g\mu_B}\right)^2\\ &= 48\left(2+\sqrt{1+\frac{1}{2}\left[\frac{2\pi}{5}\right]^2}\right)\left(0.318\,\mathrm{T}^{-1}\right)^{-2}\\ &= 1.58\times10^3\,\mathrm{T}^2.\\ B_c &= 39.8\,\mathrm{T}.\end{aligned}$$

The critical magnetic field is 39.8 T which is slightly higher than what it is in the [001] configuration.

The cycloidal case for an applied electric field can also be investigated:

$$\mathbf{S}_{1,i} = S\left(\sin\left[\mathbf{Q}\cdot\mathbf{R}_{1,i}\right]\hat{\mathbf{Y}}+\cos\left[\mathbf{Q}\cdot\mathbf{R}_{1,i}\right]\hat{\mathbf{Z}}\right), \tag{A.13}$$

$$\mathbf{S}_{2,i} = -S\left(\sin\left[\mathbf{Q}\cdot\mathbf{R}_{2,i}\right]\hat{\mathbf{Y}}+\cos\left[\mathbf{Q}\cdot\mathbf{R}_{2,i}\right]\hat{\mathbf{Z}}\right). \tag{A.14}$$

Once more, this is put into the Hamiltonian,

$$\begin{aligned}H_{cycloid} &= \frac{NS^2}{2}\left(-J\sum_{\boldsymbol{\delta}}\cos\left[\mathbf{Q}\cdot\{\boldsymbol{\tau}+\boldsymbol{\delta}\}\right]\right.\\ &\quad\left.+\frac{D}{a_{Rh}}\left[\hat{\mathbf{X}}\times\hat{\mathbf{Z}}\right]\cdot\sum_{\boldsymbol{\delta}}\left[\boldsymbol{\tau}+\boldsymbol{\delta}\right]\sin\left[\mathbf{Q}\cdot\{\boldsymbol{\tau}+\boldsymbol{\delta}\}\right]+\frac{\xi E_\perp}{4}\right)\\ &= \frac{NS^2}{2}\left(-J\sum_{\boldsymbol{\delta}}\cos\left[\mathbf{Q}\cdot\{\boldsymbol{\tau}+\boldsymbol{\delta}\}\right]+\frac{D}{a_{Rh}}\hat{\mathbf{Y}}\cdot\sum_{\boldsymbol{\delta}}\left[\boldsymbol{\tau}+\boldsymbol{\delta}\right]\sin\left[\mathbf{Q}\cdot\{\boldsymbol{\tau}+\boldsymbol{\delta}\}\right]\right.\\ &\quad\left.+\frac{\xi E_\perp}{4}\right)\\ &= -NS^2\left(J\left[1+2\cos\left\{\frac{Qa_{Rh}}{\sqrt{2}}\right\}\right]+\sqrt{2}D\sin\left[\frac{Qa_{Rh}}{\sqrt{2}}\right]-\frac{\xi E_\perp}{8}\right).\end{aligned} \tag{A.15}$$

$\mathbf{Q}=Q\,\hat{\mathbf{Y}}$ gives the lowest energy. The derivative with respect to Q can be taken of

the Hamiltonian to find the value of Q which minimizes the energy.

$$\frac{\partial H_{cycloid}}{\partial Q} = -\frac{NS^2 a_{Rh}}{\sqrt{2}}\left(\sqrt{2}D\cos\left[\frac{Qa_{Rh}}{\sqrt{2}}\right] - 2J\sin\left[\frac{Qa_{Rh}}{\sqrt{2}}\right]\right) = 0$$
$$\implies \tan\left(\frac{Qa_{Rh}}{\sqrt{2}}\right) = \frac{D}{\sqrt{2}J}. \tag{A.16}$$

From this,

$$\sin\left(\frac{Qa_{Rh}}{\sqrt{2}}\right) = \frac{D}{\sqrt{D^2+2J^2}}, \tag{A.17}$$
$$\cos\left(\frac{Qa_{Rh}}{\sqrt{2}}\right) = \frac{2J}{\sqrt{2D^2+4J^2}}. \tag{A.18}$$

Placing these terms in the Hamiltonian,

$$E_{cycloid} = -NS^2\left(J\left[1+\frac{4J}{\sqrt{2D^2+4J^2}}\right] + \frac{2D^2}{\sqrt{2D^2+4J^2}} - \frac{\xi E_\perp}{8}\right)$$
$$= -NS^2\left(J + \sqrt{2D^2+4J^2} - \frac{\xi E_\perp}{8}\right). \tag{A.19}$$

The homogeneous energy is unchanged from Equation (4.28) as the Dzyaloshinskii-Moriya interaction does not contribute as the spins are antiparallel. Now, the energies of the cycloidal and homogeneous states can be analyzed to see at what value of electric field it is preferable for the spins to align homogeneously:

$$E_{cycloid} > E_{homogeneous}$$
$$-NS^2\left(J + \sqrt{2D^2+4J^2} - \frac{\xi E_\perp}{8}\right) > -NS^2\left(3J + \frac{\xi E_\perp}{2}\right)$$
$$\sqrt{2D^2+4J^2} < 2J + \frac{5\xi E_\perp}{8}$$
$$E_\perp > \frac{8\left(\sqrt{2D^2+4J^2} - 2J\right)}{5\xi}$$
$$E_\perp > \frac{16\left(\sqrt{1+\frac{1}{2}\left[\frac{D}{J}\right]^2} - 1\right)}{\frac{5\xi}{J}}$$
$$(E_\perp)_c = \frac{16\left(\sqrt{1+\frac{1}{2}\left[\frac{D}{J}\right]^2} - 1\right)}{\frac{5\xi}{J}}. \tag{A.20}$$

With $\dfrac{D}{J} = \dfrac{2\pi}{5}$ and $\dfrac{\xi}{J} = 5.77 \times 10^{-5}\,\mathrm{cm\,V^{-1}}$,

$$\begin{aligned}(E_\perp)_c &= \frac{16\left(\sqrt{1+\frac{1}{2}\left[\frac{2\pi}{5}\right]^2}-1\right)}{5\left(5.77\times10^{-5}\,\mathrm{cm\,V^{-1}}\right)} \\ &= 1.87\times10^{4}\,\mathrm{V\,cm^{-1}}.\end{aligned}$$

The critical electric field is $1.87 \times 10^4\,\mathrm{V\,cm^{-1}}$.

Appendix B

Additional Results

Additional results which were omitted from the main body of the thesis have been included in this appendix. These results are with the polarization along the [001] direction.

Figure B.1 shows a collection of projections of the spins from two simulations. One simulation was with $B^Z = 10$ T and the other with $B^Z = 20$ T. There were no other applied fields for these simulations. Other parameters for the simulations were: $A = 0$; $\frac{D}{J} = \frac{2\pi}{5}$; and $\frac{D'}{J} = 0.60$. With the transition from cycloidal to homogeneous ordering at 15 T, these simulations show the system in both configurations. In the projections, all spins start at the origin.

At $B^Z = 10$ T, for all three projections (in the XY-, XZ- and YZ-planes) the spins are distributed around the plane. It should be noted that the images are the projections of 8000 spins onto a plane. A random collection of spins would have be evenly spread out around the plane. These spins notably only take a few positions, indicative of a repeating structure which, in this case, is the cycloid.

At $B^Z = 20$ T, the cycloid is clearly eliminated. All spins belonging to the same sublattice are found in the same position. The spins also have a net moment in the positive $\hat{\mathbf{Z}}$ direction as one would anticipate with a magentic field applied in the $\hat{\mathbf{Z}}$ direction.

Figure B.2 shows the FFT of one sublattice along the $\widehat{\mathbf{k^Y}}$ direction as well as $\left\|\tilde{\mathbf{M}}_{\mathbf{k}}\right\|$ and $\left\|\tilde{\mathbf{L}}_{\mathbf{k}}\right\|$ versus k^Y. Again, this is for $B^Z = 10$ T and $B^Z = 20$ T. The other simulation parameters were $A = E = 0$; $\frac{D}{J} = \frac{2\pi}{5}$; and $\frac{D'}{J} = 0.60$.

When the system was at $B^Z = 10$ T, there were two symmetric off-centre peaks in the FFT. This, as shown in Chapter 3, is indicative of a cycloid. At $B^Z = 20$ T,

there is a large central peak, suggestive that the system transitioned to homogeneous ordering. On the $\left\|\tilde{\mathbf{M}}_{\mathbf{k}}\right\|$ versus k^Y and $\left\|\tilde{\mathbf{L}}_{\mathbf{k}}\right\|$ versus k^Y plots, there are similar trends with off-centre peaks at $B^Z = 10$ T and a large central peak at $B^Z = 20$ T. Peaks of $\left\|\tilde{\mathbf{L}}_{\mathbf{k}}\right\|$ are higher than that of $\left\|\tilde{\mathbf{M}}_{\mathbf{k}}\right\|$ at both $B^Z = 10$ T and $B^Z = 20$ T, indicating that at both values of magnetic field, the system has more antiferromagnetic character than ferromagnetic.

Figure B.3 shows the projection of the spins in the XY-, XZ- and YZ-planes when no fields are applied. The conventional parameters were used in the simulation. There is significant overlap of the spins of the two sublattices as in the projections the spins of sublattice one cannot be seen as they are all covered by the spins of sublattice two. The X-component of the spins is nearly negligible, which, along with the projections in the other planes which have spins spread throughout, suggests that this is a cycloid with $\mathbf{Q} = \hat{\mathbf{Y}}$.

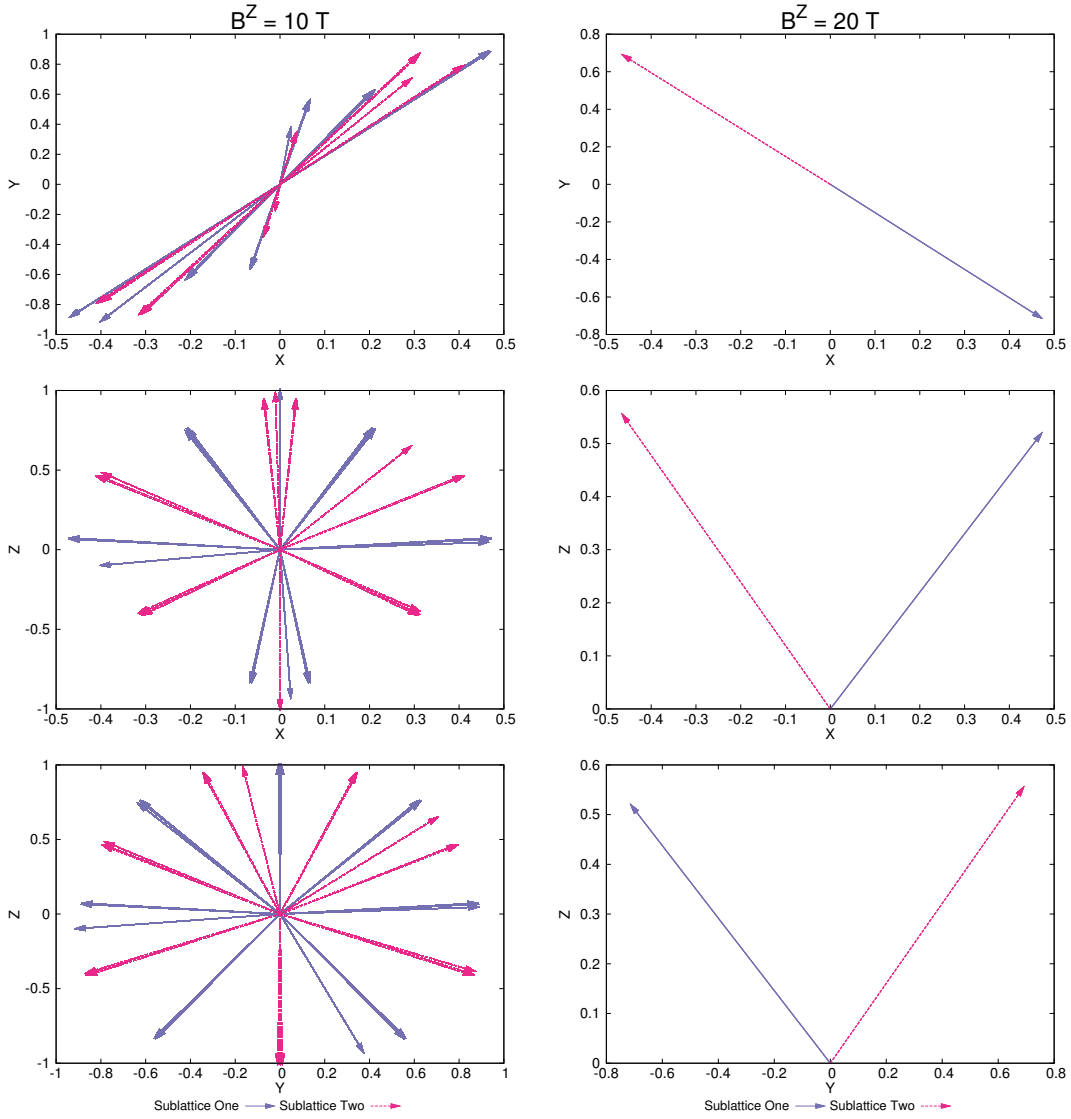

Figure B.1: A comparison of spin projections with $B^Z = 10$ T and $B^Z = 20$ T. Projections are in the XY-, XZ- and YZ-planes. $A = B^X = B^Y = E = 0; \frac{D}{J} = \frac{2\pi}{5}; \frac{D'}{J} = 0.60$.

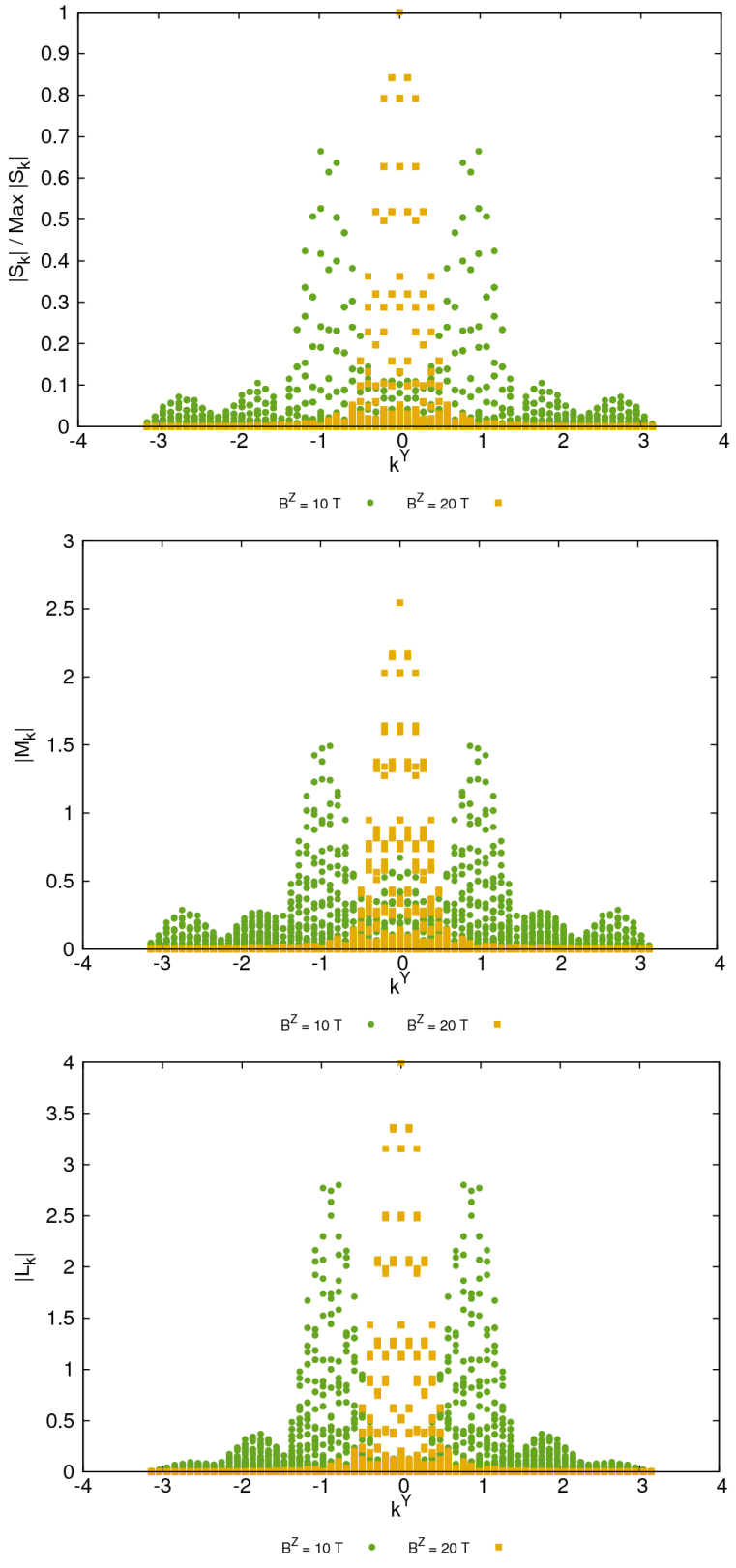

Figure B.2: FFT, $\left\|\tilde{\mathbf{M}}_{\mathbf{k}}\right\|$ and $\left\|\tilde{\mathbf{L}}_{\mathbf{k}}\right\|$ versus k^Y for $B^Z = 10$ T and $B^Z = 20$ T. $A = B^X = B^Y = E = 0; \frac{D}{J} = \frac{2\pi}{5}; \frac{D'}{J} = 0.60$.

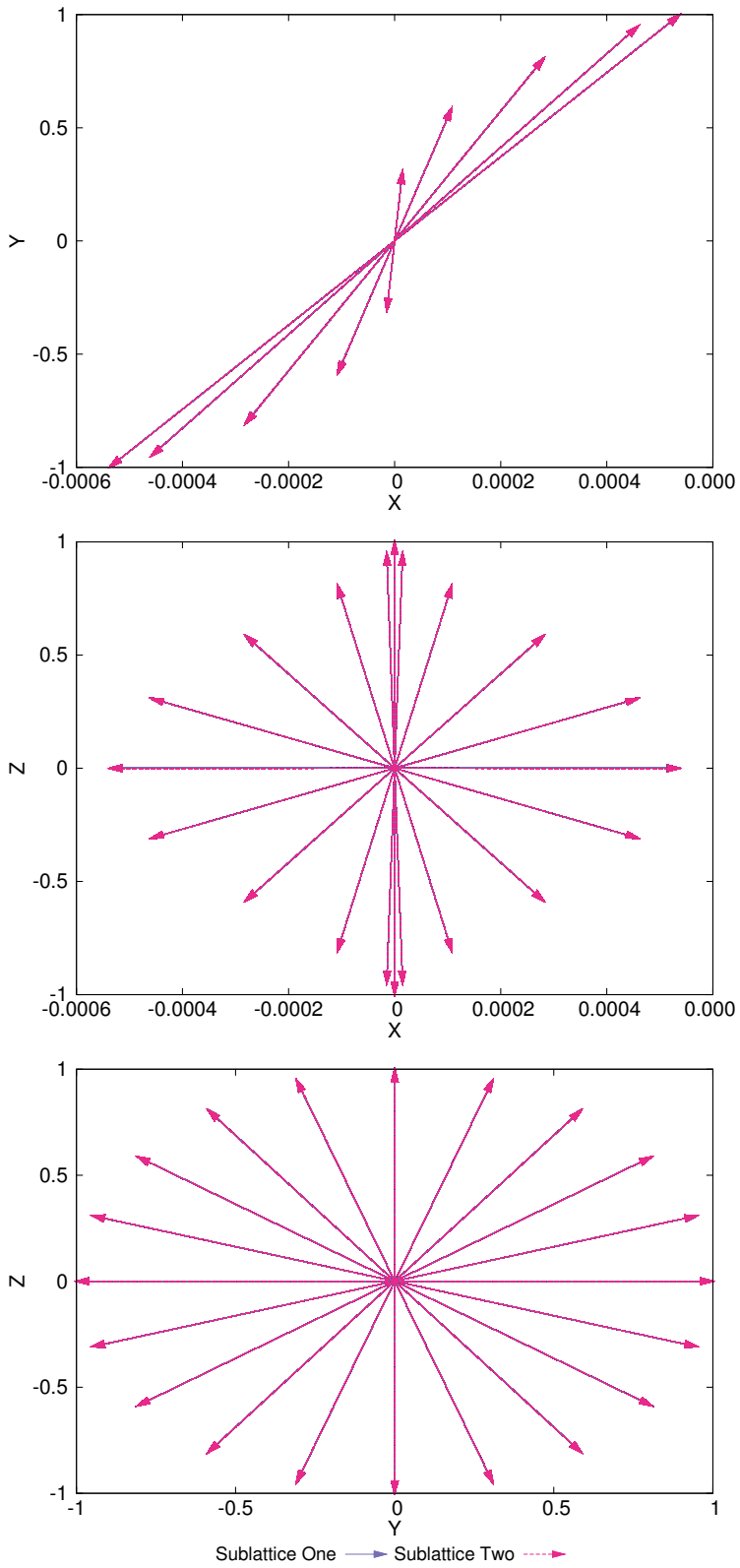

Figure B.3: Spin projections with no applied fields. Projections are in the XY-, XZ- and YZ-planes. $A = 0; \frac{D}{J} = \frac{2\pi}{5}; \frac{D'}{J} = 0.60.$